USING TIGHTLY-COUPLED CFD/CSD SIMULATION FOR ROTORCRAFT STABILITY ANALYSIS

A Thesis
Presented to
The Academic Faculty

by

Afifa Adel Zaki

In Partial Fulfillment
of the Requirements for the Degree
Doctor of Philosophy in the
School of Aerospace Engineering

Georgia Institute of Technology
May 2012

USING TIGHTLY-COUPLED CFD/CSD SIMULATION FOR ROTORCRAFT STABILITY ANALYSIS

Approved by:

Professor Olivier Bauchau, Co-advisor
Mechanical Engineering
University of Michigan-Shanghai Jiao Tong University Joint Institute
(Formerly Georgia Tech Professor at School of Aerospace Engineering)

Professor Dewey Hodges
School of Aerospace Engineering
Georgia Institute of Technology

Professor Marilyn Smith, Co-advisor
School of Aerospace Engineering
Georgia Institute of Technology

Professor Erian Armanios
College of Engineering
The University of Texas at Arlington

Professor Massimo Ruzzene
School of Aerospace Engineering
Georgia Institute of Technology

Date Approved: January 13, 2012

In the name of the Father, and the Son, and the

Holy Spirit, one God. Amen.

Dedicated to my husband and family

For their continuous encouragement and endless love and support.

ACKNOWLEDGEMENTS

I would like first to thank my God and my Savior Jesus Christ for His gift of salvation, tender mercy, grace, and many blessings. I would also like to thank the Theotokos St. Mary and all the holy saints for interceding and praying for us. I would like to thank Dr. Olivier A. Bauchau, my thesis advisor, for his guidance and advice throughout my research work, and Dr. Marilyn Smith my co-advisor for her guidance and advice and especially for dedicating the time towards my thesis revision. I would like to thank my thesis committee members: Dr. Dewey Hodges, Dr. Erian Armanios, and Dr. Massimo Ruzzene for their valuable comments and suggestions. I would also like to thank Dr. Jeff Jagoda, the Associate Chair for Graduate Studies and Research, for his help, time and support. I would like to deeply thank all my friends at Georgia Tech. especially Reema Kundu and Ritu Marpu for their endless support, prayers, and help. I would like to express my thanks to Yannick Vanweddingen for his help, time and guidance. I would also like to thank Nicolas Reveles who has been working with me on the CFD/CSD project *Innovative Strategies for Rotary-Wing Coupled Aeroelastic Simulations*, under the supervision of Dr. Olivier Bauchau and Dr. Marilyn Smith. He performed the research on the CFD portion of this project and provided all of the CFD/CSD coupled results shown in this thesis. I would like to thank Nashwa Farag for her time and help. Finally, I owe my greatest gratitude to my family for their encouragement, patience, and great love. Thank you.

Contents

List of Tables

List of Figures

LIST OF SYMBOLS

a = Speed of sound, m/sec

A_i = Coefficients of circulatory indicial response functions

b_i = Exponent (pole) of indicial response functions

b = The semi-chord length

c = Airfoil chord, m

c_c = Chord force coefficient

c_d = Pressure drag coefficient

c_m = quarter-chord pitching moment coefficient

c_{m_0} = Zero-lift pitching moment of the airfoil

c_m^v = Vortex induced pitching moment coefficient

c_n = Normal force coefficient

c_{n_1} = Critical normal force coefficient delimiting attached flow

c_n^C = Circulatory normal force coefficient

c_n^I = Noncirculatory (impulsive) normal force coefficient

c_n^P = Normal force coefficient under potential flow conditions

c_n^v = Vortex induced normal force coefficient

$\overline{c}_{n_\alpha}$ = Normal force (lift) curve slope

C_{P_v} = Vortex induced center of pressure

c_v = Vortex lift increment

D, D_p, D_f = Deficiency functions

f = Trailing edge separation point

f', f'' = 1^{rst} and 2^{nd} order temporal lag applied to T.E. separation point

k = Reduced frequency, $\omega b/V$

K = Noncirculatory time constant multiplier

K_0, K_1, K_2 = Coefficients representing pitching moment curve

$k_{n_\alpha}, k_{n_q}, k_{m_\alpha}, k_{m_q}$ = Free parameters

M = Mach number

p = Laplace variable

q = Normalized pitch rate, $\dot{\alpha}c/V$

s = Nondimensional distance traveled by airfoil in semi-chords

S_1, S_2 = Coefficient of separation point curve fit

t = Time, s

$T.F.$ = Transfer function

T = System period

t_I = Universal noncirculatory time constant

t_p, t_f, t_v = Time constants (semi-chords)

t_{vl} = Vortex passage time constant

$t'_{n_\alpha}(M), t'_{n_q}(M, \overline{x}_a)$ = Decay rates (time constants) in the s domain

V = Free stream velocity, m/s

$\overline{x}$ = Aerodynamic state vector

$\overline{x}_a$ = Nondimensional pitching axis location aft of leading edge

x_{ac} = Chordwise location of the aerodynamic center

α = Angle of attack, radian

α_E = Effective angle of attack

β = Prandtl-Glauert compressibility factor, $\sqrt{1 - M^2}$

η = Recovery factor for viscosity effect

ϕ = Indicial response function

SUMMARY

Dynamic stall deeply affects the response of helicopter rotor blades, making its modeling accuracy very important. Two commonly used dynamic stall models were implemented in a comprehensive code, validated, and contrasted to provide improved analysis accuracy and versatility. Next, computational fluid dynamics and computational structural dynamics loose coupling methodologies are reviewed, and a general tight coupling approach was implemented and tested. The tightly coupled computational fluid dynamics and computational structural dynamics methodology is then used to assess the stability characteristics of complex rotorcraft problems. An aeroelastic analysis of rotors must include an assessment of potential instabilities and the determination of damping ratios for all modes of interest. If the governing equations of motion of a system can be formulated as linear, ordinary differential equations with constant coefficients, classical stability evaluation methodologies based on the characteristic exponents of the system can rapidly and accurately provide the system's stability characteristics. For systems described by linear, ordinary differential equations with periodic coefficients, Floquet's theory is the preferred approach. While these methods provide excellent results for simplified linear models with a moderate number of degrees of freedom, they become quickly unwieldy as the number of degrees of freedom increases. Therefore, to accurately analyze rotorcraft aeroelastic periodic systems, a fully nonlinear, coupled simulation tool is used to determine the response of the system to perturbations about an equilibrium configuration and determine the presence of instabilities and damping ratios. The stability analysis is undertaken using an algorithm based on a Partial Floquet approach that has been successfully applied with computational structural dynamics tools on rotors and wind turbines.

The stability analysis approach is computationally inexpensive and consists of post processing aeroelastic data, which can be used with any aeroelastic rotorcraft code or with experimental data.

Chapter I

INTRODUCTION

Rotorcraft systems operate under flight conditions that contain nonlinearities such as transonic shocks, dynamic stall, and interactions with their own wakes. The rotors themselves are nonlinear multibody elastic systems, and an important aspect of their dynamic analysis is to assess their stability to determine the presence and of potential instabilities and the damping ratios of all relevant modes. Modes are considered relevant if they are either lightly damped or if they exhibit instabilities at any relevant flight condition.

If the governing equations of motion for a system can be formulated as linear ordinary differential equations (ODE) with constant coefficients, classical stability evaluation methodologies based on the characteristic exponents of the system can rapidly and accurately provide the system's stability characteristics. For systems described by linear ordinary differential equations with periodic coefficients, Floquet's theory [30, 31] is the preferred approach. While these methods provide excellent results for simplified linear models with a moderate number of degrees of freedom, they become quickly unwieldy as the number of degrees of freedom increases [85]. Therefore, to accurately analyze rotorcraft aeroelastic periodic systems, a formal linearization is virtually impossible. This is a similar problem to that which one faces when attempting to assess stability using experimental data. It led to the need of stability analysis methodologies that process discrete data signals to extract the system modal parameters, rather than using linearized equations of motions which are not available. For rotorcraft and flexible rotating systems in general, a fully nonlinear coupled simulation tool is used to determine their time discrete response to

perturbations about a periodic steady-state equilibrium, and to imitate experimental data with neither its cost nor its deficiencies (e.g. accuracy, setup experimental cost, time, noise, etc.).

Because of the nature of the stability analysis for wind turbines and rotorcraft, the aerodynamics and structural dynamics of these systems are highly interdependent in determining the response of the system. Thus, at each time step of the simulation, the most up-to-date information on both the structural and aerodynamic response is needed. There are two ways to achieve this: either by solving the fluid and structural equations of motion simultaneously [36] or by the exchange of data between the computational fluid dynamics (CFD) and the computational structural dynamics (CSD) codes at each time step (where the time step is sufficiently small to minimize the phase differences in the two sets of data).

Several approaches propose procedures for solving the fluid and structural equations simultaneously. By example, Hübner et al. [36] proposed a monolithic approach to solve the fluid-structure interaction problems using space-time finite elements. The structural motion was described by geometrically nonlinear elastodynamics, and the fluid was modeled by the incompressible Navier-Stokes equations. Their procedure exhibited very good convergence properties with respect to the fully coupled nonlinear solution when it was applied to two-dimensional problems with strong fluid-structure interactions and large structural deformations.

However, although solving the fluid and structural equations of motion simultaneously is the optimal solution, it requires extensive rewrite of existing systems that have been developed to solve structural and fluid equations separately, resulting in a significant cost.

The second method, involving the exchange of data between the CFD and the CSD codes at each time step (known as *tight coupling*), utilizes existing CFD and CSD methods. Thus, it alleviates the need to recreate sophisticated costly codes. Also

tight coupling leverages the existing experience in *loose coupling* CFD/CSD methods. Hence, to obtain adequate data for stability analysis of the aerodynamics system: first the tight coupling is performed to reach a trimmed equilibrium configuration. Then, adequate perturbations are applied to determine the response of the system and the modal parameters using appropriate stability analysis techniques. This method emphasizes the need of an efficient tight coupling process. In other words, an efficient practical automated framework is needed to exchange the data between the CFD and the CSD codes at each time step.

Because the exchange of data between the CFD and the CSD codes at each time step is required by the tight coupling, and because the time step must be sufficiently small to minimize the phase differences in the two sets of data, the tight coupling process is computationally costly. To trim rotor models under the tight coupling, the time required to trim the model should be optimized. Moreover, an efficient method is needed to decrease the number of tight coupling revolutions that are needed to extract the stability characteristics.

The main goal of the work reported in this thesis is to develop an approach that defines each step mentioned above to reach an efficient stability analysis of complex rotor models using CFD/CSD tight coupling.

1.1 Literature Review

1.1.1 Unsteady Aerodynamics Models and Semi-Empirical Dynamic Stall models

Dynamic stall is a phenomenon that deeply affects the response of helicopter rotor blades. Most analysis codes estimate the unsteady airloads by modifying the steady two-dimensional (2-D) wind tunnel experimental tests. However, the accuracy of these computations decreases when the angles of attack increase beyond the static stall angle of attack [14]. The successful design of advanced rotorcraft requires the ability to confidently predict the unsteady and vibratory loads on the rotor system.

Numerical solution of the Navier-Stokes equations has shown some success in capturing dynamic stall. However, those aerodynamics solutions are complex and require very costly computational resources [50]. This difficulty has motivated the development of less expensive semi-empirical theories to model dynamic stall, trading between the accuracy, the simplicity of computation, and the computational cost.

Several semi-empirical dynamic stall models [35,40,49,69,88] have been described and studied, which depend mainly on free parameters that are specified using unsteady wind tunnel test data. Five of these dynamic stall models were studied and contrasted by Bousman [14] to determine their accuracy and reliability in rotorcraft design problems. These five dynamic stall models are those of Johnson [40], Boeing [35], Leishman and Beddoes [47–50, 52], ONERA EDLIN [69], and ONERA BH (Bifurcation de Hopf) [88]. A review summarizing these models is given by Johnson [39]. Two of these models Leishman-Beddoes and ONERA EDLIN, are the most commonly used dynamic stall models and they are studied next.

Using the indicial method, Leishman and Beddoes introduced a generalized model for airfoil unsteady aerodynamic behavior [49]. In their work, they first introduced a linear attached flow model, and then extended it to the non-linear regime by including viscous effects and viscous-inviscid interactions. They considered the separation sources that appear to be involved in most types of airfoil stall, primarily the separation of flow at the airfoil trailing edge. These sources of separation introduce non linearity in the aerodynamics airloads, loss of circulation, and leading edge separation in some cases of modern cambered rotor airfoils. If supercritical flow develops, then the stall will be dominated by shock wave separation. Experimental tests showed that the disturbance associated with flow separation is either at the leading edge or the shock wave, and is usually enough to thicken the boundary layer leading to some trailing edge separation [49]. Leishman and Beddoes [50] refined and improved

their theory and presented it in an engineering framework for implementation in routine rotor aerodynamics codes (to calculate the blade airfoil sectional aerodynamics loads). Leishman et al. [51, 52] introduced the state space form of the equations of the Leishman-Beddoes semi-empirical unsteady aerodynamic model. Leishman gathered the parts and the different stages of this semi-empirical theory, and presented its development stages briefly in reference [48].

The *ONERA-EDLIN* dynamic stall model is described in reference [69], where the original ONERA model is extended to apply to the operating conditions encountered by helicopter rotor blade airfoils. This model is based on a delayed dynamic stall. Second-order linear differential equations are used in this model to compute dynamic stall loads. This model is considered a very simple model compared to the Leishman-Beddoes semi-empirical model based on its computational cost, its accuracy and reliability, and the way it models the physical aspects of the flow during dynamic stall. Stumpf et al. [83, 84] used this model as a part of their integrated finite-state model for the analysis of rotor deformation, computation of the nonlinear airloads, and rotor trimming. This model depends only on two states for the computation of dynamic stall effect for each airload, and hence was convenient for their finite-state equations. Peters et al. [65] implemented this dynamic stall model as a part of an integrated airloads-inflow model for rotor simulation and control analysis.

Several comprehensive aerodynamics codes implemented the whole or a part of the Leishman-Beddoes semi-empirical model and the ONERA-EDLIN dynamic stall model and described their implementations in their code manuals (for example RCAS [3] and CAMRAD [41, 42]).

1.1.2 Quasi-steady trimmer and kriging meta-modeling

The classical autopilot control law [64, 66] is extensively used for trimming rotor models in comprehensive analysis codes. The autopilot consists of a simple control

law that constructs a map relating the inputs to the outputs of the system based on a static approximation to the behavior of the system. It is then easy to compute a suitable set of filter time constants and control gains such that a closed loop controller will steer the system to its trimmed configuration with the desired performance. Peters et al. [66] studied helicopter trimming using an optimized controller, a closed form quasi-steady Jacobian of the plant, and a closed-form mathematical aeroelastic model of the rotor and state space stall model. However, when this control law is used to steer complex rotorcraft models (such as those used in comprehensive analysis codes), a stable behavior is observed only for judiciously chosen values of the controller parameters. The reasons for the observed discrepancy, as identified by Peters et al. [66] in the design of the controller, include:

1. The dynamic characteristics of the plant are ignored.

2. The non-linear behavior of the plant is not usually taken into account. However, when the system identification is carried out more often to update the plant approximated Jacobian, the system nonlinearity is usually better described.

Bauchau et al. [4] studied the implications of these assumptions on the behavior of the classical autopilot to determine their effect through both numerical closed-loop experiments on a realistic UH-60A multibody rotor model (the plant), and eigenvalue analysis of the closed-loop characteristics of different reduced order models of the full plant. Results have been obtained that imply that the inaccurate determination of the Jacobian matrix is one of the causes for the observed lack of stability of the autopilot algorithm at high gains. However, they observed that even if the full dynamic characteristics of the system are accurately modeled, not all of them are controllable and observable, and hence their inclusion in the trimming process will not make progress. Thus, the maximum rate at which the controls could be changed ends up as a characteristic of the system physics, determined by the least damped

uncontrollable mode of the system. In an attempt to increase the rate at which the trimming proceeds (in the light of this observation), a new strategy for trimming, called the quasi-steady trim algorithm, was elaborated. It attempts to trim the rotor in a quasi-steady manner to minimize the excitation of lightly damped modes.

The rotor trimmer acts on the instantaneous time-average values of the airloads and not their instantaneous time values. A Fast Fourier Transform (FFT) is usually used to perform this analysis in DYMORE [5]. However, the exact frequencies of the components of the signal are required.

1.1.3 CFD/CSD Coupling Interface

Computational structural dynamics tools based on finite element methods [5, 39] can provide accurate models of the rotor system structural and control nonlinearities. They have been routinely applied to rotorcraft over the past decade. To minimize the computational cost, these methods typically employ simplified (linearized) aerodynamic models to predict the response of the rotor in specific flight conditions.

Full-scale rotor systems experience strong variations across several Mach regimes during a single revolution at almost all flight conditions of interest. The aerodynamic flow field may be further complicated by the presence of the wake system (which can remain in the vicinity of the rotor), as well as highly-nonlinear dynamic stall dominated by viscous effects. The presence of these aerodynamic nonlinearities calls into question the accuracy of aerodynamic loads obtained from the lower-fidelity simplified aerodynamic models typically found in comprehensive tools.

In the last decade, the use of CFD tools has dramatically increased the accuracy of airloads predictions [2, 73, 80], in particular when they have been coupled with one of the CSD tools that is capable of modeling the blade structural and control system nonlinearities. While the cost of these CFD/CSD coupled methods is greater

than the CSD tools, the availability of low-cost computer clusters with many computational nodes is rapidly bringing the cost of coupled CFD/CSD analyses down to a level where they can be routinely applied by the engineering community. When performing any aeroelastic analysis, the accuracy of the prediction is driven by the weakest link of the analysis, which must include consideration of the structures, dynamics, and aerodynamic modeling. While the linear aerodynamics used routinely in aerodynamic analysis provides efficient turn-around, the aerodynamics of a rotor are highly nonlinear. The use of CFD/CSD coupling can provide an estimate of the nonlinearities of the aerodynamics, hence turning the CFD/CSD coupling methods appropriate methods to perform the stability analysis. However, it is critical to determine the least amount of data necessary to provide accurate stability analysis results without incurring overly costly computations [92].

Phanse et al. [70] used GT-Hybrid/DYMORE tight coupling for UH-60A rotor in a steady level flight. In this work, data exchange occurred through function calls that were made from the CSD solver to the CFD solver which was compiled as a static library. The two codes were compiled together, and GT-Hybrid was called within DYMORE. Although this methodology is efficient, it requires considerable modification of both CFD and CSD solvers.

Rajmohan et al. [75] applied an explicit file Input/Output (I/O) method to exchange data by using flag files, written by both CFD and CSD solvers. The CFD solver was GT-Hybrid, and the CSD solver was DYMORE. The cost of file I/O was tested on an Intel Core 2 Quad 2.4 GHz system and it was estimated to be approximately 2 minutes, about 1% of the time required to run a tight coupling simulation for one revolution. The Fluid Structure Interface (FSI) format, which is the current standard for data exchange in the rotorcraft aeromechanics community, was used in this study. The use of a standard format makes the coupling process generic. The procedure for tight coupling is as follows. The natural modes of the structural model

are evaluated. The equilibrium positions of the blades are used as initial conditions for the forced response simulation. The initial forced response simulation is run without coupling to the CFD solver, where the airloads are computed using the internal aerodynamic model in the CSD code which uses 2-D aerodynamic coefficients table and dynamic inflow. The simulation is run for about 30 rotor revolutions to obtain periodic deformations. At this point, DYMORE writes out a flag file signaling the end of the CSD simulation for one time step; which is monitored by GT-Hybrid. DYMORE uses a time step of 1 azimuth whereas the CFD code uses a time step of 0.05 azimuth because CFD methodology needs a smaller time step to handle the flow transients. Once the CFD simulation is completed for 1 azimuth, the solver writes out the loads and a flag file asking DYMORE to read the data. In the conventional serial-staggered time scheme (CSS) for tight coupling (TC), the loads and motions are exchanged in an explicit fashion hence there could be initial transients that could grow with the time integration. These transients are mitigated by applying a weighted average of CFD and lifting line based loads over 2 revolutions. After 2 revolutions, the internal aerodynamic model is turned off and loads applied on the structural model are identical to the CFD loads. The tight coupling simulations were run on 8 processors of Intel Core 2 Quad 2.4 GHz system. A single iteration (1 azimuth) of CFD/CSD coupling took approximately 20 seconds.

Bhagwat et al. [12] used tightly coupled simulations with OVERFLOW-2 and RCAS for calculation of rotor airloads and structural loads in the UTTAS pull-up maneuver for the UH-60A rotor. The fluid/structures interface framework provides blade elastic defections from the comprehensive analysis to the CFD solver, and it provides back the aerodynamic forces computed by CFD solver to the comprehensive analysis. The FSI framework was extended to exchange the flight conditions between RCAS and OVERFLOW-2. This data exchange is done through file I/O.

Thepvongs et al. [86] developed a high fidelity simulation for the aeroelastic analysis of rotors with actuated flexible airfoils. Their simulation consists of an unstructured Reynolds-Averaged Navier-Stokes (RANS) CFD analysis coupled with a non-linear structural analysis that captures camber deformations. They presented the simulation of scaled BO105 rotor in forward flight using tight coupling of FUN3D and UM/NLABS solvers. In their solution, trimming and convergence to periodic response were assisted by a low-order aerodynamics model consisting of two-dimensional finite-state formulation for flexible airfoils, dynamic wake model, and semi-empirical dynamic stall model.

Lynch and Liu [1, 28, 53, 57] used DYMORE 2 and OVERFLOW-2 loose coupling where the data was exchanged between the solvers though a set of formatted I/O files. Liu [53] added in DYMORE 2 a kinematic and a load interfaces for both loose and tight coupling, based on data exchanged using standard formatted I/O files. In this technique, loose coupling iterations were done manually and not automated, and hence the same technique was not practical for tight coupling runs. The delta-airloads method [72] was used with the loose coupling approach to improve the loose coupling convergence. The validation of their loose coupling interfaces were performed on the UH-60A aircraft for different forward flight conditions such as flight counters 8534 and 9017. Results showed that loose coupling approach converged quickly in terms of aerodynamic loads and control angles, and that the predicted airloads agreed well with the experimental data. The trends of normal force and pitch moment had good agreement with experimental data, but some peak values could not be recovered using loose coupling approach [53].

Sitaraman et al. [81] performed tight coupling simulations between DYMORE and UMTURNS for the UTTAS 11029 maneuver. The CFD approach consists of the solution of the unsteady Reynolds-Averaged Navier-Stokes (URANS) equations for the near-field of the rotor coupled with the dynamics of trailed vortex wake that are

computed using a free vortex method. The CSD approach uses a multibody finite element method to model the rotor hub and blades. Results illustrated the correlation of predicted performance, i.e. the correlation of aerodynamic and structural dynamic loading with measured flight test data. The normal load factor and the peak-to-peak structural and aerodynamic loading showed good correlation with flight test data, indicating that the analysis framework is suitable for preliminary design purposes. Important phenomenon such as advancing blade transonic effects and retreating blade flow separation were satisfactorily predicted. However, deficiencies were noted in the accurate resolution of stall incidence, reattachment and shock induced separation. Coupling of codes was performed using a python based framework where all data exchange is performed using memory pointers rather than file I/O making the coupling process efficient and seamless. The time evolution of the structural, fluid dynamic, and vorticity transport equations are consistently coupled to obtain an aeroelastic solution for the unsteady maneuver. The fluid, structure, and wake equations were integrated using the conventional serial-staggered (CSS) time stepping scheme. The sequence of integration first begins with the CSD solver computing converged blade position using the provided aerodynamic loading; next the wake solver computes new wake locations based on this new blade position, as well as the aerodynamic loading. Once the new blade positions and wake locations are obtained, the fluid equations are integrated to generate the aerodynamic loading for the next time step. This method degrades in accuracy and shows instabilities if large time steps are used. Sitaraman et al. [81] used in their study an azimuthal step of 0.4. Their computations were conducted on a 16 processor cluster with Intel 2.3 MHz. The wall clock time required for the computation in each time step (including both CFD and CSD) was 2.2 seconds.

Nygaard et al. [63] used loose coupling (LC) to provide trimmed solutions to periodic problems, and to exchange information between CFD and CSD models on a periodic basis. They mentioned that using tight coupling to exchange information

throughout the simulation (often every time step) is more useful for unsteady transient maneuvers. By itself, tight coupling was not used to provide for trimmed flight. A restart was used from a well converged LC solution to a TC with fixed controls, and it gave identical results for both loose and tight coupling within engineering accuracy. Hence it appears to be an efficient method of initiating a transient maneuver. A TC transient maneuver with a rapid doublet disturbance to the collective pitch control for the UH-60 case 8534 showed both similarities and significant differences with computations with the CSD model using lifting line aerodynamic.

Yeo et al. [91] used a fully automated OVERFLOW and RCAS coupling. The two codes communicate via flag files written to disk, waiting for each other to finish their tasks, where in loose coupling the task is a complete trimmed rotor revolution. They used tight coupling for the maneuver transient response, where the tight coupling run is initiated from the steady loose coupling simulations.

Usually, when using the loose-coupling strategy, data are exchanged between the two codes at regular intervals (typically after a full revolution of the rotor or a fraction of it) based on the number of rotor blades. In the *delta airloads approach* [72] the CSD solver trims the model based on airloads from the CSD internal linear aerodynamics and a frozen set of CFD loads. This method has been successfully applied for level forward flights. The loose coupling approach with the delta-airloads method represent a computationally efficient technique to obtain a trimmed periodic solution of a rotor in forward flight conditions. An iterative procedure, often involving a trimming analysis, is required to achieve convergent solutions. Therefore, the loose coupling analysis is suitable for periodic problems. In a tight coupling simulation, data are exchanged between the CFD and the CSD solvers at each time step. Tight-coupling strategy is required to validate the loose coupling results and for simulation of maneuvering flights. Tightly coupling is also applied to model rotor transient response. The initial condition applied in the tight coupling is usually the solution obtained from

the last iteration of the loosely coupled simulation, which provides an equilibrium starting point to the tight-coupled analysis.

1.1.4 Stability Analysis

Using CSD tools, Bauchau and Wang [9], along with others [74,82], have reviewed several approaches to stability analysis and their applicability to rotorcraft and other large-scale multibody systems. The complex rotorcraft model is used as a virtual prototype of the actual dynamic system, and a set of *experiments* is run to determine the stability characteristics of the system. Using the moving block analysis [16, 34], Yeo et al. [91] examined RCAS and OVERFLOW 2 coupling to evaluate the stability analysis of the ADM model (Advanced Dynamics Model, an isolated rotor with four hingeless blades flexible in bending and torsion) for several configurations. First, they obtained converged loose coupling solution, and a tight coupling simulation was applied to obtain the ADM model responses to different sets of excitations from the steady periodic simulations. No trimming was done under the tight coupling, where the tight coupling was initiated from the loose coupling solutions as initial conditions. They used the moving block analysis for the stability analysis to extract the regression lead-lag mode damping.

Bauchau and Wang [9] used an algorithm based on a Partial Floquet Analysis (PFA) to extract the stability characteristics of the UH-60A in forward light encounter 8534, using DYMORE 2 solver. Bauchau and Skjolden [82] used the same algorithm to successfully obtain the stability characteristics of wind turbine. In their study, Bauchau and Skjolden [82] applied both the moving window analysis and the Coleman post-processing transform along with the PFA.

1.2 Proposed work and Thesis organization

The main goal of the work reported in this dissertation is to demonstrate the ability of tightly coupled CFD/CSD methodology to assess the stability characteristics of

complex rotorcraft problems with optimized computational cost. Such a goal requires all the pieces contained in the chapters of this thesis together. First to enable an efficient CFD/CSD tight coupling interfaces. Then to obtain a converged trimming solution in forward flight using the kriging meta-modeling along with the proposed quasi-steady trimmer. The stability assessment is undertaken using an algorithm based on the Partial Floquet Approach that has been successfully applied together with CSD tools to helicopter rotors by Bauchau and Wang [9], and to wind turbines by Bauchau and Skjolden [82], and it has been successfully applied to helicopter rotors using tightly coupled CFD/CSD simulations by Zaki et al. [92].

For this effort, kinematic and load interfaces are added to DYMORE version 4 (henceforth will be denoted by DYMORE), to enable its coupling (tight or loose coupling) with any external CFD code directly or through scripting language like Python interface. The coupling is performed by automated data exchange through memory allocation of the required interchanged data, alleviating the need for flags files, or I/O formatted data files as was accomplished previously by Lynch and Liu [1, 28, 53, 57]. Finally, a quasi-steady trimmer along with a kriging meta-model are introduced and compared to the classical autopilot and system identification to enhance the trimming process under tight coupling.

The dissertation is organized in six chapters as follows. First, the thesis background and motivation are introduced in chapter 1.

Then to advance DYMORE aerodynamic modules, the Leishman-Beddoes complete unsteady aerodynamics model and the ONERA EDLIN semi-empirical dynamic stall model are studied and implemented as detailed in chapter 2. The Leishman-Beddoes implementation is first verified for a simple 2-D airfoil experiencing a moderate and a severe dynamic stall cases. After the verification, Leishman-Beddoes model (with some of its coefficients adjusted for airfoil SC-1905) is used to compute the airloads for the UH-60A rotor in forward flight case 9017 (which is known for

dynamic stall effect), and the resultants airloads are compared to the converged loose coupling airloads at the same control settings. The ONERA dynamic stall model is used with Peters model, and it is tested for NACA 0012 symmetric airfoil going trough a light dynamic stall.

The second part of this dissertation, chapters 3-5, deals with the required stages of the problem to reach an efficient stability analysis of rotorcraft in a trimmed forward flight condition using CFD/CSD tight coupling.

Chapter 3 introduces a quasi-steady trimmer along with a kriging meta-model, to enable an efficient fast trimming procedure, and to decrease the required number of CFD/CSD tight coupling revolutions that are needed to reach the trimmed solution. Hence, decreasing the computation cost. Both the quasi-steady trimmer and the ordinary kriging are studied in details. Then they are tested together for the UH-60A rotor in forward flight case 8534.

In chapter 4, the loose and tight coupling procedures are revised, and new load and kinematic interfaces are implemented in DYMORE. This enables both the direct access to the setting of the airstations airloads by the CFD code and the collection of motion solutions to pass to the CFD solver. Also the DYMORE code was modified and organized to enable a simpler way to access its main functions. This code can either be compiled with another CFD code, or it can be called together with the CFD code using a third party code (e.g. Python). A Python interface is hence developed and some of the DYMORE functions were wrapped into Python functions using Swig, to enable this last mentioned CFD/CSD coupling technique. The interfaces were tested for tight coupling, then used for both loose and tight coupling runs for the UH-60A and the ADM models in forward flight for several flight encounters.

In chapter 5, all the problem stages are put together. Using an efficient CFD/CSD tight coupling procedure, and good initial control settings obtained from the kriging

meta-modeling that corresponds to airloads very near to their target values, the trimming process is done during the tight coupling simulation. Once the periodic solution is reached, adequate set of perturbation loads is applied to the rotorcraft blades, an appropriate time is waited to allow the transient behavior to decrease, and then the coupled aeroelastic simulation is allowed to run until the steady periodic flight condition is recovered. Signals are constructed, and then a post-processing stability analysis is undertaken, using both moving windows analysis and multi-blade transform, to identify the modal characteristics of the rotor. This technique has been tested for both the UH-60A case 8534 and the ADM model, first for DYMORE alone runs, then for CFD/CSD coupling runs.

Finally the work done and conclusions are summarized in chapter 6, and the recommendations for future work are enumerated in chapter 7.

Chapter II

UNSTEADY AERODYNAMICS MODEL AND SEMI-EMPIRICAL DYNAMIC STALL MODELS

2.1 Introduction

Dynamic stall is characterized by a delay of the onset of stall due to the formation of a vortex that increases the maximum lift produced beyond that of the static stall case. This increases in the maximum lift is accompanied by corresponding peaks in both the pitching moment and the drag force. The increase in these airloads during dynamic stall needs to be accurately predicted to provide the design procedure with accurate information about the efficiency of the airfoil along with providing the higher airloads that will be applied on the structure during the occurrence of dynamic stall. The main features of the flow field during dynamic stall are illustrated in figures 1 and 2 as described by Leishman and Beddoes [50]. These figures are recreated by the Matlab code implemented based on the theory explained in this chapter.

2.2 Leishman-Beddoes Unsteady Aerodynamics

The two-dimensional unsteady aerodynamic behavior of airfoils described in this section is based on the work of Leishman and Beddoes [47–50, 52]. The Leishman-Beddoes unsteady aerodynamics semi-empirical model for dynamic stall of a 2-D airfoil in subsonic compressible flow consists of three distinct subsystems:

1. An unsteady attached (potential linear) flow conditions solution.

2. A separate flow solution for nonlinear airloads.

3. A dynamic stall solution for the vortex induced airloads.

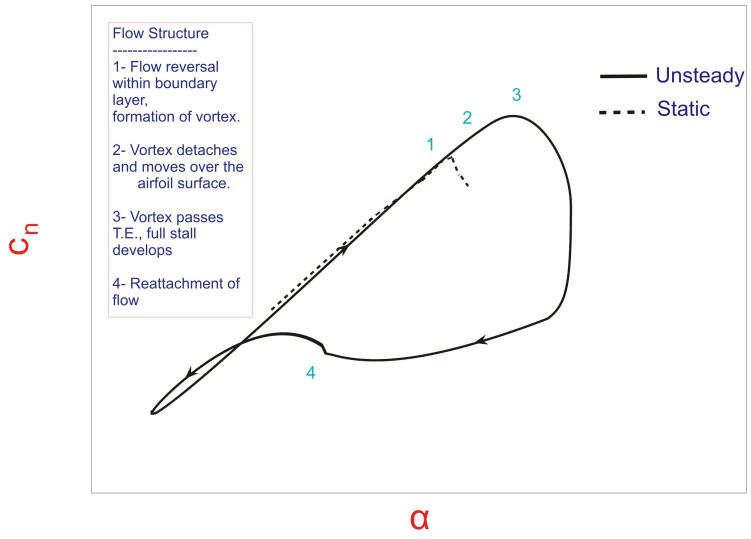

Figure 1: Typical dynamic stall behavior of the lift for 2-D airfoil, adapted for NACA 0012 airfoil

Hence the formulation of the flow solution can be separated into two components: the unsteady behavior of the attached flow and the separated flow behavior. These two aspects of the problem will be examined next.

2.2.1 Unsteady attached flow

The unsteady aerodynamics of a 2-D airfoil under attached flow conditions in a subsonic compressible flow is formulated in terms of the superposition of indicial aerodynamics response. In rotor analysis, the unsteady aerodynamics can result from the plunging and/or the pitching motion of the blade element.

2.2.1.1 ***Indicial response method***

For a general pitching airfoil, two indicial functions are required. The first function corresponds to the uniform perturbation velocity due to the plunging motion. The second function corresponds to the linear variation velocity associated with the angular velocity about the pitch axis. Each indicial function consists of two parts: the circulatory part and the non-circulatory *'impulsive'* part. The circulatory part is

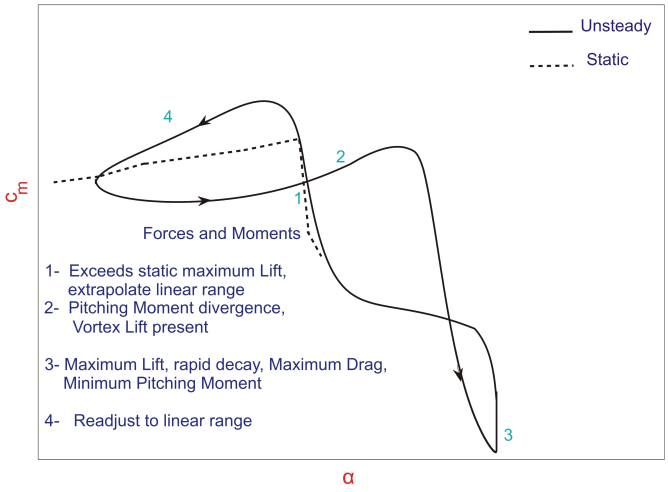

Figure 2: Typical dynamic stall behavior of the pitching moment for 2-D airfoil, adapted for NACA 0012 airfoil

manifested as a gradual asymptotic approach of the indicial part to the final steady state value, dominant at low frequency, and is usually referred to as the *shed wake* term. The non-circulatory part is dominant at high frequency and is usually referred to as the *apparent mass* term. Although the initial and final values for these functions are known exactly from the Piston theory and the linearized subsonic theory [13], their intermediate values are only known at certain values of time. The scaling normally adopted to nondimensionalize time produces the parameter $s = 2Vt/c$ which corresponds to the relative distance traveled by the airfoil in terms of semi-chords, $b = c/2$.

For a step change in angle of attack and pitching rate q (about some reference axis $\overline{x}_a$), the normal force coefficients can be written in the s domain as

$$\triangle c_{n_\alpha}(s, M) = \left[\overline{c}_{n_\alpha}(M)\Phi^C_{n_\alpha}(s, M) + \frac{4}{M}\Phi^I_{n_\alpha}(s, M)\right] \triangle \alpha \tag{1}$$

$$\triangle c_{n_q}(s, M, \overline{x}_a) = \left[\overline{c}_{n_\alpha}(M)\left(\frac{3 - 4\overline{x}_a}{4}\right)\Phi^C_{n_q}(s, M) + \frac{2(1 - 2\overline{x}_a)}{M}\Phi^I_{n_q}(s, M, \overline{x}_a)\right] \triangle q \tag{2}$$

where $\overline{c}_{n_\alpha}(M)$ is the normal force curve slope in the steady flow as function of Mach

number (measured from experiments or computed by CFD solver).

Similarly, the indicial moment response about quarter-chord resulting from a step change in angle of attack α and pitch rate q about the quarter-chord can be written in the s domain as

$$\triangle c_{m_\alpha}(s,M) = \left[\left(\frac{1}{4} - x_{ac}\right)\overline{c}_{n_\alpha}(M)\Phi^C_{n_\alpha}(s,M) - \frac{1}{M}\Phi^I_{m_\alpha}(s,M)\right] \triangle \alpha \tag{3}$$

$$\triangle c_{m_q}(s,M) = \left[\frac{-\pi}{8\beta}\Phi^C_{m_q}(s,M) + \frac{-7}{12M}\Phi^I_{m_q}(s,M)\right] \triangle q \tag{4}$$

where all the indicial functions represent the behavior of the response between $s = 0$ and $s = \infty$.

These functions can be defined for the circulatory lift response as

$$\Phi^C_{n_\alpha}(s,M) = 1 - \sum_{i=1}^{N} A_i \exp(-b_i \beta^\gamma s) \tag{5}$$

where A_i, b_i and γ_i are free parameters subject to the constraint that they are all positive.

For a subsonic compressible flow

$$\Phi^C_{n_q}(s,M) = \Phi^C_{n_\alpha}(s,M) \tag{6}$$

Then, the circulatory indicial lift response for an airfoil pitching about any axis can be obtained from the following transformation:

$$(\Phi^C_{n_q})_{\overline{x}_a}(s,M) = \left(\frac{7 - 4\overline{x}_a}{4}\right)\Phi^C_{n_\alpha}(s,M) \tag{7}$$

If pitching is about quarter-chord, then the equivalent angle of attack is evaluated by

$$\alpha_{eq}(t) = \alpha(t) + \frac{q(t)}{2} = \alpha_{\frac{3}{4}}(t) \tag{8}$$

Similarly, the non-circulatory lift function is

$$\Phi^I_{n_\alpha}(s,M) = \exp\left[\frac{-s}{t'_{n_\alpha}(M)}\right] \tag{9}$$

$$\Phi^I_{n_q}(s, M, \overline{x}_a) = \exp\left[\frac{-s}{t'_{n_q}(M, \overline{x}_a)}\right] \tag{10}$$

where $t'_{n_\alpha}(M)$ is Mach number dependent decay rate in the s domain, while $t'_{n_q}(M, \overline{x}_a)$ time constant depends on both the Mach number and the pitch axis location.

These non-circulatory time constants can be evaluated by equating the sum of the time derivatives of the assumed forms of the non-circulatory and circulatory responses at time zero ($s = 0$) to that of the exact solution obtained by Lomax et al. [54], who suggested an interesting analog with the steady supersonic flow, from which the indicial responses can be calculated explicitly for $0 \leq s \leq \frac{2M}{M+1}$. For the lift response, they can be given as

$$t_{n_\alpha}(M) = k_{n_\alpha}\left(\frac{c}{2V}\right) t'_{n_\alpha}(M) = K_{n_\alpha}(M) t_I \tag{11}$$

$$t_{n_q}(M, \overline{x}_a) = k_{n_q}\left(\frac{c}{2V}\right) t'_{n_q}(M, \overline{x}_a) = K_{n_q}(M, \overline{x}_a) t_I \tag{12}$$

where

$$K_{n_\alpha}(M) = \frac{k_{n_\alpha}}{(1 - M) + \pi\beta^{\gamma-1} M^2 \sum_{i=1}^{N} A_i b_i} \tag{13}$$

$$K_{n_q}(M, \overline{x}_a) = \frac{2k_{n_q}(1 - 2\overline{x}_a)}{(1 - M)(1 - 2\overline{x}_a) + 2\pi\beta^{\gamma-1} M^2 \sum_{i=1}^{N} A_i b_i} \tag{14}$$

and t_I is the universal time constant, given by

$$t_I = \frac{c}{a} \tag{15}$$

k_{n_α} and k_{n_q} are free parameters in the range $0.7 \leq k_{n_\alpha}, k_{n_q} \leq 1.0$. Although these factors modify the initial behavior of the indicial response, they are justified because of additional physical effects such as the airfoil thickness and the minor viscosity effects.

2.2.1.2 ***Optimal selection of the indicial coefficients***

For the optimal selection of the indicial coefficients, the (2N+3) dimensional vector is first defined. This vector consists of all the coefficients and the poles used in the

indicial response functions including the exponent γ and the factors k_{n_α} and k_{n_q}

$$X^T = [A_1, A_2, \ldots, A_N; b_1, b_2, \ldots, b_N; \gamma; k_{n_\alpha}; k_{n_q}] \tag{16}$$

Then, the value of this vector is chosen through an optimization algorithm to minimize the difference between the explicit solution based on the assumed indicial response approximations given above and the experimental measurements of the unsteady response in the frequency domain which must be known for I values of Mach numbers at L values of reduced frequency each. The constraints on this vector are

$$A_i, b_i, \gamma > 0 \qquad i=1,2,\ldots,N \tag{17}$$

$$0.7 \leq k_{n_\alpha}, k_{n_q} \leq 1.0 \tag{18}$$

$$\sum_{i=1}^{N} A_i = 1 \tag{19}$$

It was found that only two circulatory poles, $N=2$, were sufficient to obtain satisfactory results [49] and that the values obtained for γ were consistently close to 2. So, in this study only two poles will be considered and γ will be set equal to 2.

The indicial pitching moment response at the quarter-chord can be obtained similarly to the lift response. Finally, the indicial lift response in the time domain for input α and q (about any axis $\overline{x}_a$) can be summarized as

$$c^C_{n_\alpha}(t) = \overline{c}_{n_\alpha} \left[1 - A_1 \exp\left(-\frac{\beta^2 t}{T_1}\right) - A_2 \exp\left(-\frac{\beta^2 t}{T_2}\right)\right] \tag{20}$$

where $T_i = \frac{c}{2Vb_i}$, for $i = 1, 2$

$$c^I_{n_\alpha}(t) = \frac{4}{M} \exp\left(-\frac{t}{t_{n_\alpha}}\right) \tag{21}$$

$$c^C_{n_q}(t) = \overline{c}_{n_\alpha} \left(\frac{3 - 4\overline{x}_a}{4}\right) \left[1 - A_1 \exp\left(-\frac{\beta^2 t}{T_1}\right) - A_2 \exp\left(-\frac{\beta^2 t}{T_2}\right)\right] \tag{22}$$

$$c^I_{n_q}(t) = \frac{2(1-2\overline{x}_a)}{M}\exp\left(-\frac{t}{t_{n_q}}\right) \tag{23}$$

The indicial pitching moment about quarter-chord for input of the angle of attack and pitching rate about quarter-chord axis ($\overline{x}_a$=0.25) can be expressed as

$$c^C_{m_\alpha}(t) = \overline{c}_{n_\alpha}(0.25 - x_{ac})\left[1 - A_1\exp\left(-\frac{\beta^2 t}{T_1}\right) - A_2\exp\left(-\frac{\beta^2 t}{T_2}\right)\right] \tag{24}$$

$$c^I_{m_\alpha}(t) = \frac{-1}{M}\left[A_3\exp\left(-\frac{t}{b_3 t_{m_\alpha}}\right) + A_4\exp\left(-\frac{t}{b_4 t_{m_\alpha}}\right)\right] \tag{25}$$

where

$$t_{m_\alpha}(M) = K_{m_\alpha}(M)t_I\ ,\ K_{m_\alpha}(M) = \frac{(A_3 b_4 + A_4 b_3)k_{m_\alpha}}{b_3 b_4(1-M)} \tag{26}$$

$$c^C_{m_q}(t) = \frac{-\pi}{8\beta}\left[1 - A_5\exp(-b_5\beta^2\frac{2V}{c}t)\right] \tag{27}$$

$$c^I_{m_q}(t) = \frac{-7}{12M}\exp\left(-\frac{t}{t_{m_q}}\right) \tag{28}$$

$$t_{m_q}(M) = K_{m_q}(M)t_I\ ,\ K_{m_q}(M) = \frac{7k_{m_q}}{15(1-M) + 3\pi\beta M^2 A_5 b_5} \tag{29}$$

Experimental results show that $k_{n_\alpha}, k_{n_q} \approx 0.75$, while $k_{m_\alpha}, k_{m_q} \approx 0.8$.

By taking the Laplace transform of all the above indicial responses in the p–domain, knowing that the initial value of the circulatory indicial functions are equal to zero: $\Phi^C(0) = 0 = (1 - \sum_{i=1}^{N} A_i)$ (their transfer function is the Laplace transform of their impulse response). The transfer functions of the indicial responses are expressed as

$$T.F.[c^C_{n_\alpha}] = \overline{c}_{n_\alpha}\beta^2\left[\frac{A_1}{T_1}\left(\frac{1}{p + \frac{\beta^2}{T_1}}\right) + \frac{A_2}{T_2}\left(\frac{1}{p + \frac{\beta^2}{T_2}}\right)\right] \tag{30}$$

$$T.F.[c^I_{n_\alpha}] = \frac{4}{M}\left(\frac{t_{n_\alpha} p}{1 + t_{n_\alpha} p}\right) \tag{31}$$

$$T.F.[c^C_{n_q}] = \overline{c}_{n_\alpha}\beta^2\frac{(3-4\overline{x}_a)}{4}\left[\frac{(A_1T_2+A_2T_1)\,p+(A_1+A_2)\,\beta^2}{(T_1T_2)\,p^2+(T_1+T_2)\,\beta^2 p+\beta^4}\right] \tag{32}$$

$$T.F.[c^I_{n_q}] = \frac{2(1-2\overline{x}_a)}{M}\left(\frac{t_{n_q}p}{1+t_{n_q}p}\right) \tag{33}$$

$$T.F.[c^C_{m_\alpha}] = (0.25-x_{ac})\overline{c}_{n_\alpha}\beta^2\left[\frac{A_1}{T_1}\left(\frac{1}{p+\frac{\beta^2}{T_1}}\right)+\frac{A_2}{T_2}\left(\frac{1}{p+\frac{\beta^2}{T_2}}\right)\right] \tag{34}$$

$$T.F.[c^I_{m_\alpha}] = \frac{-1}{M}\left[\frac{A_3\,(b_3t_{m_\alpha})\,p}{(b_3t_{m_\alpha})\,p+1}+\frac{A_4\,(b_4t_{m_\alpha})\,p}{(b_4t_{m_\alpha})\,p+1}\right] \tag{35}$$

$$T.F.[c^C_{m_q}] = \frac{-\pi A_5b_5\beta V}{4c}\left[\frac{1}{p+2b_5\beta^2\frac{V}{c}}\right] \tag{36}$$

$$T.F.[c^I_{m_q}] = \frac{-7}{12M}\left(\frac{t_{m_q}p}{t_{m_q}p+1}\right) \tag{37}$$

From these transfer functions, the responses to general inputs $\alpha(t)$ and $q(t)$ (about quarter-chord) can be written in the state space form.

2.2.1.3 ***State equations form and attached flow equations summary***

The complete formulation of the unsteady behavior of the attached flow leads to the following set of first order ordinary differential equations

$$\dot{\underline{x}} = A\underline{x}+B\underline{u}, \quad \underline{y} = C\underline{x}+D\underline{u}, \tag{38}$$

where $\underline{u}$ is the input array, $\underline{y}$ the output array, and $\underline{x}^T = \lfloor x_1, x_2, ..., x_8\rfloor$ the state array.

The input array is defined as

$$\underline{u} = \left\{\begin{array}{c}\alpha(t)\\ q(t)\end{array}\right\}, \tag{39}$$

where the components of the relative flow velocity at quarter-chord along unit vectors $\bar{a}_2$ and $\bar{a}_3$ are U_2 and U_3, respectively, $\bar{a}_2$ is the unit vector along the zero-lift line direction pointing positive towards the airfoil leading edge (L.E.), and $\bar{a}_3$ is the sectional unit vector normal to $\bar{a}_2$ and to the span wise airfoil unit vector $\bar{a}_1$. The angle of attack α is defined as $\arctan(U_3/U_2)$ measured in radians from the zero-lift line as shown in figure 3, and $q = \dot{\alpha}c/V$ is the normalized pitch rate counted positive for nose up motion.

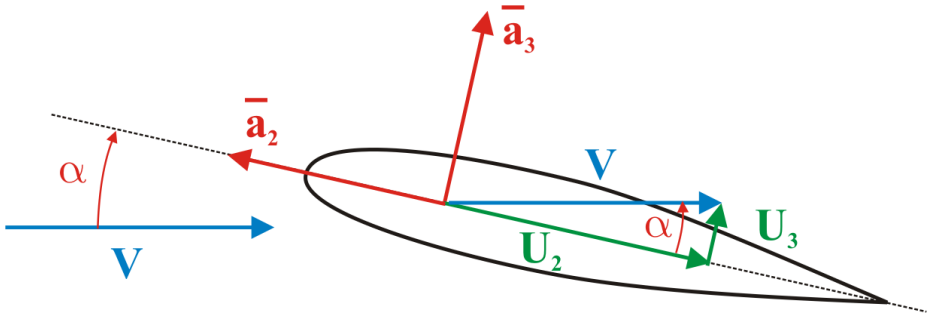

Figure 3: Relative velocity of the flow with respect to the quarter-chord point.

The output array is defined as

$$\underline{y} = \left\{ \begin{array}{c} c_n^p(t) \\ c_m(t) \end{array} \right\}, \tag{40}$$

where c_n^P is the normal force coefficient under potential flow conditions, and c_m is the quarter-chord pitching moment coefficient. Once a solution has been obtained for theses two coefficients, the effective angle of attack of the airfoil due to the shed wake terms can be written in terms of the states x_1 and x_2 as

$$\alpha_E(t) = \beta^2 \left(\frac{V}{b}\right) (A_1 b_1 x_1 + A_2 b_2 x_2). \tag{41}$$

The chord force and pressure drag coefficients, shown in figure 4, are then found as

$$c_c(t) = \eta\, \bar{c}_{n_\alpha} \alpha_E^2(t) \tag{42}$$

$$c_d(t) = c_n^p \sin\alpha - c_c \cos\alpha \tag{43}$$

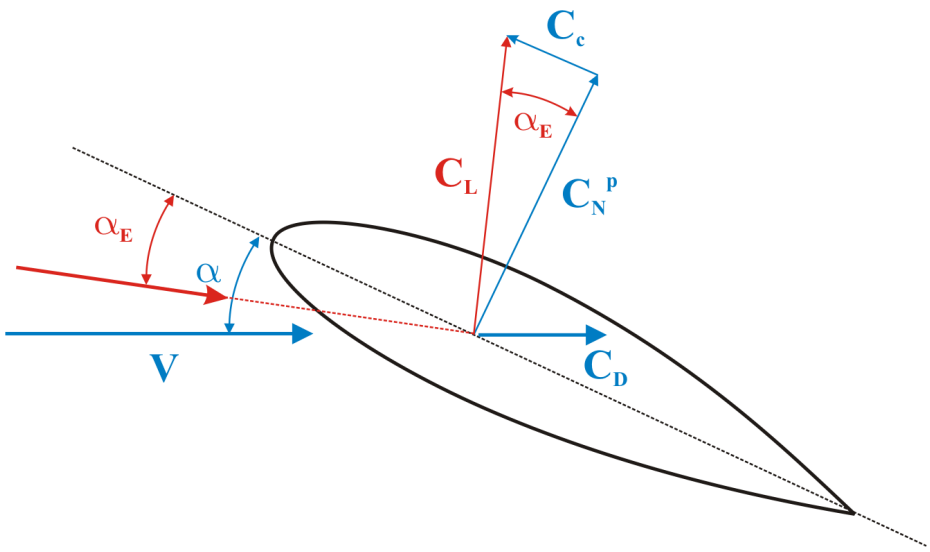

Figure 4: Definition of the chord force and pressure drag coefficients.

respectively. The total section drag is obtained by adding the profile drag forces.

The governing equations, eqs. (38), involve four matrices. The diagonal matrix A is

$$A_{8\times 8} = -\text{diag}\left(\frac{V\beta^2 b_1}{b}, \frac{V\beta^2 b_2}{b}, \frac{1}{t_{n_\alpha}}, \frac{1}{t_{n_q}}, \frac{1}{b_3 t_{m_\alpha}}, \frac{1}{b_4 t_{m_\alpha}}, \frac{V\beta^2 b_5}{b}, \frac{1}{t_{m_q}}\right). \tag{44}$$

While the rectangular matrices B and C are

$$B_{8\times 2} = \begin{bmatrix} 1 & 0.5 \\ 1 & 0.5 \\ 1 & 0 \\ 0 & 1 \\ 1 & 0 \\ 1 & 0 \\ 0 & 1 \\ 0 & 1 \end{bmatrix}, \tag{45}$$

$$C_{2\times 8} = \begin{bmatrix} (V/b)\bar{c}_{n_\alpha}\beta^2 A_1 b_1 & (0.25 - x_{ac})(V/b)\bar{c}_{n_\alpha}\beta^2 A_1 b_1 \\ (V/b)\bar{c}_{n_\alpha}\beta^2 A_2 b_2 & (0.25 - x_{ac})(V/b)\bar{c}_{n_\alpha}\beta^2 A_2 b_2 \\ -4/(Mt_{n_\alpha}) & 0 \\ -1/(Mt_{n_q}) & 0 \\ 0 & A_3/(Mb_3 t_{m_\alpha}) \\ 0 & A_4/(Mb_4 t_{m_\alpha}) \\ 0 & (-\pi A_5 b_5 \beta V)/(8b) \\ 0 & 7/(12Mt_{m_q}) \end{bmatrix}^T \tag{46}$$

respectively. Finally, the square matrix D is

$$D_{2\times 2} = \frac{1}{M}\begin{bmatrix} 4 & 1 \\ -(A_3 + A_4) & -7/12 \end{bmatrix}. \tag{47}$$

Typically, the value of the recovery factor for viscosity effect η is ≈ 0.95, and for inviscid flow $\eta = 1$.

The coefficients of circulatory indicial response functions are denoted $A_i, i = 1, 2, \ldots, 5$. In the absence of unsteady test data, the values of these coefficients can be taken from refs. [47,52], as shown in table 1 which lists different sets of coefficients from various sources. Note that $A_2 = (1 - A_1)$.

Table 1: Indicial response coefficients

Data Source	A_1	A_2	A_3	A_4	A_5
Boeing Data	0.636	0.364	1.5	-0.5	1.0
ARA Data	0.625	0.375	1.5	-0.5	1.0
NASA Data	0.482	0.518	1.5	-0.5	1.0
Consolidated Data	0.918	0.082	1.5	-0.5	1.0

For the results listed in table 1, the Boeing data were obtained from unsteady test run in a 4×4 ft wind tunnel for free-stream Mach numbers of 0.2, 0.4, and 0.6 and for fairly wide range of reduced frequencies. Two airfoil shapes were included in the study: the symmetric NACA 0012 airfoil and the cambered NACA 23010 airfoil. This data set is quite unique since a few measurements were made at the very high reduced

frequency of 0.72, albeit at lowest Mach number. On the other hand, the ARA data set was obtained from unsteady test run in an 18×8 in intermittent blowdown wind tunnel for the NACA 0012 airfoil. The data cover a range of Mach numbers from 0.3 to 0.75, but only up to reduced frequencies 0.25. Nevertheless, relatively high reduced frequencies were tested at higher Mach numbers of 0.7 and 0.75. Finally, the NASA data set was obtained by Davis and Malcolm [27] from the NASA facility for a supercritical NACA 64A010 airfoil. This data set was recorded for Mach numbers of 0.5 and 0.8, and for small angle of attack oscillations at reduced frequencies up to 0.3.

The exponents or poles of the circulatory indicial response functions are denoted $b_i, i = 1, 2, \ldots, 5$. In the absence of unsteady test data, the values of these coefficients can be taken from refs. [47, 52], as shown in table 2 which lists different sets of coefficients from same sources mentioned previously.

Table 2: Indicial response coefficients

Data Source	b_1	b_2	b_3	b_4	b_5
Boeing Data	0.339	0.249	0.25	0.1	0.5
ARA Data	0.310	0.312	0.25	0.1	0.5
NASA Data	0.684	0.235	0.25	0.1	0.5
Consolidated Data	0.366	0.102	0.25	0.1	0.5

It is clear from tables 1 and 2 that the indicial response coefficients and exponents strongly depend on the actual experimental data set used. Thus, in view of the limited data from any source, the results from the various tests were consolidated into one data set which covers Mach numbers from 0.2 up to 0.8, and is mainly for reduced frequencies up to 0.3.

Also, from reference [11], $A_1 = 0.3, A_2 = 0.7, b_1 = 0.14$ and $b_2 = 0.53$ and their generalization to different Mach numbers is accomplished through the scaling of the exponents by β^2 the Prandtl-Glauert compressibility factor. $\beta = \sqrt{1 - M^2}$ [11] will be used in the implementation of the model. The non-circulatory time constant

multiplier are denoted $k_{n_\alpha}, k_{n_q}, k_{m_\alpha}$ and k_{m_q}. In the absence of available unsteady test data, the following empirical data can be used $k_{n_\alpha} \approx 0.75$, $k_{n_q} \approx 0.75$, $k_{m_\alpha} \approx 0.8$ and $k_{m_q} \approx 0.8$.

Finally, the non-circulatory time constants are

$$t_I = \frac{2b}{a} \tag{48}$$

$$K_{n_\alpha} = \frac{k_{n_\alpha}}{(1-M) + \pi\beta M^2 \sum_{i=1}^{2} A_i b_i}, \qquad t_{n_\alpha} = K_{n_\alpha} t_I \tag{49}$$

$$K_{n_q} = \frac{k_{n_q}}{0.5(1-M) + 2\pi\beta M^2 \sum_{i=1}^{2} A_i b_i}, \qquad t_{n_q} = K_{n_q} t_I \tag{50}$$

$$K_{m_\alpha} = \frac{k_{m_\alpha}(A_3 b_4 + A_4 b_3)}{b_3 b_4 (1-M)}, \qquad t_{m_\alpha} = K_{m_\alpha} t_I \tag{51}$$

$$K_{m_q} = \frac{7 k_{m_q}}{15(1-M) + 3\pi\beta M^2 A_5 b_5}, \qquad t_{m_q} = K_{m_q} t_I \tag{52}$$

2.2.2 Separated flow behavior

To solve for the separated flow behavior, the following inputs need to be added to the model, where in the absence of available test data, their values can be taken from table 3. The theory for separated flow and dynamic stall model is presented in refs. [49–51].

First, α_1, S_1 and S_2 are used in the formulation of the trailing edge separation point f as function of the angle of attack as following. From the airfoil static $c_n - \alpha$ data, the following relation could be constructed, where f is defined as fraction of the airfoil chord

$$f = \left[2\sqrt{\frac{c_n}{\bar{c}_{n_\alpha}(M)\alpha}} - 1 \right]^2 \tag{53}$$

Then $f-\alpha$ static relation is curve-fitted to two expressions before and after the static stall as following

$$f = \begin{cases} 1 - 0.3\ \exp((\alpha - \alpha_1)/S_1) & \alpha \leq \alpha_1 \\ \\ 0.04 + 0.66\ \exp((\alpha_1 - \alpha)/S_2) & \alpha > \alpha_1 \end{cases} \tag{54}$$

where S_1, S_2 and α_1 are three empirical parameters which may be fitted to the test data. α_1 is the break point corresponding to $f \approx 0.7$ (closely correspond to the static stall angle of attack for most airfoil sections). Their values in table 3 are in degrees.

This $f - \alpha$ static relation must be modified to account for negative angles of attack, as shown in reference [42]

$$f = \begin{cases} 1 - 0.3\ \exp((|\alpha| - \alpha_1)/S_1) & |\alpha| \leq \alpha_1 \\ \\ 0.04 + 0.66\ \exp((\alpha_1 - |\alpha|)/S_2) & |\alpha| > \alpha_1 \end{cases} \tag{55}$$

Next set of inputs to the Leishman-Beddoes theory for the separated flow model are $k_0,\ k_1,\ k_2$, and z. These constants are used in the computation of c_m/c_n ratio when the separated flow is encountered. First, the static c_m/c_n ratio is formulated from the airfoil static test data as function of the angle of attack. Compute the T.E. separation point f at the same angles of attack using eq. (55), then c_m/c_n as function of f could be curve-fitted

$$c_m/c_n = k_0 + k_1(1 - f) + k_2\ \sin(\pi f^z) \tag{56}$$

where $k_0 = (0.25 - x_{ac})$ is aerodynamic center offset from the quarter chord, k_1 represents the direct effect of the growth of the separated flow region on the center of pressure, and k_2 helps describe the shape of the moment break at stall. The values of k_0, k_1, k_2 and z can be adjust to give the best moment reconstruction. z will be taken equal to 2.0 in the implementation of the model.

Next set of inputs are denoted $t_p(M)$ and $t_f(M)$ which are Mach number dependent time constants used in the separated flow behavior.

Table 3: Airfoil coefficients for unsteady separated flow modeling for NACA 0012

M	0.30	0.40	0.50	0.60	0.70	0.75	0.80	Units
α_1	15.25	12.5	10.5	8.5	5.6	3.5	0.7	degree
$\delta\alpha_1$	2.1	2.0	1.45	1.0	0.8	0.2	0.1	degree
S_1	3.0	3.25	3.5	4.0	4.5	3.5	0.7	degree
S_2	2.3	1.6	1.2	0.7	0.5	0.8	0.18	degree
k_0	0.0025	0.006	0.02	0.038	0.03	0.001	-0.01	non-dim.
k_1	-0.135	-0.135	-0.125	-0.12	-0.09	-0.13	0.02	non-dim.
k_2	0.04	0.05	0.04	0.04	0.15	-0.02	-0.01	non-dim.
t_p	1.7	1.8	2.0	2.5	3.0	3.3	4.3	non-dim.
t_f	3.0	2.5	2.2	2.0	2.0	2.0	2.0	non-dim.

Both t_p and t_f are weak Mach number dependent variables. From the experimental results, it appears that the values of t_p are largely independent of airfoil shape 3. On the other hand, it is more difficult to determine how t_f changes with airfoil shape, and without access to unsteady airfoil data an unsteady boundary layer code can be practically used to determine how t_f varies with airfoil shape.

The components of the output vector $\underline{y}$, eq. 40, need to be split into their circulatory and noncirculatory parts where each part is defined as function of the states or the states time derivatives

$$\underline{y} = \begin{bmatrix} c_n^p(t) \\ \\ c_m(t) \end{bmatrix} = \begin{bmatrix} c_n^C(t) + c_{n_\alpha}^I(t) + c_{n_q}^I(t) \\ \\ c_{m_\alpha}^C(t) + c_{m_\alpha}^I(t) + c_{m_q}^C(t) + c_{m_q}^I(t) \end{bmatrix}. \tag{57}$$

where

$$c_n^C(t) = \bar{c}_{n_\alpha}\alpha_E(t). \tag{58}$$

$$c_{n_\alpha}^I(t) = \frac{4}{M}\dot{x}_3. \tag{59}$$

$$c_{n_q}^I(t) = \frac{1}{M}\dot{x}_4. \tag{60}$$

$$c_{m_\alpha}^C(t) = k_0 c_{n_\alpha}^C(t). \tag{61}$$

$$c^I_{m_\alpha}(t) = \left(\frac{-1}{M}\right)\left[A_3\dot{x}_5 + A_4\dot{x}_6\right]. \tag{62}$$

$$c^C_{m_q}(t) = \left(\frac{-\pi A_5 b_5 \beta V}{8b}\right) x_7. \tag{63}$$

$$c^I_{m_q}(t) = \left(\frac{-7}{12M}\right)\dot{x}_8. \tag{64}$$

The time derivatives of the states are taken from eq. (38). Note that the circulatory or the noncirculatory part of c^p_n and c_m could be calculated as previously shown, then using eq. 57 to compute the other part.

The circulatory part of the normal force coefficient due to angle of attack, $c^C_{n_\alpha}(t)$, is calculated similarly to eqs.(41-58) as

$$c^C_{n_\alpha}(t) = \overline{c}_{n_\alpha}\beta^2\left(\frac{V}{b}\right)(A_1 b_1 \widehat{x}_1 + A_2 b_2 \widehat{x}_2). \tag{65}$$

where these two new states are defined as

$$\dot{\widehat{x}_i} = A(i,i)\widehat{x}_i + \alpha(t), i = 1, 2. \tag{66}$$

where $A(i,i)$ is the i^{th} diagonal term of matrix A (eq. (44)). Also these two states can be computed numerically from the corresponding first two states of the attached flow solution by extracting the effect of the pitch rate $q(t)$.

2.2.2.1 ***Leading edge separation effect***

Under unsteady conditions, the normal force coefficient $c_n(t)$ lags $\alpha(t)$ and the leading edge pressure response lags $c_n(t)$. Therefore the critical pressure for separation onset (stall) at the appropriate Mach number is achieved at a higher angle of attack than the quasi-static case, and there is an overall delay in the onset of dynamic stall.

To implement the critical pressure criterion under unsteady conditions, a first order lag is applied to $c^p_n(t)$ to produce a subsonic value $c'_n(t)$. Defining i as the current time sample, this first order lag is accomplished as following

$$D_{p_i} = D_{p_{i-1}}E_p + (c^C_{n_i} - c^C_{n_{i-1}})E_p^{0.5}. \tag{67}$$

where

$$E_p = \exp\left(\frac{-\Delta s}{t_p}\right) \tag{68}$$

then

$$c'_{n_i} = c^p_{n_i} - D_{p_i}. \tag{69}$$

where $s = Vt/b$ is the non-dimensional distance traveled by the airfoil in semi-chords, $\Delta s = s_i - s_{i-1}$, and $c^p_{n_i}$ is the total unsteady normal force coefficient for attached flow. The equation for c'_{n_i} can be written in the form of a state equation as reference [51]

$$\dot{x}_9 = \left(\frac{-x_9}{t_p}\right) + \left(\frac{c^p_n(t)}{t_p}\right). \tag{70}$$

$$c'_n(t) = x_9. \tag{71}$$

2.2.2.2 ***Trailing edge separation effect***

There can exist a modified trailing edge separation point location due to temporal effects on the airfoil pressure distribution and the boundary layer response. An open loop procedure is formed to represent the time dependent effects on the trailing edge separation point f eq. (54) and thereby permits the evaluation of nonlinear forces and moments under dynamic conditions via the application of Kirchhoff theory. The procedure is performed as following. First, define an effective angle of attack $\alpha_f(t)$ which gives the same unsteady leading edge pressure as for the equivalent quasi-steady case

$$\alpha_f(t) = \frac{c'_n(t)}{\overline{c}_{n_\alpha}(M)}. \tag{72}$$

Using this effective angle of attack, determine a value for the trailing edge separation point f' from the static $\alpha - f$ relationship (eq. 54). However when the angle of attack is decreasing the static hysteresis around stall is modeled using an empirically derived dynamic offset $\Delta\alpha_{1_i}$ [49]

$$\Delta\alpha_{1_i} = \begin{cases} \left((1 - f''_{i-1})^{0.25}\delta\alpha_1\right) & S_\alpha < 0 \\ 0 & S_\alpha >= 0 \end{cases} \tag{73}$$

where $\delta\alpha_1$ is function of the airfoil shape and Mach number, as given in table 3, and $S_\alpha = (\alpha_i - \alpha_{i-1})$ is used to detect the angle of attack is increasing or decreasing with time (pitch up or down). The unsteady trailing edge (T.E.) separation point f'' used here is from the previous time step (eq. 78) that will be defined next. Finally, α_1 is calculated as

$$\alpha_{1_i} = \alpha_1 - \Delta\alpha_{1_i} \tag{74}$$

so that

$$f' = \begin{cases} 1 - 0.3\,\exp\left[(|\alpha_f| - \alpha_{1_i})/S_1\right] & |\alpha_f| \le \alpha_{1_i} \\ 0.04 + 0.66\,\exp\left[(\alpha_{1_i} - |\alpha_f|)/\,S_2\right] & |\alpha_f| > \alpha_{1_i} \end{cases} \tag{75}$$

Additional effects of the unsteady boundary layer response may be represented by applying a first-order lag to f' to produce a final value for the unsteady trailing edge separation point f''. The deficiency function given by

$$D_{f_i} = D_{f_{i-1}} E_f + (f'_i - f'_{i-1}) E_f^{0.5}. \tag{76}$$

where

$$E_f = \exp\left(\frac{-\sigma_1 \Delta s}{t_f}\right) \tag{77}$$

$\sigma_i,\ \ i = 1, 2, 3$ are three time constants parameters and their values will be specified at each time step to solve the interaction between the different flow features.

The dynamic T.E. separation point is calculated from

$$f''_i = f'_i - D_{f_i}. \tag{78}$$

Alternatively, this additional lag in the T.E. separation point can be represented in a state space formulation [51] as

$$\dot{x}_{10} = \left(\frac{-x_{10}}{t_f}\right) + \left(\frac{f'(t)}{t_f}\right). \tag{79}$$

$$f''(t) = x_{10}. \tag{80}$$

Finally, the nonlinear normal force coefficient c_n^f incorporating the effect of the unsteady trailing edge separation point f'' can be given by

$$c_{n_i}^f = c_{n_i}^{fC} + c_{n_i}^I. \tag{81}$$

where $c_{n_i}^{fC}$ is the circulatory part of the normal force coefficient including the separated flow effect and is computed from

$$c_{n_i}^{fC} = K_{n_i} c_{n_i}^C \tag{82}$$

where

$$K_{n_i} = \frac{(1+\sqrt{f_i''})^2}{4} \tag{83}$$

and the noncirculatory normal force coefficient computed from eqs.(59, 60) is

$$c_{n_i}^I = c_{n_{\alpha_i}}^I + c_{n_{q_i}}^I. \tag{84}$$

Similarly, the pitching moment coefficient is given by

$$c_{m_i}^f = \left[k_0 + k_1(1-f_i'') + k_2 \sin(\pi f_i^{"m})\right] c_{n_{\alpha_i}}^{fC} + c_{m_{q_i}}^C + c_{m_i}^I + c_{m_0} \tag{85}$$

where c_{m_0} is the zero lift pitching moment, and $c_{n_{\alpha_i}}^{fC}$ is the circulatory part of the normal force coefficient due to angle of attack including the separated flow effect eq. 66. $c_{n_{\alpha_i}}^{fC}$ is computed similarly to eq. 82 as

$$c_{n_{\alpha_i}}^{fC} = K_{n_i} c_{n_{\alpha_i}}^C \tag{86}$$

and the noncirculatory moment coefficient computed from eqs.(62, 64) as

$$c_{m_i}^I = c_{m_{\alpha_i}}^I + c_{m_{q_i}}^I \tag{87}$$

Finally, the chord force coefficient $c_{c_i}^f$ and the pressure drag coefficient $c_{d_i}^f$ for separated flow are given respectively as

$$c_{c_i}^f = \eta\, \bar{c}_{n_\alpha}(M) \alpha_{E_i}^2 \sqrt{f_i''} \tag{88}$$

and

$$c_{d_i}^f = c_{n_i}^f \sin\alpha - c_{c_i}^f \cos\alpha. \tag{89}$$

Next section will study the effect of adding dynamic stall vortex effect.

2.2.2.3 ***Dynamic stall effect***

Dynamic stall involves the formation of a vortex near the leading edge of the airfoil, which separates from the surface and is transported downstream. A physically accepted model for the vortex induced lift has been formulated by viewing the vortex lift contribution as an excess accumulation of circulation in the vicinity of the airfoil until some critical condition is reached.

This model takes its input from the previous two sections for unsteady aerodynamic attached and separated flow. The following inputs need to be added for the formulation of dynamic stall effect for Leishman-Beddoes theory, where in the absence of available unsteady test data, their values can be taken from table 4.

The critical normal force coefficient c_{n_1}, may be obtained from an analysis of airfoil static test data. c_{n_1} corresponds to the critical pressure for separation onset at the appropriate Mach number. In practice, it can be obtained from the static value of c_n that corresponds to either the break in pitching moment or the chord force at stall [50].

The vortex decay constant $t_v(M)$ and the center of pressure travel time constant $t_{vl}(M)$ appear in table 4 to be relatively independent of Mach number over most of the Mach number range. Dynamic stall experiments show that while there is a significant effect of airfoil shape under light stall conditions, all airfoils behave similarly under strong dynamic stall conditions. Thus, it can be concluded that the parameters t_v and t_{vl} should be relatively insensitive to the airfoil shape.

Table 4: Airfoil coefficients for dynamic stall modeling for NACA 0012

M	0.30	0.40	0.50	0.60	0.70	0.75	0.80	Units
c_{n_1}	1.45	1.2	1.05	0.92	0.68	0.5	0.18	non-dim.
t_v	6.0	6.0	6.0	6.0	6.0	6.0	4.0	non-dim.
t_{vl}	7.0	9.0	9.0	9.0	9.0	9.0	9.0	non-dim.
D_f	8.0	7.75	6.2	6.0	5.9	5.5	4.0	non-dim.

Finally, the constant D_f is needed to empirically model the increased rate at which

the chord force is lost (and hence the onset of drag divergence) after the onset of the gross separation of flow in dynamic stall.

As described previously, the general case of dynamic stall involves the formation of a vortex near the airfoil leading edge, which at certain point in time, separates and convects downstream. The onset of leading edge separation for subcritical flow, or shock induced separation for higher Mach number flow, under dynamic conditions will be initiated when $c'_n(t)$ eq. (69) exceeds the critical $c_{n_1}(M)$ boundary.

At this point there is a catastrophic loss of the leading edge suction, and the accumulated vortex lift is assumed to start to convect over the airfoil chord [51]. Then τ_v, a non-dimensional vortex time parameter (in semi-chords), is used to track the position of the convected vortex such that $\tau_v = 0$ at the onset of separation conditions, and $\tau_v = t_{vl}$ when the vortex reaches the trailing edge, computed from eq. (110). Experimental tests [50] show that the rate of vortex convection is less then half the free-stream velocity with a weak dependence on the Mach number. Vortex speed can be calculated as $V_{vortex} = 2V/t_{vl}$ [42].

For discretely sampled system, the vortex lift force coefficient c_n^v could be computed by assuming that the increment in vortex lift c_v is determined by eq. (90) for a given sample period

$$c_{v_i} = D_s c_{n_i}^C (1 - K_{n_i}) \tag{90}$$

where K_{n_i} is from eq. (83), and $c_{n_i}^C$ from eq. (58). Then the total accumulated vortex lift can be calculated from

$$c_{n_i}^v = c_{n_{i-1}}^v E_v + D_s (c_{v_i} - c_{v_{i-1}}) E_v^{0.5} \tag{91}$$

where

$$E_v = \exp\left(\frac{-\sigma_2 \Delta s}{t_v}\right) \tag{92}$$

where σ_2 is a time constant parameter, and D_s is a switch that takes at the beginning its value from the previous time step, and after that its value is zero unless any of

the following conditions is met, where D_s equals unity [42, 51].

1. $0 < \tau_v \leq t_{vl}$; or

2. $|c'_n| < c_{n_1}$ and $\Delta f'' < 0$; or

3. $S_\alpha > 0$ and $\Delta f'' > 0$.

where τ_v is a the non-dimensional vortex time parameter, $\Delta f'' = \left(f''_i - f''_{i-1}\right)$ is computed at the end of the time step to be used for the next time step to detect the separating flow $\Delta f'' < 0$, or the reattaching flow $\Delta f'' > 0$.

Alternatively, the accumulated vortex lift can be calculated from the following state space equations [51]

$$\dot{x}_{11} = \left(\frac{-x_{11}}{t_v}\right) + D_s \left(\frac{\dot{c}_v}{t_v}\right) \tag{93}$$

$$c_n^v(t) = x_{11} \tag{94}$$

Based on analysis of experimental data involving dynamic stall over wide range of Mach numbers, a representation of the center of pressure behavior (aft quarter-chord) was formulated empirically if $(0 < \tau_v \leqslant 2t_{vl})$ as

$$C_{P_v} = 0.25 \left(1 - \cos(\frac{\pi \tau_v}{t_{vl}})\right). \tag{95}$$

otherwise its default value is 0.

The increment in pitching moment about the quarter-chord due to the aft-moving center of pressure is given by

$$c_m^v = -C_{P_v} c_n^v. \tag{96}$$

The total loading can be computed using superposition. The total normal force and pitching moment coefficients under dynamic stall conditions are given by

$$c_n(t) = c_n^f(t) + c_n^v(t) \tag{97}$$

$$c_m(t) = c_m^f(t) + c_m^v(t) \tag{98}$$

After the onset of the gross separation, Kirchhoff modification for the chord force (eq. 88) becomes invalid, and another procedure that ensures the continuity of its behavior is used

$$c_{c_i} = \eta\, \bar{c}_{n_\alpha}(M)\alpha_{E_i}^2 \sqrt{f_i''}\, \Phi \tag{99}$$

where Φ is defined by

$$\Phi = \begin{cases} 1 & |c_n'| \le c_{n_1} \\ (f_i'')^{min(D_f(|c_n'|-c_{n_1}),1)} & |c_n'| > c_{n_1} \end{cases} \tag{100}$$

and the constant D_f values for different Mach numbers can be taken from table 4.

The pressure drag coefficient, shown in figure 4, is found similarly to eq.89 using

$$c_d(t) = c_n(t)\sin\alpha - c_c(t)\cos\alpha \tag{101}$$

As mentioned before, the total section drag is obtained by adding the profile drag forces.

2.2.2.4 ***Flow reattachment***

Flow is allowed to reattach from deep stall after a reasonable time delay $\tau_v > 2t_{vl}$ during the presence of the vortex. However, this condition is superseded whenever $|c_n'(t)| < c_{n_1}$. The model changes during reattachment are completed through modifications of the time constants parameters σ_1, σ_2 and σ_3. In addition, the pitching moment coefficient is calculated using a different quasi-steady T.E. separation point f_{qs}. Thus, for $c_m(t)$ calculation [3, 49]

$$f_m^r = \begin{cases} f' & S_\alpha \ge 0 \\ f_{qs} & S_\alpha < 0 \end{cases} \tag{102}$$

where

$$f_{qs} = \begin{cases} 1 - 0.3\, \exp\left[(|\alpha| - \alpha_{1_i})/S_1\right] & |\alpha| \le \alpha_{1_i} \\ 0.04 + 0.66\, \exp\left[(\alpha_{1_i} - |\alpha|)/\, S_2\right] & |\alpha| > \alpha_{1_i} \end{cases} \tag{103}$$

with

$$D^r_{f_i} = D^r_{f_{i-1}} E_m + (f^r_{m_i} - f^r_{m_{i-1}}) E^{0.5}_m \tag{104}$$

where

$$E_m = \exp\left(\frac{-\sigma_3 \Delta s}{t_f}\right). \tag{105}$$

then

$$(f''_i)^r = f^r_{m_i} - D^r_{f_i}. \tag{106}$$

and the pitching moment coefficient, similar to eq. 85, is given by

$$c^f_{m_i} = \left[k_0 + k_1(1 - (f''_i)^r) + k_2 \sin(\pi((f''_i)^r)^z)\right] K_{nr_i} c^C_{n_{\alpha_i}} + c^C_{m_{q_i}} + c^I_{m_i} + c_{m_0}. \tag{107}$$

where

$$K_{nr_i} = \frac{(1 + \sqrt{(f''_i)^r})^2}{4}. \tag{108}$$

2.2.2.5 ***Time constants modification***

As mentioned before, to solve the interaction between the different parts of the theory, the time constants t_f and t_v will be modified at each time step through the values of their parameters σ_1, σ_2 and σ_3 (with two different parameters for t_f for both the force and the moment coefficients to account for their different behavior during flow reattachment).

Those parameters default values are $\sigma_1 = 1, \sigma_2 = 1$ and $\sigma_3 = 5$. At the beginning of each time step their values from previous the time step are used, then their values are updated at the end of each time step. The time constants values will be determined based on the flow is separating or reattaching i.e. the sign of $\Delta f''$, the angle of attack is increasing or decreasing i.e. the sign of S_α, and on the phase of the flow itself as shown in figure 5 [3, 42, 49].

The constant *FlagState* is used to determine the initiation of dynamic stall phase ($|c'_n| \geq c_{n_1}$) to compute the non-dimensional vortex travel time τ_v. At the onset of dynamic stall τ_v value is computed as [42]

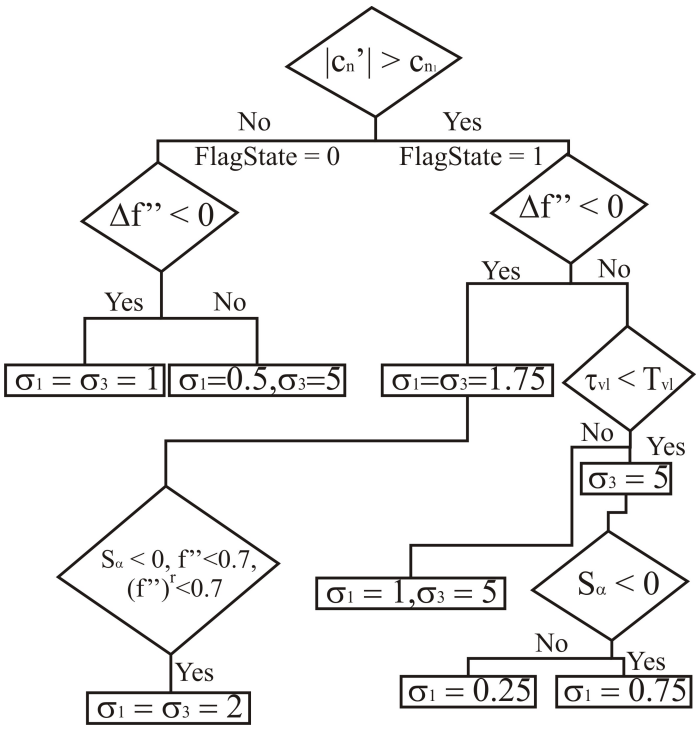

Figure 5: Leishman-Beddoes σ_1 and σ_3 time constants modification

$$\tau_v = \Delta t \left(\frac{V}{b}\right) \left(\frac{|c'_{n_i}| - c_{n_1}}{|c'_{n_i}| - |c'_{n_{i-1}}|}\right). \tag{109}$$

where V is the relative flow velocity in the plane of the airfoil. After that, its accumulation during vortex travel, as long as $FlagState = 1$, is computed simply from

$$\tau_{v_i} = \tau_{v_{i-1}} + \Delta t \frac{V}{b}. \tag{110}$$

For dynamic stall model, the determination of the value of σ_2 is shown in figure 6.

2.2.3 Implementation testing

To test the Leishman-Beddoes model, it was implemented first in Matlab and two tests runs were carried to validate it.

1. ***Unsteady attached flow***

   Consider a 2-D airfoil pitching at a sinusoidal small angle of attack where the flow is unsteady attached flow. Results obtained by Leishman-Beddoes, Peters

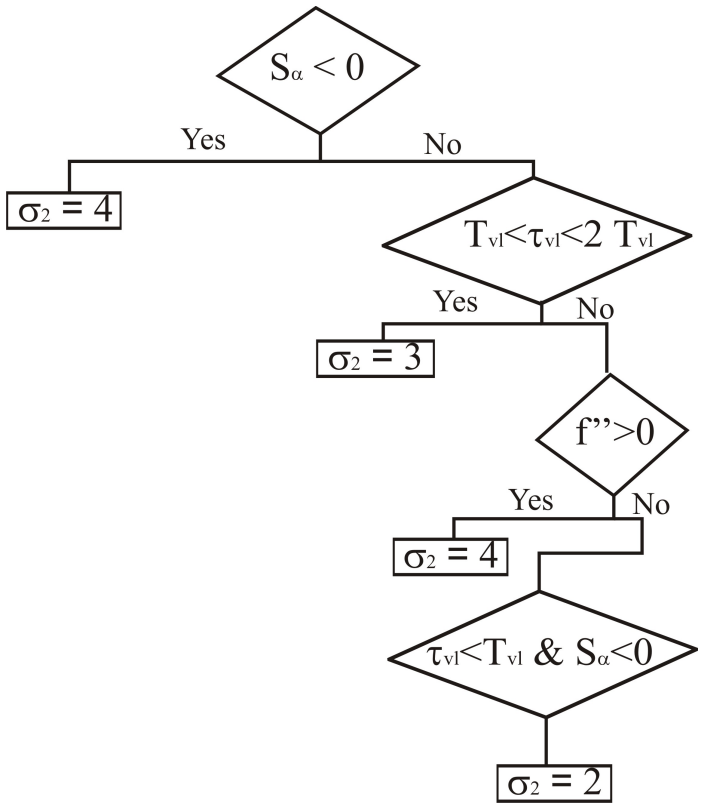

Figure 6: Leishman-Beddoes σ_2 time constant modification

[68], and Theodorsen [13] models are compared for small reduced frequency $k = 0.1$. Results are shown in figures 7-8. Figures 7 and 8 show that Leishman-Beddoes unsteady attached flow solutions were very close to those obtained by both Peters and Theodorsen models at small angle of attack and at small reduced frequency as expected.

2. ***Deep Dynamic Stall Case***

A deep dynamic stall case was carried to validate the theory against the published results [50]. This test run is performed on a NACA 0012 symmetric airfoil pitching at a sinusoidal angle of attack with reduced frequency $k = 0.075$, magnitude $\alpha = 8$ degree, and $\alpha_0 = 10.3$ degree, at 0.38 Mach number. Leishman-Beddoes model constants and parameters were taken from tables 1 and 2. The rest of the constants are determined as shown in table 5 using NACA 0012

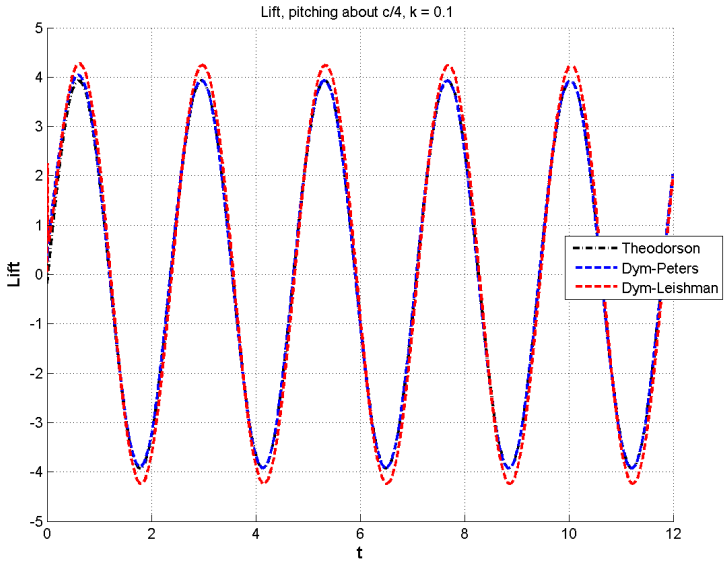

Figure 7: Normal force per unit span computed by Leishman-Beddoes, Peters and Theodorsen for k = 0.1.

static wind tunnel test data. The model predictions for normal force, pitching moment and drag force coefficients are presented in figures 9, 10 and 11 respectively, compared to the corresponding airloads of reference [50]. The results obtained matched well the published results, and the small discrepancy might be due to that some of the coefficients were not mentioned clearly in the paper and had to be guessed through trials of different combinations of their values from the available data tables, and also might be due to the fact that the input to the published results were the angles of attack as measured in the experiment which were not published in the paper.

2.2.4 Leishman-Beddoes airloads equations summary

Section 2.2.1.3 represents the state space form of the attached flow equations. Equations (81)-(89), and eq. (107) represent Leishman-Beddoes separated flow final airloads. Dynamic stall vortex effect are incorporated in eq. (97)-eq. (101), and eq. (107). Summary of the I/O stream for each of Leishman-Beddoes modules is shown in figure 12.

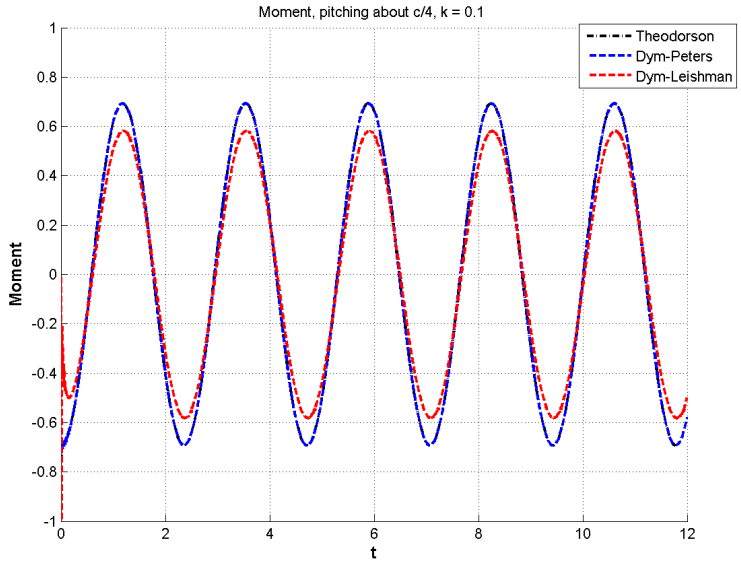

Figure 8: Moment per unit span computed by Leishman-Beddoes, Peters and Theodorsen for k = 0.1.

2.3 The ONERA EDLIN *Dynamic Stall model*

This model is described in reference [65, 69], where the original *ONERA* model is extended for application to the operating conditions encountered by helicopter airfoils. This model is based on a delayed dynamic stall, and second-order linear differential equations are used to compute dynamic stall loads. The second-order differential

Table 5: Leishman-Beddoes coefficients for dynamic stall modeling for NACA 0012.

Parameter	Value
k_0	0.006
k_1	-0.135
k_2	0.05
z	2
c_{n_1}	1.2
α_1	12.5 degree
S_1	3.25 degree
S_2	1.6 degree

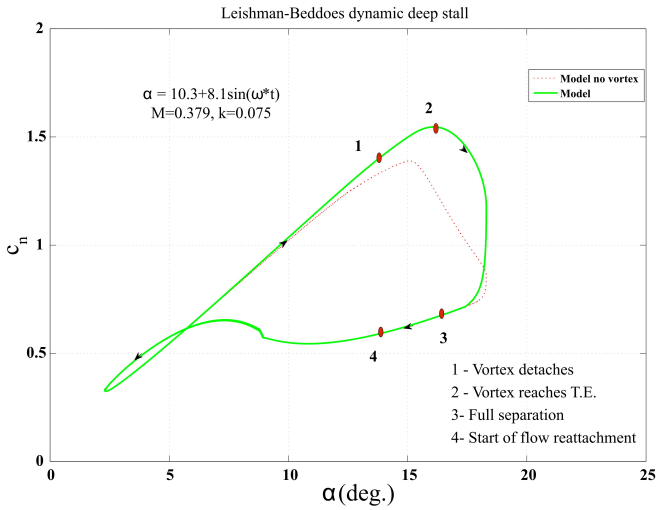

(a) c_n calculated by Leishman-Beddoes model implementation.

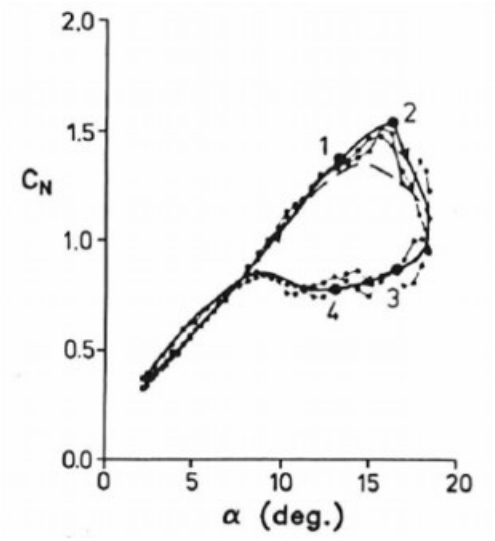

(b) c_n from Leishman-Beddoes reference [50].

Figure 9: Leishman-Beddoes prediction of c_n during deep dynamic stall at M = 0.4.

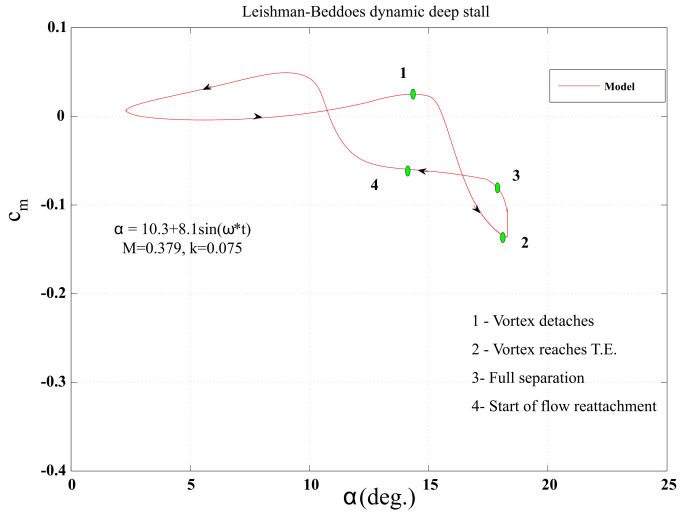

(a) c_m calculated by Leishman-Beddoes model implementation.

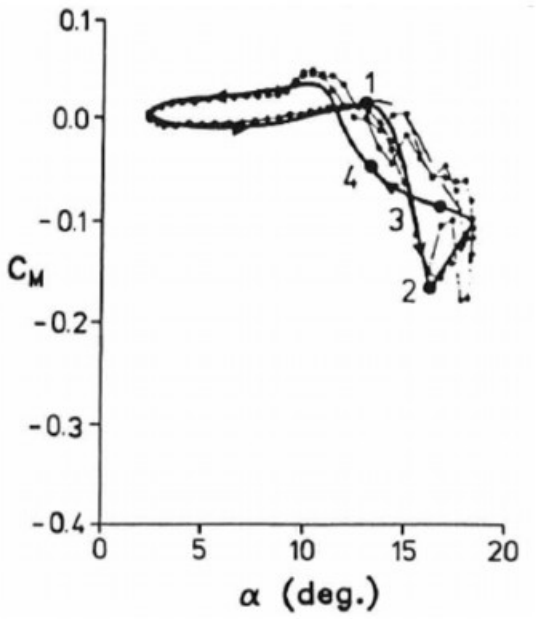

(b) c_m from Leishman-Beddoes reference [50].

Figure 10: Leishman-Beddoes prediction of c_m during deep dynamic stall at M = 0.4.

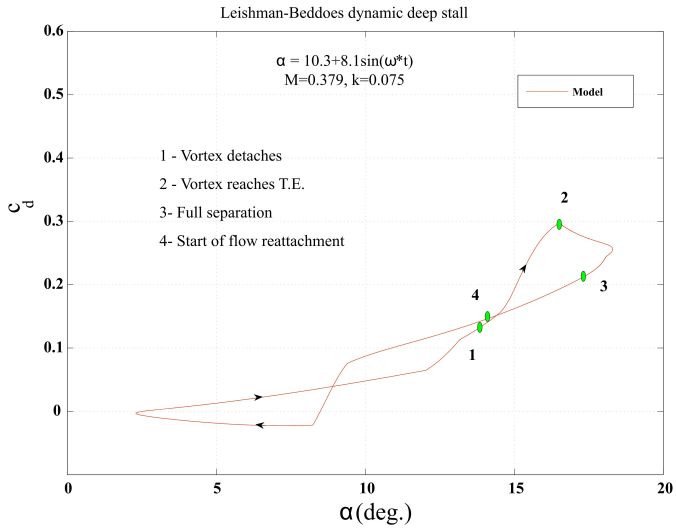

(a) c_d calculated by Leishman-Beddoes model implementation.

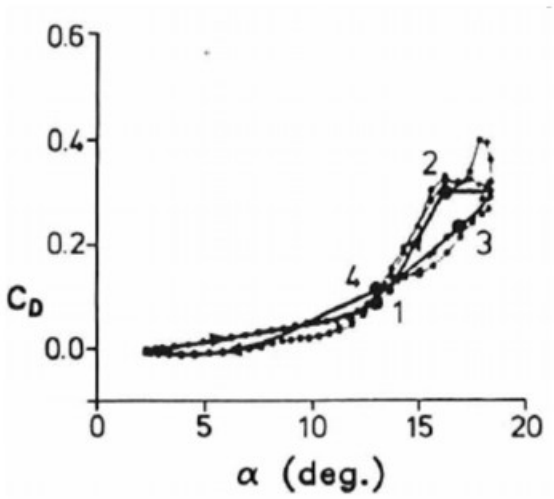

(b) c_d from Leishman-Beddoes reference [50].

Figure 11: Leishman-Beddoes prediction of c_d during deep dynamic stall at M = 0.4.

equations that govern this model are in the form of

$$\frac{d^2\Gamma_i}{dt^2} + \eta_i \left(\frac{V}{b}\right) \frac{d\Gamma_i}{dt} + \omega^2 \left(\frac{V}{b}\right)^2 \Gamma_i = -V\omega^2 \left(\frac{V}{b}\right)^2 \Delta c_i - e_i \left(\frac{V}{b}\right) \frac{d\alpha}{dt}. \tag{111}$$

where Γ is the circulation, $i = l, m, d$ corresponding to lift, moment and drag equations respectively, Δc_i is the difference in the aerodynamic coefficient between its linear static value extrapolated in the stalled region and its real measured value at the angle of attack considered. η_i and e_i are parameters that depend on Δc_l according to

$$\eta_i = \eta_{0i} + \eta_{1i} \Delta c_l^2 \tag{112}$$

$$e_i = e_{0i} + e_{1i} \Delta c_l^2 \tag{113}$$

Experiments show that the parameter ω is the same for the lift, drag and moment equations and depends also on Δc_l according to

$$\omega = \omega_0 + \omega_1 \Delta c_l^2. \tag{114}$$

The values of these parameters can be taken from table 6 [42, 69].

To transform each second-order differential equation in two first-order equations for load i, the following variable is defined

$$\Gamma_{2i} = \frac{d\Gamma_{1i}}{dt}. \tag{115}$$

Then eq. 111can be written as

$$\frac{d\Gamma_{2i}}{dt} + \eta_i \left(\frac{V}{b}\right) \Gamma_{2i} + \omega^2 \left(\frac{V}{b}\right)^2 \Gamma_{1i} = -V\omega^2 \left(\frac{V}{b}\right)^2 \Delta c_i - e_i \left(\frac{V}{b}\right) \frac{d\alpha}{dt}. \tag{116}$$

Using second order finite difference in time, eq. 115 can be written as

$$\Gamma_{2i} = \frac{\Gamma_{2iI} + \Gamma_{2iF}}{2} = \frac{\Gamma_{1iF} - \Gamma_{1iI}}{\Delta t} \tag{117}$$

or

$$\Gamma_{2iF} = 2\frac{\Gamma_{1iF} - \Gamma_{1iI}}{\Delta t} - \Gamma_{2iI} \tag{118}$$

Table 6: *ONERA* Dynamic Stall Coefficients

Equation	Parameter	Range	Default Value
lift, drag, and moment	ω_0	0.1 : 0.4	0.2
	ω_1	0.0 : 0.5	0.2
lift	η_{0l}	0.1 : 0.4	0.3
	η_{1l}	0 : 0.6	0.2
	e_{0l}	0.0	0.0
	e_{1l}	0.0 : -0.2	-0.05
	τ_{d_l}	8.0	8.0
drag	η_{0d}	0.0 : 0.5	0.25
	η_{1d}	0.0 : 0.6	0.0
	e_{0d}	0.0	0.0
	e_{1d}	0.0 : -0.05	-0.015
	τ_{d_d}	0.003	0.0
moment	η_{0m}	0.0 : 0.4	0.25
	η_{1m}	0.0 : 0.6	0.1
	e_{0m}	0.0	0.0
	e_{1m}	0.0 : 0.06	0.01
	τ_{d_m}	2.0	2.0

where the subscript I denotes the value of the variable at the beginning of the time step, and F denotes its value at the end of the time step. Similarly, eq. 116 can be written as

$$\frac{\Gamma_{2iF}-\Gamma_{2iI}}{\Delta t}+\eta_i\left(\frac{V}{b}\right)\frac{\Gamma_{2iF}+\Gamma_{2iI}}{2}+\omega^2\left(\frac{V}{b}\right)^2\frac{\Gamma_{1iF}+\Gamma_{1iI}}{2}= -V\omega^2\left(\frac{V}{b}\right)^2\Delta c_i-e_i\left(\frac{V}{b}\right)\frac{\Delta\alpha}{\Delta t}. \tag{119}$$

Introducing the following variables

$$tr_0=\frac{2}{\Delta t}+\eta_i\left(\frac{V}{b}\right),\quad tr_1=\frac{\Delta t\omega^2}{2}\left(\frac{V}{b}\right)^2. \tag{120}$$

then substitute from eqs.(118, 120) in eq. 119 and rearranging, the following equation is obtained

$$\Gamma_{1iF}=\frac{(C_2\Gamma_{1iI}+2\Gamma_{2iI}-\Delta tC_3)}{C_1}. \tag{121}$$

where

$$C_1=tr_0+tr_1C_2=tr_0-tr_1 \tag{122}$$

$$C_3 = \begin{cases} 0 & \tau \leq \tau_{d_i} \\ \\ \dfrac{2Vtr_1\Delta c_i}{\Delta t} + e_i\left(\dfrac{V}{b}\right)\dfrac{\Delta\alpha}{\Delta t} & \tau > \tau_{d_i} \end{cases} \tag{123}$$

τ is the non-dimensional time, as computed by eq. (110) after the angle of attack exceeds the static stall value α_1, and τ_{d_i} is the time delay for airload i (different value of stall delay for the lift, drag and moment) and can be taken from table 6.

Once the circulations are solved for, the corresponding dynamic stall aerodynamic coefficients are computed as

$$c_l^{DS} = \frac{\Gamma_l}{V} \tag{124a}$$

$$c_d^{DS} = \frac{\Gamma_d}{V} \tag{124b}$$

$$c_m^{DS} = \frac{\Gamma_m}{V} + \frac{1}{4}C_l^{DS}\frac{V}{|V|}. \tag{124c}$$

The airloads due to dynamic stall can be computed as

$$l^{DS} = \rho V b \Gamma_l \tag{125a}$$

$$d^{DS} = \rho V b \Gamma_d \tag{125b}$$

$$m^{DS} = 2\rho V b^2 \Gamma_m + \frac{b}{2}l^{DS}\frac{V}{|V|}. \tag{125c}$$

The second term in the moment equation accounts for reverse flow.

A test run using Peters and ONERA models

The ONERA EDLIN model depends on the solution of two first order ODE for each airload as was shown previously. The coefficients of these first order ordinary differential equations are semi-empirical parameters that need to be specified for each airfoil case. Since the solution of the ODE depend mainly on its coefficients, this leaves the reliability of the ONERA EDLIN dynamic stall model results questionable despite the model itself low computational cost and simplicity. The following test run was performed to proof the sensitivity of ONERA EDLIN simple dynamic stall model to the specified values of its semi-empirical parameters.

Consider a NACA 0012 symmetric airfoil of chord length $c = 6$ m, at Mach number $M = 0.2$, pitching at rotation prescribed as a sinusoidal angle about 0 degree with magnitude $\alpha = 13.7$ degree and reduced frequency $k = 0.07$. Airloads per unit span were computed using Peters model [68] and ONERA EDLIN dynamic stall model. Results are shown in figures 13-15. These results were obtained by including the airfoil static table data, and setting the static stall angle of attack to 13 degree as extracted from the airfoil static experimental data at $M = 0.2$. The obtained results show that the lift and the drag forces obtained by Peters model are comparable to those computed when adding the ONERA dynamic stall model to the computed Peters airloads, i.e. the computed changes in lift and drag airloads due to this case of light dynamic stall, were small changes. This is expected for this case of light stall encountered by the airfoil. However, large differences are observed for the computed moment, which means that adding dynamic stall effect resulted in a large moment variation, which is questionable for this case of light dynamic stall. This last observation might be due to that ONERA model parameters were selected to be the default values form table 6, which might be very different from the parameters for NACA 0012 airfoil used in this test run specially for the pitching moment airload. To identify if the parameters used in this test run are comparable to those for NACA 0012 airfoil, the airloads coefficients predicted by Peters model and those predicted by Peters model corrected with ONERA dynamic stall model, are plotted versus the angle of attack α in figures 16-18. On the same plots, the corresponding available static wind tunnel test data for NACA 0012 are plotted. Figure 16 shows that ONERA model was able to capture the cyclic behavior of dynamic stall in the loops of $c_l - \alpha$ relation. However, the model was unable to predict the onset of dynamic stall correctly as it should be delayed from that for the static stall. This shows that indeed ONERA dynamic stall model results are sensitive to the values of its parameters even for this case of light dynamic stall.

It is important to note that dynamic stall effect on the pitching moment is more critical then its effect on the lift and drag airloads, mainly as the pitching moment is affected by two of the main features that are encountered during dynamic stall. These two features are the change in lift values and the change in the center of pressure location as the vortex associated with dynamic stall is shed over the airfoil surface. More study needs to be done to confirm this observation, specially for test cases where the exact ONERA EDLIN parameters for the airloads are determined, to be used in the test runs, which will increase the reliability of the results obtained, and hence the reliability of the drawn conclusions based on it.

2.4 Leishman-Beddoes and ONERA models observations

For small angles of attack, it was shown that the results of Leishman-Beddoes attached flow predicted airloads were in good agreement to the airloads computed using both Peters and Theodorsen theories as was shown previously in section 2.2.3. The strength of dynamic stall vortex depends directly upon both the amplitude of the angle of attack and the reduced frequency. However when the stall occurs these parameters' effect on $c_{n_{max}}, c_{m_{min}}$ and $c_{d_{max}}$ become negligible [14]. Both ONERA and Leishman-Beddoes semi-empirical models have different sets of parameters that need to be specified, and it is not a trivial task to find a test run where these parameters are accurately defined specially as dynamic stall becomes severe.

Leishman et al. [50] showed that by increasing the reduced frequency for the same nominal angle of attack, the amount of flow separation can be suppressed. Although the lift loss during the flow reattachment will still affect the airloads and the nominally elliptical loops characterizing the airloads and angle of attack relations that are usually obtained under attached unsteady flow conditions. In this case, the concept explained in the simplified steps of this semi-empirical model will not anymore hold. As the reduced frequency decreases, as the flow behavior becomes

more close to the quasi-steady case, and on the other hand, there is a maximum value for the reduced frequency after which the flow simplified behavior described here breaks down. Another region where this theory breaks down is when the angle of attack stays high enough such that a full flow reattachment will not be possible and only partial flow reattachment might occur.

Clark [19] studied the Leishman-Beddoes unsteady aerodynamics model for SC-1095 airfoil at high Mach numbers. McAlister et al. [60] showed that the ONERA model accuracy decreases as dynamic stall becomes severe with the increasing of both the reduced frequency and the amplitude of the angle of attack. The semi-empirical models studied in this chapter do not include some important parameters like the blade sweep and the three dimensional effects (blade tip effects), nor the effect of trailing edge flap.

2.5 Comparing Leishman-Beddoes and Peters models to CFD/CSD loose coupling airloads

The Leishman-Beddoes model was used along with airfoil airtables to compute the airloads for the UH-60A high altitude case 9017, with the controls being fixed at the loose coupling converged control settings (this test case is studied in details in section 4.2.3). For the Leishman-Beddoes semi-empirical model, some of its coefficients were set to values modified for airfoil SC-1905. First, the indicial response functions, the indicial response poles and the time constant multipliers are chosen from reference [19] and shown in table 7. Clark [19] used C-81 tables for SC-1095 airfoil to derive the empirical constants of Leishman-Beddoes model, and when not enough data points were available to obtain a reliable curve-fit, he used a spline to fit the data. For the remaining coefficients of Leishman-Beddoes model, two different sets of values were considered from references [19] and reference [51], as compared in table 8. The profile drag coefficient c_{d_0} was set to 0.01 for both cases.

The obtained airloads were compared to those using Peters model without dynamic stall model. The loads of DYMORE alone are compared to the loose coupling airloads at the loose coupling run converged controls from section 4.2.3). Results are shown in table 9.

Table 7: Leishman-Beddoes indicial coefficients and poles adjusted for airfoil SC-1905

Indicial response coefficients	0.482	0.518	1.5	-0.5	1.0
Indicial response exponents	0.684	0.235	0.25	1.0	0.5
Time constant multipliers	0.75	0.75	0.8	0.8	–

Table 8: Leishman-Beddoes coefficients used in Case 1 and Case 2 test runs for UH-60A case 9017

Parameter	Case 1 : Clark [19]	Case 2: Leishman et al. [51]
$\overline{c}_{n_\alpha}$	6.1077	6.3025
α_1	12.9 deg	15.5 deg
S_1	0.9896 deg	1.1 deg
S_2	3.435 deg	1.1 deg
k_0	-0.0001	0.003
k_1	-0.1277	-0.13
k_2	0.0306	0.04
c_{m_0}	-0.01	-0.0236
η	1.0	0.97
c_{n_1}	1.22	1.55
t_p	1.7	1.7
t_f	3.0	3.0
t_v	6.0	6.0
t_{vl}	7.0	6.75

These results show that only small differences were predicted in the airloads of DYMORE alone when the Leishman-Beddoes semi-empirical model was added, as compared to the airloads computed by the Peters aerodynamics model. The airloads computed by DYMORE alone for the UH-60A flight case 9017 are different from the loose coupling airloads, specially for both the roll and pitch moments, which are more than an order of magnitude different. Thus using the advanced Leishman-Beddoes semi-empirical dynamic stall model did not improve the airloads of DYMORE compared to the loose coupling airloads for this critical forward flight case 9017.

Table 9: Comparing the airloads computed by DYMORE to converged loose coupling airloads for case 9017

Case	Thrust [lb]	Roll mom.[lb.ft]	Pitch mom.[lb.ft]
Targets loads	16452	379	-138
Peters model	13849	5291	-8704
Case 1	14313	4729	-6502
Case 2 (10 inflow modes)	15020	5748	-7764
Case 2 (6 inflow modes)	15240	5780	-7585
Case 2 (no inflow model)	20100	9826	-3992
Loose coupling HRLES	16493	-37	-557

This might be because Leishman-Beddoes parameters were not identified at all the airstations as function of both the Mach number and the airfoil shape. Another potential cause might be that dynamic stall is non linear phenomena that needs an accurate wake solution. Datta and Chopra [26] stated that rotor dynamic stall differs from airfoil and three dimensional wing stall due to additional excitations caused by wake induced inflow and high frequency elastic twist deformations. Hence an advanced accurate wake solution is needed to accurately predict rotor airloads during dynamic stall.

The wake model used in the current test was solved using the three-dimensional finite-state generalized dynamic wake theory [67] available in DYMORE. The increase of the number of the wake inflow modes did not enhance the predicted airloads for the same empirical parameters values. However, the three-dimensional generalized dynamic wake was found to go unstable and lacks convergence as the number of inflow modes increased as shown in tables 10-11.

Results in tables 10-11 show that both case 1 and 2 for Leishman-Beddoes semi-empirical dynamic stall model parameters gave very close results for the same number of inflow modes. It might be that using a more accurate wake along with the semi-empirical dynamic stall model may be a good alternative for the more expensive CFD method. However this was not studied in the present work, as the only available

Table 10: Comparing the airloads computed by DYMORE Leishman-Beddoes Case 1 for C9017

Case	Thrust [lb]	Roll mom.[lb.ft]	Pitch mom.[lb.ft]
Targets loads	16452	379	-138
Case 1 (no inflow model)	19812	9928	-4270
Case 1 (6 inflow modes)	1.509	5816	-7705
Case 1 (10 inflow modes)	15020	5748	-7764
Case 1 (25 inflow modes)	14430	5949	-6685
Case 1 (30 inflow modes)	13730	6295	-6741
Loose coupling HRLES	16493	-37	-557

Table 11: Comparing the airloads computed by DYMORE Leishman-Beddoes Case 2 for C9017

Case	Thrust [lb]	Roll mom.[lb.ft]	Pitch mom.[lb.ft]
Targets loads	16452	379	-138
Case 2 (no inflow model)	20100	9826	-3992
Case 2 (6 inflow modes)	15265	5774	-7564
Case 2 (10 inflow modes)	15046	5747	-7733
Case 2 (25 inflow modes)	14530	5703	-6563
Case 2 (30 inflow modes)	unstable	unstable	unstable
Loose coupling HRLES	16493	-37	-557

option for a wake model within DYMORE code is the simplified Peters et al. three-dimensional finite-state generalized dynamic wake theory [67] wake that was tested here.

2.6 Conclusions

Leishman-Beddoes semi-empirical model is a complete sophisticated aerodynamic model, while ONERA EDLIN model is very simplified dynamic stall model only. Both Leishman-Beddoes and ONERA EDLIN are semi-empirical models that depend each on a set of parameters that need to be determined, and some of these parameters depend on unsteady experimental test data. In the absence of the experimental test data, the default values of these parameters could be used for each semi-empirical aerodynamic model, but the accuracy of the results becomes questionable and the conclusions drawn based on those results lose their reliability. When compared to

ONERA EDLIN dynamic stall model, Leishman-Beddoes model relies on a larger number of parameters that need to be specified and it involves more complicated dynamic stall model. ONERA EDLIN model consists only of a second order differential equation for the circulation of each airload to model dynamic stall effect.

From the test runs studied here, both semi-empirical models seem to be sensitive for the specified values of their parameters. When these models were used to compute the airloads for a practical test run to compare their results to the loose coupling results, it seemed that their effect in enhancing the computed airloads in a comprehensive code with a simplified aerodynamics tools was not enough, and an explicit sophisticated wake model is required along with those semi-empirical dynamic stall models. In the case of the existence of a reliable wake model in the comprehensive code along with sufficient accurate unsteady experimental test data to compute the parameters of these semi-empirical dynamic stall models, it is expected that the enhancement in the aerodynamic airloads computation in the presence of such dynamic stall models would be reliable and could be comparable to the CFD computed airloads with much less computational cost.

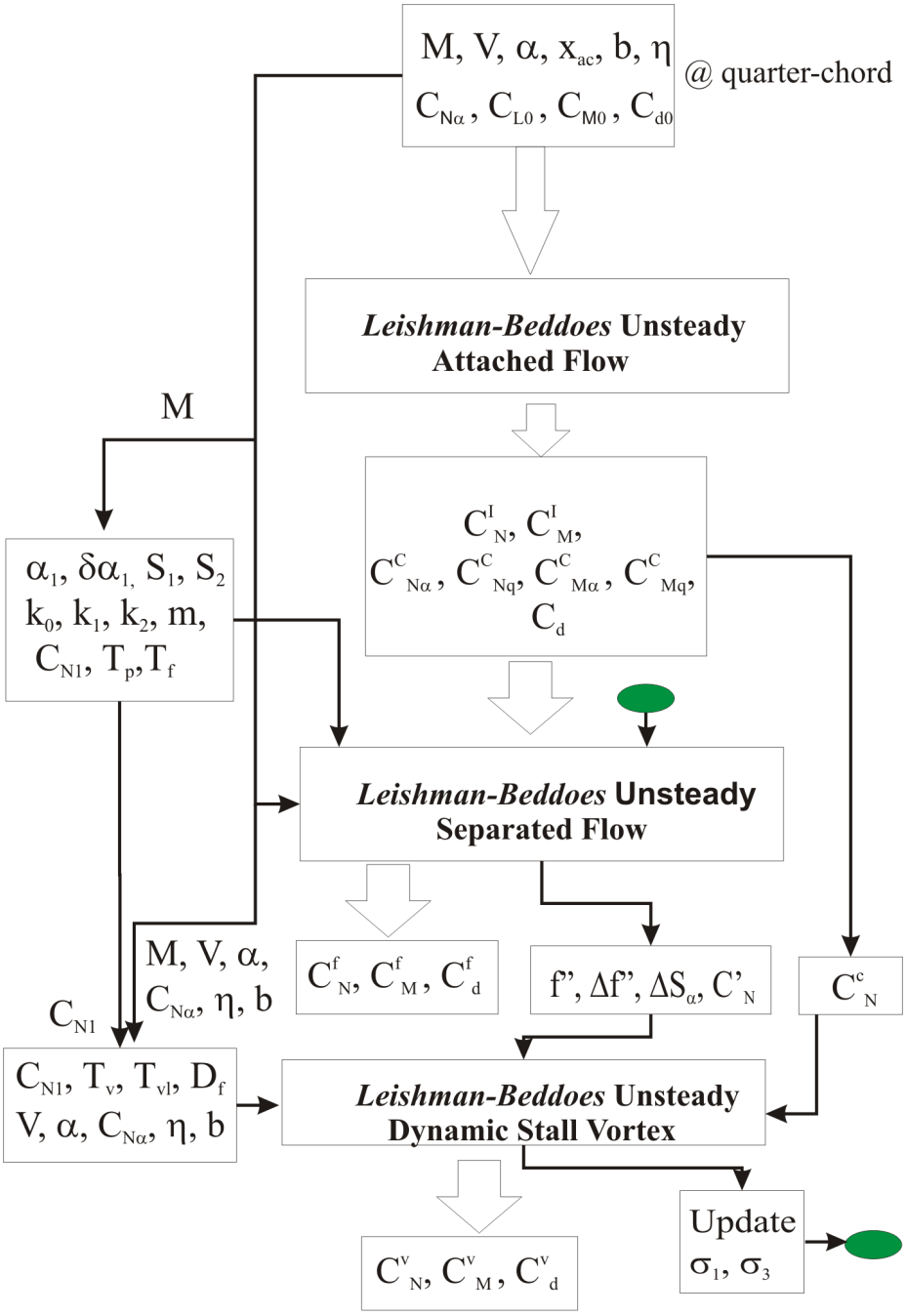

Figure 12: I/O for the complete Leishman-Beddoes Dynamic Stall Model.

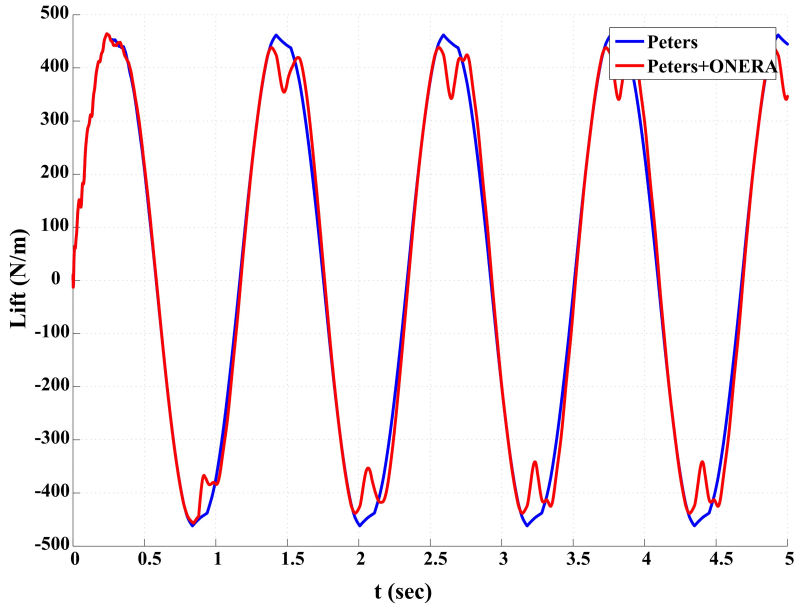

Figure 13: Computed lift per unit span by Peters+ONERA models for a light dynamic stall case.

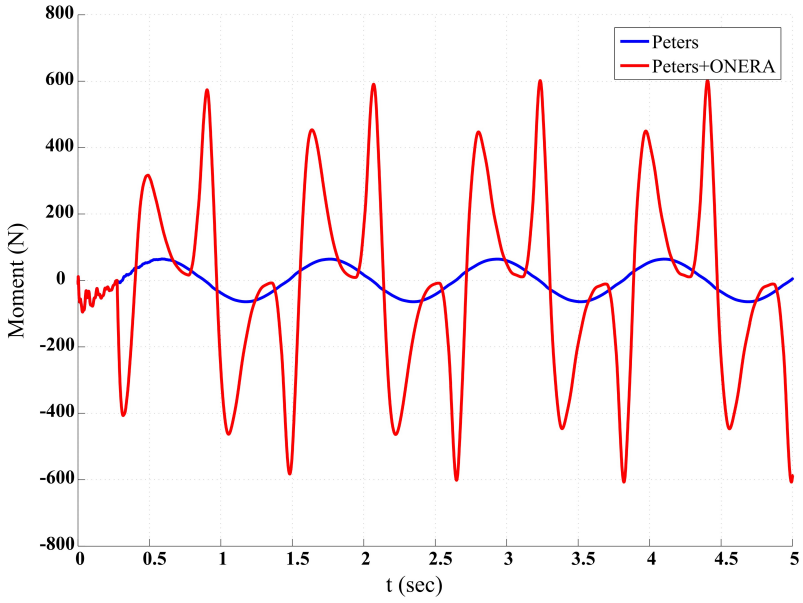

Figure 14: Computed moment per unit span by Peters+ONERA models for a light dynamic stall case.

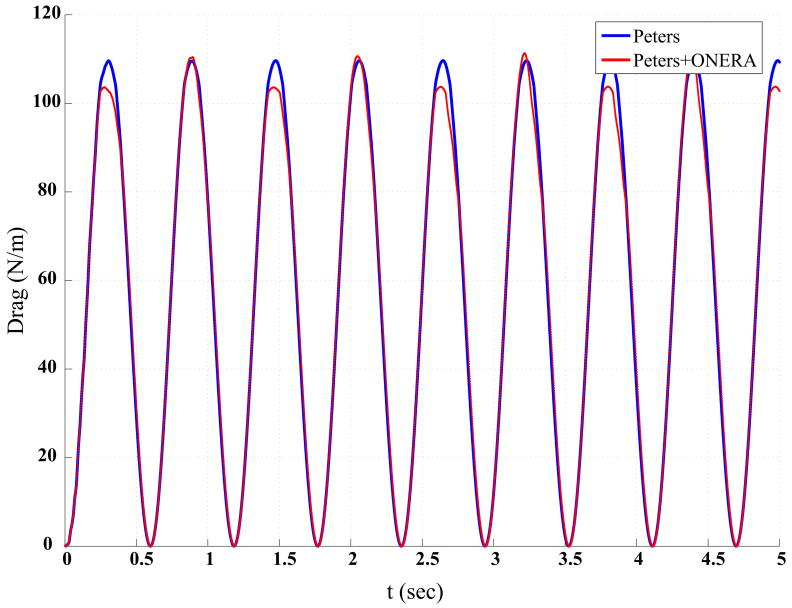
Peters
Peters+ONERA
Drag (N/m)
t (sec)
120
100
80
60
40
20
0
0
0.5
1
1.5
2
2.5
3
3.5
4
4.5
5

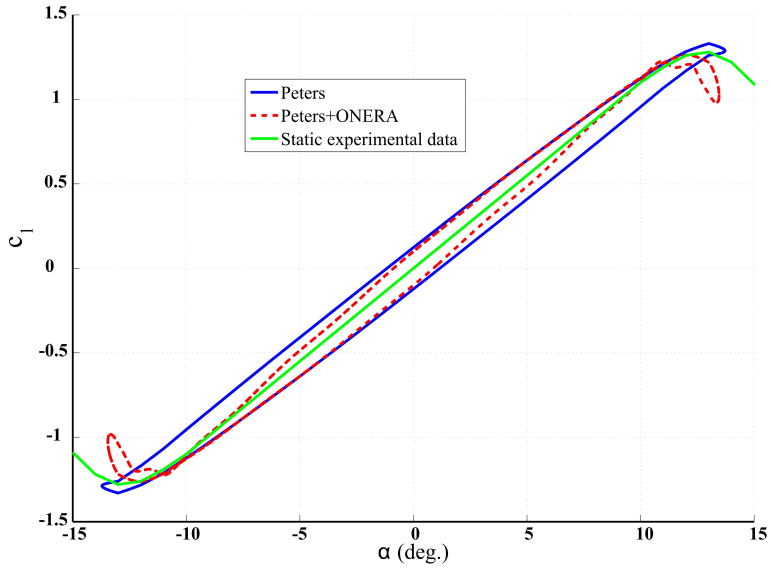

Figure 16: Computed c_l by Peters+ONERA models for a light dynamic stall case versus angle of attack.

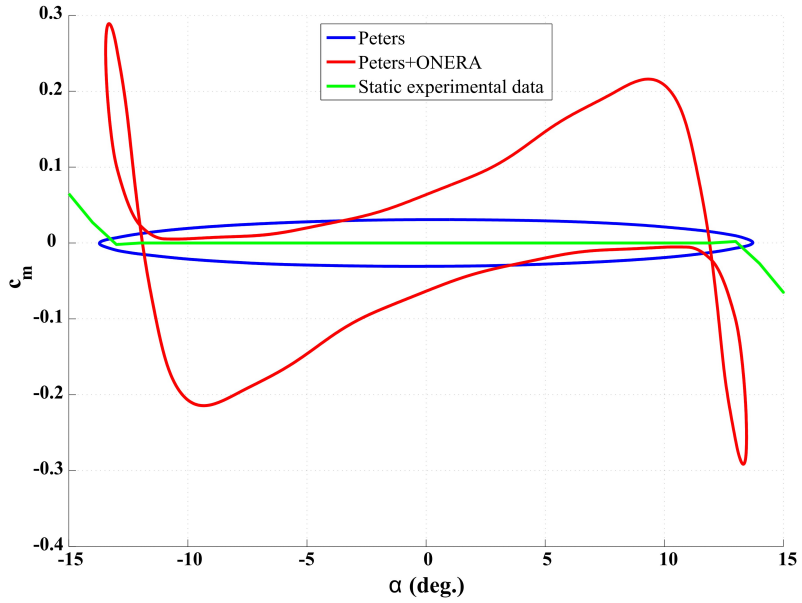

Figure 17: Computed c_m by Peters+ONERA models for a light dynamic stall case versus angle of attack.

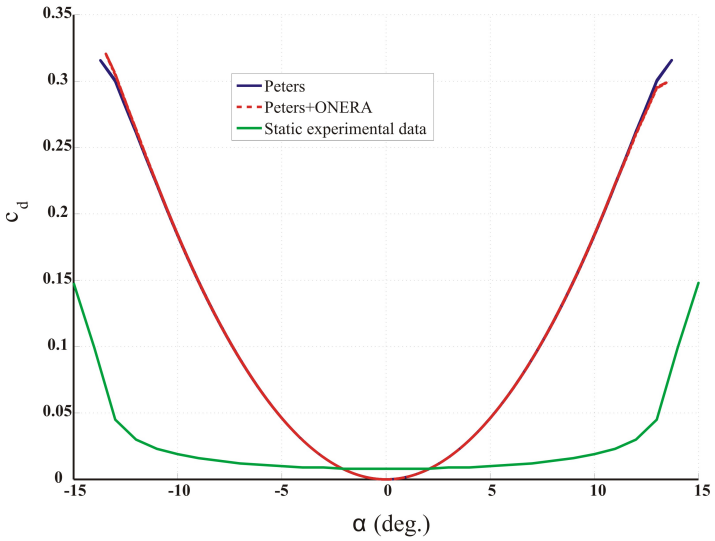

Figure 18: Computed c_d by Peters+ONERA models for a light dynamic stall case versus angle of attack.

Chapter III

QUASI-STEADY TRIMMER AND KRIGING

3.1 Introduction

A new strategy for trimming, called the quasi-steady trim algorithm is elaborated in this chapter. The purpose is to attempt to increase the rate at which the rotorcraft trimming process proceeds. It mainly depends on trying to trim in a quasi-steady manner to minimize the excitation of the light damped modes.

3.2 Quasi-Steady trimmer

The quasi-steady trimmer is a control law designed to determine the outputs $\underline{u}$ that will drive the system to a configuration where the input matches the specified target values. A set of N_i target values: $\underline{\hat{y}} = \hat{y}_1, \hat{y}_2, \ldots, \hat{y}_{N_i}$ must be defined, and N_i gains: $g_1, g_2, \ldots, g_{N_i}$, may be defined. The procedure for this proposed trim strategy as proposed by Bauchau et al. [6].

1. Identify the Jacobian J (eq. 128) and its inverse J^{-1}.

2. Obtain the initial guess for the control settings as $\underline{u}_0 = J^{-1}\underline{\hat{y}}_0$ where $\underline{\hat{y}}_0$ is the target values for the trim.

3. Run a static analysis with $\underline{u}_0$ as the control settings.

4. Run a dynamic analysis with $\underline{u}_0$ as the control settings and the configuration from the static analysis of step 3 as the initial conditions. The converged trim variables are obtained as $\underline{\hat{y}}_1$.

5. If $||\underline{\hat{y}}_k - \underline{\hat{y}}_0||(k = 1, 2, , N_i)$ is less than the expected error criteria, stop. Otherwise, update the control settings as follows:

(a) $\underline{u}_k = J^{-1}(\underline{\hat{y}}_0 - \underline{\hat{y}}_k) + \underline{u}_{k-1}$.

(b) Run a static analysis with $\underline{u}_k$ as the control settings.

(c) Run a dynamic analysis with $\underline{u}_k$ as the control settings and the configuration from the static analysis (in step b) as the initial conditions. The converged trim variables are obtained as $\underline{\hat{y}}_{k+1}$.

6. Go to step 5.

Using the above procedure, Bauchau et al. [6] performed test runs with the UH-60A model. The rotor speed for the runs was 27.02 rad/sec, and the target values for the trim were $17,944$ lb, $6,884$ lb-ft, and $-2,583$ lb.ft for the thrust, roll and pitch moments, respectively. First, an autopilot run was performed for comparison purpose and the results are shown in figures 19 and 20, which show the time history of the thrust and the change of the swash plate displacement, as an example of this run results. Clearly, it took the autopilot about 116 revolutions to obtain well converged control settings. Note that the initial guess for the control settings in the autopilot run was very good in the sense of being near the final converged control settings. With bad initial control settings, autopilot may need longer time to converge. In some cases, no convergence occurs.

The trimming procedure was next accomplished using the proposed manual quasi-steady technique. Results [6] are shown in figures 21-22 where the whole process converged in about 5 to 6 revolutions, which demonstrates the efficiency of this proposed quasi-steady trim algorithm.

However, these steps are done using a *manual process* where the static and dynamic runs in steps 3 and 4 of the procedure described above are submitted one at a time (as individual runs) for each iteration. Clearly, this process needed to be automated as an independent trimming procedure. If the simplified aerodynamic models internal to the comprehensive analysis are used, a fully automated procedure should

be put in place that leads to trim. However, to automate the proposed quasi-steady approach to trim, both static and dynamic analysis must be performed repeatedly within a single run, which is very difficult to handel in a comprehensive code specially when CFD/CSD coupling is under process. Hence, a modified version of this proposed manual process could be automated. Two time spans are defined for the two phases of the operation of the quasi-steady trimmer as following.

First, t_{ref} time span will be taken to establish the *reference configuration* of the system for the reference output values $\underline{\bar{u}}$. At the end of the reference run, the input values are denoted $\underline{\bar{y}}$. It is important to simulate the response of the system for a period that is long enough to allow the dynamics of the system to settle, *i.e.* for $\underline{\bar{y}}$ to settle to steady values.

Next, t_{adj} time span will be taken in the adjustment phase. At each time step, the control law (eq. 127) is applied to drive the input values to their targets. At the beginning of this phase, the adjustment values of the controlled variables are computed by

$$\Delta\underline{u} = J^{-1}G(\underline{\hat{y}} - \underline{y}_f) \tag{126}$$

where $\underline{y}_f$ is the present input value at the beginning of the adjustment phase time T_{iniate}, J is the Jacobian matrix defined in eq. 128, and G is the gain matrix. The gain matrix is assumed to be a diagonal matrix. The quasi-steady trimmer modifies the controls proportionally to the output error to drive the inputs to their target values. The following discrete equations are introduced to compute the control outputs at each time step

$$\underline{u}_f = \underline{u}_i + \frac{t_f - T_{iniate}}{T_{\text{adj}}}\Delta\underline{u} \tag{127}$$

where the subscripts $()_i$ and $()_f$ denote quantities computed at the initial time (denoted t_i) and final time (denoted t_f) of the time step, respectively. T_{iniate} is the beginning time of the adjustment phase, and T_{adj} is the total adjustment time. $\Delta\underline{u}$ is the total adjustment magnitude in the controller outputs defined in eq. 126. The

Jacobian matrix is defined as a derivative of the inputs with respect to the outputs

$$J = \frac{\partial \underline{y}}{\partial \underline{u}} \tag{128}$$

This matrix is, in general unknown. Hence, it is either evaluated numerically using a finite differences process or it is replaced by an approximated model that will represent the relation of the system outputs to its inputs (through system identification [8] or by using meta-models).

3.2.1 Application challenges and solutions

Application of the quasi-steady trimmer approach to periodic problems can be troublesome. In view of eq. (127), the control variables are adjusted at every time step to track the target values. This leads to periodic excitation of the controlled variables, and in turn, to periodic excitation of the input values. To overcome this problem, the quasi-steady trimmer equation should be driven by averages of the input values over one period of the system. This is readily achieved in DYMORE by using the data conditioning feature of sensors, and all sensors measurements will then be running averages instead of instantaneous measurements. This averaging could be done using an online FFT or a low bypass filter (see section 3.3). In the automated form, the quasi-steady trimmer computes the required changes in the controls at the beginning of the *adjustment phase*, but instead of applying them at a single time step after multiplying the computed values by very small gain numbers then update them in the next time step (like the autopilot), it eventually applies them through the complete *adjustment phase* using a linear time function. A lot of other time functions were tried to apply the control changes as quasi-steady as possible, but it was observed that the linear function was more efficient.

Some modifications were also tried in the main quasi-steady trimmer algorithm. By example, after computing the changes in the controls, they are applied through step functions, then keeping the controls constant for a certain amount of time to

allow the decay of the system transient responses. This procedure showed good results regarding the stability of the system, but on the other hand it was taking longer time than the autopilot to converge.

The quasi-steady trimmer in its automated form, increased the number of parameters that should be adjusted for each simulation, and they exceed the number of parameters of the autopilot, and this is a disadvantage in the proposed quasi-steady trimer, as the problem becomes harder to identify the appropriate values of these parameters that will keep the simulation stable to converge. If the input Adjustment time T_{adj} is set to equal the time step size, then the quasi-steady trimmer is reduced to the autopilot control law. Both the autopilot and the quasi-steady trimmer fail to work if the system to trim is unstable.

The behavior and convergence characteristics of both the autopilot and the quasi-steady trimmer are affected by the gain matrix $G = \text{diag}(g_i)$. The individual gains g_i should be adjusted to obtain the best convergence characteristics. High gain values may render the system unstable. Even moderate gain values can lead to instabilities because the quasi-steady trimmer does not account for system dynamics. To overcome this problem, define $e = \|\hat{\underline{y}} - \underline{y}\|/\|\hat{\underline{y}}\|$ as the relative difference between the actual and target input values. When the difference between the input and its target value becomes small, smaller then reference value $e_{\min}$, the gain is gradually decreased to zero using the following schedule [89]

$$g_s = \tanh(4e/e_{\min}) \tag{129}$$

3.2.2 Test results

The performance of the automated quasi-steady trimmer was evaluated by simulating the UH-60A helicopter in a fully automated manner. The inflow on the rotor disk was modeled using the Peters' dynamic inflow model. Figures 23-28 show the results of a typical run. The left portions of these figures show the time history of the

rotor thrust, pitching moment and rolling moment, respectively. The right portions depict the rotor collective, longitudinal, and lateral cyclic controls, respectively. For the first 12 seconds, the rotor is simulated with constant control inputs. The lift and pitching and rolling moments are stabilized to their reference values. Note the slow oscillation in the response coming from the slow time response of the wake for about 7 seconds. At time $t = 12$ seconds (*reference phase*), the quasi-steady trimmer starts to adjust the controls (*adjustment phase*). As expected, the lift converges to the target value, whereas the moments are much slower to converge.

As conclusion, when using the Jacobian approximation to model the system, both the quasi-steady trimmer algorithm and the autopilot ignore to a certain extent system nonlinearity and dynamics from both structural dynamics and aerodynamic standpoints. However, still the main problem faced by the controller is that the system to be trimmed is not completely controllable and observable. This leads to a maximum rate at which the controls could be changed, after which the lightly damped modes will be excited and will lead the system unstable. To avoid these spurious dynamics and unsteady aerodynamic effects, it is necessary to limit the rate of change of the control variables per time step. Hence, if $R_{\max}$ is defined, the following condition is imposed

$$\|\underline{u}_f - \underline{u}_i\| \leq R_{\max} \tag{130}$$

A great care should be taken in specifying the input value of $R_{\max}$ as the adjustment time of the adjustment phase T_{adj} decreases, since by definition, it is the allowed maximum rate of change the controlled variables per time step. An appropriate value of $R_{\max}$ is $0.1\Delta t$, where Δt is the time step size.

The proposed solution to achieve faster trim is to find a very good initial guesses of the controls for certain target loads and certain flight condition. If good initial guesses are provided, any reasonable control law will reach the trim state rapidly, as long as the sign of the Jacobian is correct. To provide this good initial guess, the

Ordinary Kriging is going to be used (see section 3.4).

3.3 Filter

3.3.1 Introduction

As mentioned previously in section 3.2.1, filters could be used to provide airloads filtered values to the controller. Filters are typically designed to eliminate or attenuate the amplitude of a signal in certain frequency ranges. Filters can be low-pass, band-pass, high-pass, or band reject filters. Among the well-known filters are the Butterworth, Bessel, Chebyshev Types I and II, and elliptic filters [46]. Let $x(t)$ be a time dependent signal and $\hat{x}(t)$ be the signal resulting from the application of the filter. It is convenient to characterize filters in Laplace domain as

$$\hat{x}(s) = H(s)x(s) \tag{131}$$

where $x(s)$ and $\hat{x}(s)$ are the Laplace transforms of $x(t)$ and $\hat{x}(t)$, respectively, s is the Laplace variable, and $H(s)$ is the transfer function that characterizes the filter. This transfer function is typically given for a unit *cutoff frequency* ($\Omega_c = 1$ rad/sec) as a rational function of $\bar{s} = s/\Omega_c$

$$H(\bar{s}) = \frac{\sum_{k=0}^{M} b_k \bar{s}^k}{1 + \sum_{k=0}^{N} a_k \bar{s}^k} \tag{132}$$

3.3.2 Butterworth Low-pass Filter

Butterworth low-pass filters are characterized by the property that the magnitude characteristics is maximally flat at the origin of the s plane. This means that as many derivatives of the magnitude response as possible are zero at the origin. Its poles occur at equally spaced points on the unit circle in the s plane. The transfer function of the normalized Butterworth filter can then be written in terms of its poles

as

$$H(\bar{s}) = \frac{1}{\prod_{k=1}^{N}(\bar{s} - \bar{s}_k)} \tag{133}$$

where N is the filter order, and the poles are

$$\bar{s}_k = \exp\left[\frac{i\pi}{2}\left(1 + \frac{2k-1}{N}\right)\right], \quad k = 1, 2, \ldots, N \tag{134}$$

and $i = \sqrt{-1}$. Expanding the denominator of eq. (133), the Butterworth transfer function becomes

$$H(\bar{s}) = \frac{1}{\bar{s}^N + a_{N-1}\bar{s}^{N-1} + \ldots + a_1\bar{s} + 1} \tag{135}$$

The squared-magnitude response of a normalized Butterworth filter is

$$|H(\bar{\Omega})|^2 = [H(\bar{s})H(-\bar{s})]\,|_{\bar{s}=i\bar{\Omega}} = \frac{1}{1 + (\bar{\Omega}^2)^N} \tag{136}$$

where $\bar{\Omega} = \Omega/\Omega_c$ the normalized frequency. From eqs. (136) and (134), the characteristics of Butterworth low-pass filters are as follows: they are all-poles designs (*i.e.* their zeros are at $s = \infty$), and at $\bar{\Omega} = 1$, their magnitude response is down 3 dB at the cutoff frequency. The filter order N completely specifies the filter. The filter order required to obtain a magnitude of $1/A$ at $\bar{\Omega} = \bar{\Omega}_t$ can be obtained from

$$N = \frac{\log_{10}(A^2 - 1)}{2\log_{10}(\bar{\Omega}_t)} \tag{137}$$

The magnitude (gain) and phase of a normalized Butterworth low-pass filter are defined by

$$G(\bar{\Omega}) = |H(i\bar{\Omega})| \tag{138}$$

and

$$\phi(\bar{\Omega}) = \arctan\left[\frac{\Im[H(i\bar{\Omega})]}{\Re[H(i\bar{\Omega})]}\right] \tag{139}$$

Figure 29 shows the variation of the magnitude of the frequency response of a normalized low-pass Butterworth filter with its order, while figure 30 shows the phase of a 2^{nd} order normalized Butterworth filter.

3.3.2.1 Butterworth filter in state space form

Taking the inverse Laplace transform of eq. (133), the following differential equation of the Butterworth filters is obtained

$$\frac{\mathrm{d}^N \hat{x}(\tau)}{\mathrm{d}\tau^N} + a_{N-1}\frac{\mathrm{d}^{N-1}\hat{x}(\tau)}{\mathrm{d}\tau^{N-1}} + \ldots + a_1\frac{\mathrm{d}\hat{x}(\tau)}{\mathrm{d}\tau} + \hat{x}(\tau) = x(\tau) \tag{140}$$

where $\tau = \Omega_c t$ is the non-dimensional time. This N^{th} order linear differential equation can be transformed into a state space in the form of

$$\dot{\underline{v}} = A\underline{v} + Bx(\tau) \tag{141}$$

where $\underline{v}_{(N)}$ is the state vector

$$\underline{v}^T(\tau) = \lfloor \hat{x}(\tau), \frac{\mathrm{d}\hat{x}(\tau)}{\mathrm{d}\tau}, \ldots, \frac{\mathrm{d}^{N-1}\hat{x}(\tau)}{\mathrm{d}\tau^{N-1}} \rfloor \tag{142}$$

For the Butterworth filters

$$A_{(N\times N)} = \begin{bmatrix} 0 & 1 & 0 & \ldots & 0 \\ 0 & 0 & 1 & 0 & \ldots \\ \vdots & \vdots & \vdots & \vdots & \vdots \\ -1 & -a_1 & \ldots & -a_{N-2} & -a_{N-1} \end{bmatrix}, \quad B_{(N)} = \begin{bmatrix} 0 \\ \vdots \\ 1 \end{bmatrix} \tag{143}$$

Using the trapezoidal rule, this linear ODE system could be integrated to obtain

$$\underline{v}_f = K_1^{-1}\left[K_2\underline{v}_i + \Delta\tau\frac{x(\tau_f) + x(\tau_i)}{2}B\right] \tag{144}$$

where $\Delta\tau = \Omega_c\Delta t$ is the normalized time step size. 'i' and 'f' denote the initial and end of the time step, respectively, and K_1 and K_2 matrices are defined by

$$K_1 = \left[I - \frac{\Delta\tau}{2}A\right], \quad K_2 = \left[I + \frac{\Delta\tau}{2}A\right] \tag{145}$$

3.3.3 Test Example

Consider a discrete signal representing the total lift of a four bladed rotor in periodic steady forward flight. This total lift is shown in figure 31. Next, a Butterworth low-pass 2^{nd} order filter with $\Omega_c = 1.93$ rad/sec is applied on this signal. Figure 32 shows the resultant filtered signal.

3.3.4 Comparing the Butterworth filter to the on-line FFT

A random signal is created. Both on-line FFT [5] and Butterworth filter (with different orders and cutoff frequencies) are applied to it separately.

As shown in figure 33, the lag induced in the filtered signal increased by increasing the cutoff frequency and the order of the Butterworth filter, while the on-line FFT did not introduce such noticeable lag in averaging the signal. Since introducing lag has a destabilizing effect, the on-line FFT is superior to Butterworth filter for averaging the signals involved in rotor trimming problems. It is important to note that mainly on-line FFT requires the foreknowledge of the frequencies content in a particular signal, which is suitable for rotorcraft airloads in periodic steady forward flight, but if the original signal contains noise of unknown frequencies, a question rises about the accuracy of the on-line FFT averaging procedure.

3.4 Kriging Meta-Model

3.4.1 Introduction

A meta-model is an approximation of the I/O function that is implied by the underlying simulation model which could be either deterministic or random (stochastic). A deterministic simulation is a simulation which gives same output for the same input. For deterministic computer analysis, there is no random error, and thus the meta-model should reproduce each experimental point exactly and interpolate between them. That is the meta-modal predictions at the locations of the training data points should be the same as the actual values of the training data points [22, 62].

The linear regression methods fit the data points to linear or nonlinear curve functions by minimizing the distances between these sample points and the curve to fit (the error). In the case of the nonlinear regression techniques like Artificial Neural Networks (ANN), the sample points are to be fitted to a complicated curve function with no easy way to predetermine it. That is in the case of the ANN, the curve

function is determined implicitly and it is not through a set of unknown coefficients as in the case of linear regression techniques.

In the case of Gaussian Process (GP), there is not anymore a curve to fit. Instead GP uses the information in the data set to create a statistical prediction or estimate by incorporating Bayesian regression. To understand this concept of GP, figure 3.4.1 shows a typical case, a set of sampled data points at different values of the input. If those sample points are to be fit, there are different curves that could be used, which means that at each input value the are different values of the output based on the curve used to fit the data. The output could be viewed as a random variable, assumed to be of Gaussian distribution, with a mean value (the most likely to occur) and a variance. Gaussian process provides this mean value, and the variance (i.e. how good is this prediction).

As a conclusion, not all the predictions obtained by GP will have the same measure of goodness, as shown in figure 3.4.1. The closer the point to one of the sampled points, the smaller the variance of the prediction will be, till the variance reaches zero at a known sampled point [24].

The kriging as a meta-modeling technique is similar to GP in the local component. However, it does not typically make use of the Bayesian step the way GP does [25, 59]. Kriging provides flexible means to construct meta-models that accurately approximate highly nonlinear behavior. Kriging meta-model is usually used for predictions, sensitivity analysis, and optimization [44].

Kriging also offers more accuracy than the polynomial regression methods, but at the cost of a difficult setup, while the later trades some accuracy for ease of use [62]. Several authors [32,38] have shown that in side by side comparisons of kriging and response surface models for aerospace applications, neither one consistently outperforms the other. However, kriging also lends itself nicely to sequential experimentation, in which experimental data is collected as needed in an iterative manner, which is very

useful for expensive experiments. Several references [23, 43] demonstrated the use of an estimation of the prediction error as a basis for sequential sampling, by directing the new samples to regions characterized by larger errors [62]. Moreover, kriging models gained large popularity for approximating the mapping process of a deterministic computer program, due to its high capability to model complex response functions [59].

The first goal in this study is to use kriging to predict good initial controls corresponding to specified loads targets. Thus dramatically reducing the computation effort required for the trimming procedure. Then the second goal is to use the kriging meta-model to compute the Jacobian matrix as opposed to system identification.

In the mathematical study next, a univariate kriging will be considered, that is a kriging applied to a single output simulation model, and this model could then be applied for every output of multiple outputs simulations.

3.4.2 Ordinary Kriging

Ordinary kriging is the simplest type of kriging, and it is quite successful in deterministic simulation. Ordinary kriging assumes the following model for the prediction

$$y(\mathbf{x}) = \mu + \delta(\mathbf{x}) \tag{146}$$

where μ is the average of the simulation output over the whole experimental area (i.e. over the whole domain of admissible scenarios), and $\delta(\mathbf{x})$ represents the deviation of the simulation output y from its mean value μ, that forms a stationary covariance process (i.e. a random process with zero mean, constant variance, and covariance that is giving by eq. (147)).

$$Cov(\mathbf{x}_1, \mathbf{x}_2) = \sigma^2 R(\mathbf{x}_1, \mathbf{x}_2) \tag{147}$$

where σ^2 is the process variance, and $R(\mathbf{x}_1, \mathbf{x}_2)$ is the correlation matrix calculated by spatial correlation function eq. (152).

Now assuming there are n data points of the simulation results that form the simulation experiment, obtained by running the simulation for n different combinations of its k inputs, then $\mathbf{x} = (x_{ij})$ is the design matrix for the experiment, with $i = 1, \ldots, n$ and $j = 1, \ldots, k$. An example of the design of experiment for the case of a rotorcraft simulation aeroelastic code is shown in figure 36.

Ordinary kriging, will be called henceforth kriging, uses the following linear predictor

$$\hat{y}(\mathbf{x}) = \lambda^T(\mathbf{x})\mathbf{Y} \tag{148}$$

where λ is the vector of weights which decrease with the distance between the input $\mathbf{x}$ at which the output is to be predicted, and the experiment n inputs combinations data points used to compute the simulated outputs $\mathbf{Y}$. To calculate the optimal values of these weights, kriging selects the Best Linear Unbiased Predictor (BLUP), which minimizes the Mean Squared Error (MSE) of the prediction $\hat{y}$, and preserves the predictor unbiased. The mathematical form of these two constraints are formulated in eqs. (149) and (150), respectively.

$$\min_{\lambda} MSE[\lambda^T(\mathbf{x})\mathbf{Y}] = \min_{\lambda}[E[\lambda^T(\mathbf{x})\mathbf{Y} - y(\mathbf{x})]^2] \tag{149}$$

$$E[\lambda^T(\mathbf{x})\mathbf{Y}] = E[y(\mathbf{x})] \tag{150}$$

Finally, using the optimum weights, the BLUP prediction could be giving by

$$\hat{y}(\mathbf{x}) = \mu + \mathbf{r}(\mathbf{x})^T R^{-1}(\mathbf{Y} - \mu\mathbf{1}) \tag{151}$$

where $\mathbf{x}$ is the input at which the output is to be predicted, and $\mathbf{r}(\mathbf{x})$ is the n-dimensional correlation vector between the n experiment inputs combinations data points used to compute the simulated outputs $\mathbf{Y}$ and the location at which the output $\hat{y}$ is to be predicted. This vector is also calculated by spatial correlation function equation (152).

The commonly used correlation function in kriging is an exponential correlation function that is function of the magnitude of the distance between the two points data (since stationary covariance process eq. (146)) and that infinitely differentiable very smooth function [25]

$$\rho(\mathbf{x}_i, \mathbf{x}_j) = exp[-\frac{1}{2}\sum_{l=1}^{k} \theta_l h_{ij}^l] \tag{152}$$

where $\mathbf{\Theta} = (\theta_1, \ldots, \theta_k)$ are the free parameters for the correlation function for a k inputs coordinates system, which act as a measure of the length scale of variation in each of the k inputs directions. $h_{ij}^l = |\mathbf{x}_i^l - \mathbf{x}_j^l|$ is the magnitude of the distance between pair i and j of the inputs training sample points in direction l. The values of these free parameters are obtained through an optimization technique is studied, implemented and tested in 3.4.3.

The overall procedure for the kriging meta-modeling for rotorcraft simulations could be summarized in the next few steps

1. Design of Experiment

   (a) Create a set of n training data spanning the parameter range of interest of the rotorcraft flight envelope.

   (b) Let $\underline{\Theta}$ be the control inputs and $\underline{L}$ the corresponding rotor thrust and moments. No trimming is required to generate the data (this provides important computational savings).

   (c) Using the obtained trained data, evaluate the free parameters values through the optimization technique using the position of the target loads.

2. Use kriging meta-model with the optimized free parameters to estimate the control settings corresponding to the target loads for the specified flight case.

The use of this kriging meta-modeling as sensitivity analysis tool to approximate the system Jacobian will be investigated next.

3.4.3 Kriging Free Parameters

The best guesses for the free parameters of kriging model for a certain training data sample points are those that will maximize the Maximum Likelihood Estimates (153) and that will give the best estimates (MLE method) [87]. However this method is based on assuming that the observed data are behaving as a Gaussian process, which is a very restrictive constraint, and when this constraint is not applicable, then the Cross Validation method (CV) results in better estimates of the model parameters then MLE, with the disadvantages that CV is significantly more computationally expensive than MLE and does not also result in an estimate of the variance, which is a straight forward result of the MLE formulation [59]

$$l[\mathbf{\Theta}|\mathbf{Y}] = -\frac{n}{2}\ln[2\pi\sigma^2] - \frac{n}{2}\ln[|R|] - \frac{1}{2\sigma^2}(\mathbf{Y}-\mu\mathbf{1})^T R^{-1}(\mathbf{Y}-\mu\mathbf{1}) \tag{153}$$

where σ^2 is the process variance. The MLE technique was implemented in DYMORE. Both steepest descent and Polak-Robiere (Gradient method) methods were tested to minimize the negative of the log likelihood function. The steepest descent method was used in the obtained results explored in this study, and Polak-Robiere method was added when difficulties were encountered in the convergence of the optimization of the MLE. However as it will be explained next, it turns out that this problem was not due to the optimizer efficiency itself, but it is a problem dependent instead. Polak-Robiere method's main attraction is the simple formula for updating the direction vector, requiring only the computation of the first partial derivatives. This conceptually decreases the computation effort associated with computing the second partial derivatives, which increases with the increase of the number of independent variables. Also this method is slightly more complicated than the steepest descent method, but converges faster. Some difficulties in the convergence were observed, and

hence it was also tested to restart new loop of the optimizer iterations and initializing the free parameters with those of the last iteration in the previous loop, that is restarting the optimizer loop with updated initial values of the free parameters. It was also tested to compute the maximum log likelihood function at random grid points of the free parameters, and the initial guess of the first optimizer loop is the free parameter set corresponding to the maximum log likelihood function.

The optimization of the kriging free parameters was next implemented and evaluated in DYMORE code.

3.4.4 Implementation and Testing

For the application of kriging in this effort, there are three dependent variables which are the thrust, and the roll and pitch moments. There are three independent variables which are the three control angles: the collective, and the longitudinal and lateral cyclics. The problem arises from the fact that there is only one cost function to maximize to compute the free parameters, while there are three dependent variables. That is, there are different sets of free parameters that will best fit each of the dependent kriging meta-model, i.e. the kriging meta-model of the thrust as a function of the three controls, the kriging meta-model of the roll moment as a function of the three controls, and finally that for the pitch moment as a function of the three controls. To obtain a target value for the thrust, the thrust-controls meta-model will give an estimate of controls, followed by target trim to the roll moment, which requires another set of control estimates, and so on, which creates the problem. The goal is to obtain a unique set of controls that are the best estimates, corresponding to the three loads concurrently, and not a different set of controls for each load.

To correct this problem, instead of having the meta-model be based on the airloads functions of the controls, the inverse relation is going to be modeled, and hence at the same target loads there will be a corresponding unique control estimates.

The MLE method depends on an unconstrained optimization problem, which is usually solved through a numerical iteration algorithm, like the method of steepest descent or Newton's method. In such methods, the iteration loop initialization begins from a set of initial guess for those free parameters. It was observed that it was difficult to determine a unique set of the initial guess of the free parameters, and that the cost function can contain local minima that depend on the initial guess. At the beginning the optimization is performed on the free parameters of the collective as function of the thrust and the two moments, then the same optimized set of free parameters was used for the two cyclic controls meta-models as functions of the loads. The obtained results are analyzed next.

Figures 37-39 summarize the results obtained from the kriging meta-model where the kriging free parameters were obtained by optimization for the collective-airloads relations and the data sample points consist of the 9 points obtained by CFD/CSD loose coupling simulations of the UH-60A rotor case 8534. To test the kriging meta-model, first the values of the independent variables for the 9 samples points were passed to the model, and the model estimated values for the dependent variables were compared to the data samples points used to train the model. As shown in figures 37-39, the estimated values are almost equal to the trained values (labeled *kriging meta-model* and *sample points*, respectively). Then, a range of random values for the independent variables were generated and passed to the kriging meta-model, to test the model interpolation accuracy. The obtained interpolated functions are plotted as continuous lines in these three figures (labeled *test model*).

In these 2-D plots of the 3-D functions, the interpolated functions could detect the overall behavior of the variations of the dependent variables as functions of the independent variables, but the predictions still have large variances. This is due to that this test case includes only 9 sample points to get the variation of three variables as functions of three independent variables. However, the main feature

of the variations could be still detected by the meta-models, which means that the Jacobian computed based on those meta-models could be accurate enough to get a converged trim solution. On the other hand, using this model with the optimized free parameters to predict initial controls estimations corresponding to the target loads, were very close to those of the 5^{th} iteration loose coupling results, as shown in table 13, and the different cases are explained in table 12.

Table 12: Different test cases definition

Case A	9 points DYMORE/OVERFLOW LC, single optimization
Case B	9 points DYMORE/OVERFLOW LC, general optimization
Case C	5^{th} iteration DYMORE/OVERFLOW LC
Case D	9 points DYMORE, single optimization
Case E	9 points DYMORE, general optimization
Case F	16 points DYMORE, single optimization
Case G	16 points DYMORE, general optimization
Case H	DYMORE trimmed controls

LC refers to loose coupling runs, *single optimization* refers to optimization of the free parameters for one of the dependent variables and using the same free parameters to the other two dependent variables meta-models; and *general optimization* is the optimization of the free parameters for every dependent variable meta-model.

Table 13: Comparing the controls estimated from kriging to 5^{th} iteration of loose coupling for Case 8534

Case	Collective [rad]	Cyclic1 [rad]	Cyclic2 [rad]	Estimation S.D.
A	0.228295	0.0423120	-0.139071	0.451
B	0.228369	0.00423925	-0.139435	0.446, 0.394, 0.411
C	0.230615	0.0428699	-0.14034	–
D	0.232475	0.0482541	-0.146125	0.811
E	0.232414	0.0482736	-0.146489	0.801, 0.781, 0.788
F	0.232997	0.0484298	-0.147962	0.59
G	0.232997	0.0484417	-0.148384	0.59,0.56,0.56
H	0.238321	0.0496658	-0.154414	–

Notice that the 5^{th} iteration loose coupling converged loads were not exactly equal to the target loads as shown in table 14. When beginning a new loose coupling run

Table 14: Comparing the loads of different cases to 5^{th} iteration of loose coupling for Case 8534

Case	Thrust [lb]	Roll mom.[lb.ft]	Pitch mom.[lb.ft]
Targets loads	16602	6042	-4169
DYMORE trimmed loads	16601.9	6032.07	-4178.8
LC converged loads	16609	6211	-2253
DYMORE Loads Case A	16912	5929.22	-3329.79
DYMORE Loads Case C	16842.4	5982.55	-3667.24

with iteration 0 control settings corresponding to the kriging controls initial estimates, the converged loads of iteration 0 loose coupling were more deviated from the target loads than the converged loads corresponding to loose coupling iteration 0 with traditional initial control settings. However the loose coupling run beginning from the kriging controls estimates as the initial settings, did converge faster to the target loads than the original run as shown in table 15, where *iter* is used as abbreviation for *iteration*.

Table 15: Comparing converged loads for CSD alone and CFD/CSD loose coupling at the kriging estimated controls

Case	Thrust [lb]	Roll mom.[lb.ft]	Pitch mom.[lb.ft]
Targets loads	16602	6042	-4169
iter 0 Traditional Start	16380	-3311	-6050
iter 5 Traditional Start	16609	6211	-2253
iter 0 Kriging Start	16050	21140	2857
iter 3 Kriging Start	16630	7495	-4235

This may mainly be due to that iteration 0 is done with the absence of the delta airloads, and that those delta airloads corresponding to the iteration 0 run with kriging estimates as initial controls, so they are more accurate than those corresponding to iteration 0 run with the traditional start, and hence the first case converged faster. Notice in this test case, the data sample points for the CFD/CSD were created around the converged loose coupling controls.

Another test was done, where the sample points were created using the simplified aerodynamic module in DYMORE (CSD code alone, low cost runs). A set of controls

points were created, around the converged controls of the CFD/CSD loose coupling run, which are not the converged controls for the CSD stand alone code. The kriging optimized free parameters and the estimated control settings are shown is table 13.

The variance of the estimates is large for the CFD/CSD and the CSD stand alone code. Taking into account that the free parameters of the kriging meta-models were optimized based on the given observed data in both cases, this might indicates that this high variance in both cases are mainly due to the small number of sample points used in training kriging meta-models in both cases. To test that, more samples points were added to the CSD side to see the effect of increasing the number of the sample points on the variance of the meta-models estimations. As shown in table 13, the variance of the estimations of the kriging meta-model based on 16 data sample points is smaller than that of the estimation calculated based on 9 data sample points as expected. Using the controls estimate based on 16 data sample points to run the CSD code resulted in airloads closer to the target airloads than the CSD run airloads with controls estimate based on 9 samples points only. In addition, the way the data points were created could also have an effect on the accuracy of the estimation. However this can not be confirmed from the runs carried in this test. As a conclusion, the accuracy of the estimation carried out using kriging meta-model depends on the location of the independent variables at which the estimation is to be calculated, with respect to the data sample points. As expected, adding more points to the data sample increases the accuracy of the estimation. Also creating the data sample points around the known converged controls solution results in good accuracy level for the prediction based on smaller number of data sample points.

Driving the optimization of the free parameters for the three controls meta-models resulted in more computation costs, and better initial guess of the controls and estimates.

As was mentioned at the beginning of this section, it was found that when changing

the initial guess of the free parameters that are passed to the optimizer loop, the obtained estimate values and variances vary, and sometimes it is not easy to get a converged set of free parameters using the MLE method.

In investigating the source, potential causes, and proposed solutions of this problem, it was found that a number of references approached the problem, and proposed quite different explanations and solutions.

Reference [59] suggested that this might indicate that the constraint of the MLE method used to get the kriging best parameters is questionable, that is the observed data of the model do not really behave as a Gaussian process.

Reference [90] showed that sometimes the likelihood profile function has a long very flat ridge with a number of local maxima of almost identical height for the Gaussian correlation function is used, which is eventually what is being observed.

Reference [58] explained some difficulties with the method of maximum likelihood estimation for the spatial linear model, and that even for small samples, even with a regular covariance scheme like the exponential function used here, the likelihood can be multimodel. One of the solutions to such problem, is doing several optimization cycles, and then takes the best one among them. According to reference [59], it seems that the free parameters magnitude is very important and can vary widely, while their exact value is not so important, and hence redoing the optimization few times with different initial values for the free parameters, which are different with large steps, could help in solving this problem. However, this still did not explain the cause of the problem observed and a real solid solution.

Finally, it was found that reference [77] addressed the exact problem faced here and that the computed cost multi-variants function calculated based on a small number of sample points carried out using a costly deterministic computer program has a lot of difficulty in getting its minimum value. Reference [77] studied this problem in deep, and as a result, they showed that a very good solution to get around it was the

use of a penalized likelihood function instead of the profile likelihood. This results in more complicated computational effort and cost but solves the problem that was faced in the current study, caused by the small number of sample points used in the kriging meta-model training. Such a problem is faced when the sample points are drawn from costly computer program runs.

To study reference [77] suggestion, first a simple example was re-run using the implemented MLE in DYMORE. This example is a simply *sin* function, $y = sin(x)$. First a sample of 6 points was used, $x = 0, 2, 4...10$. Reference [77] showed that the optimized free parameter was found to be 3, using both the MLE method and the REML method (REML is also called *Residual* or *Modified* Maximum Likelihood). The prediction based on the Gaussian kriging model shows that the prediction becomes very erratic when x is not equal to the sample data, as shown in figure 40, that was reproduced using the implemented kriging meta-model in DYMORE with a prescribed free parameter equal to 3. When DYMORE was run to detect the optimized free parameter for this data set, a different value of the free parameter was obtained, that is equal to almost 1.05 when the data table was not normalized, and equal to 30 when the independent variable values in the training data table was normalized in the range $[0, 1]$. The corresponding predictions of these three meta-models are compared to the exact *sin* function in figure 40. It is to note that the best meta-model was the one with the free parameter set to the value obtained using the implemented MLE in DYMORE, with normalizing the independent variable values in the data table. However, the profile function has a very large flat region along which the variance increases. To resolve this problem, and to stop the optimizer iterations before reaching this flat region, the tolerance constraint put on the Euclidian norm of the profile function first partial derivatives was set to 1% of the normalized maximum independent variable value in the training data, i.e. 0.01 in the studied case. This resulted in reaching a near-optimum optimized free parameters values with the smallest possible

kriging meta-model variance. This modification that was added, along with normalizing the independent data variables values, was shown to solve the problem of the flat region part of the profile function in this simple example, of one independent variable model. The same procedure is extended to the case of multi-independent variables meta-models.

3.4.5 CFD/CSD Loose coupling beginning from kriging controls estimates

Using the 9 sample points of the CFD/CSD loose coupling runs for the UH-60A high speed case 8534, a kriging meta-model was constructed and the estimated controls corresponding to the target loads were computed. A loose coupling run was done with initial control settings equal to the kriging control estimates. The converged airloads are shown in figure 41. It is clear that the CFD/CSD loosely coupled simulation can be trimmed more efficiently and it has been found to save typically $1-3$ coupling iterations compared to simulations that apply controls computed by the standard trim process.

3.4.6 CFD/CSD Trimming under Tight coupling

To trim under tight coupling, an efficient way is needed to determine the trim matrix, other then the system identification, that mainly depends on perturbations of the system for every control, requiring extra revolutions of the expensive simulation, just to compute the trim matrix. The tight coupling was performed through the load/motion interfaces added to both OVERFLOW and DYMORE codes, as explained in chapter 4. Using the 9 points CFD/CSD loose coupling runs studied in the previous section, a kriging meta-model was obtained with optimized free parameters for the CFD/CSD model of the UH-60A for case 8534. This meta-model was used to compute the Jacobian matrix required for the trimming of the model under tight coupling, hence replacing the lengthy and expensive system identification technique

in providing a reliable Jacobian matrix. The quasi-steady trimmer was used in this test run.

Using the kriging meta-model, the trim matrix is evaluated like in system identification technique, but instead of the need to perturb the system itself, kriging meta-model of the system is used to predict the approximate response of the system to the required perturbation numerically.

The thrust from this tightly coupled simulation using continuous trim via kriging for the UH-60A high-speed flight test case (case 8534) is provided in figure 42. The first revolution applies fixed initial controls so that the CFD transients can be resolved. Those initial controls were estimated using the kriging meta-model. During the trimming process, changes in controls are provided at every time step based on the latest performance estimates, and the trim matrix is updated every fifteen degrees using the kriging meta-model. A trimmed solution is reached for the thrust after approximately three tightly coupled revolutions, with trimmed moments achieved shortly thereafter, and the complete airloads convergence is shown in figure 43.

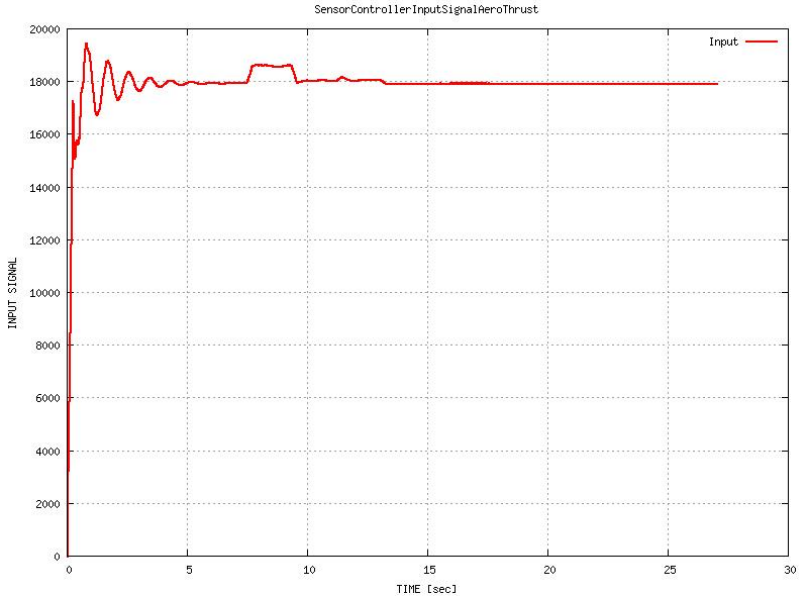

Figure 19: Time history of the thrust from autopilot run.

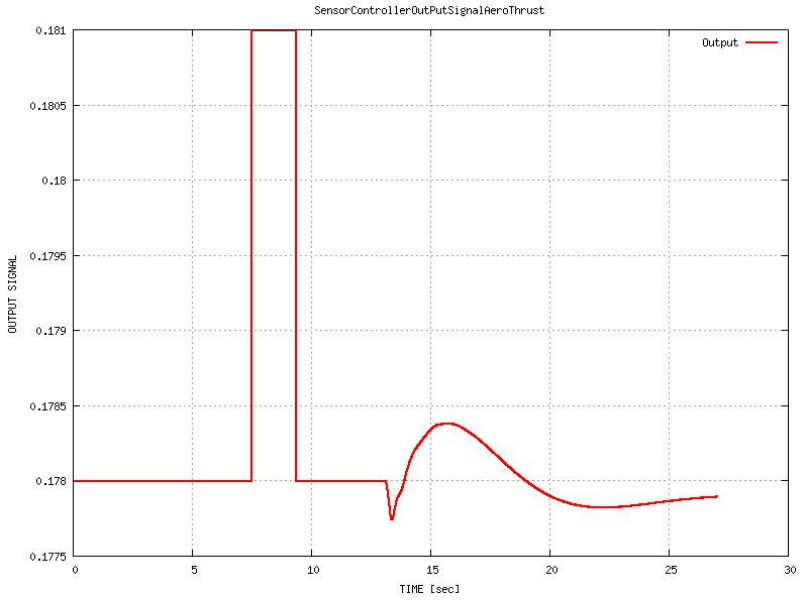

Figure 20: Displacement change of swash plate from autopilot run.

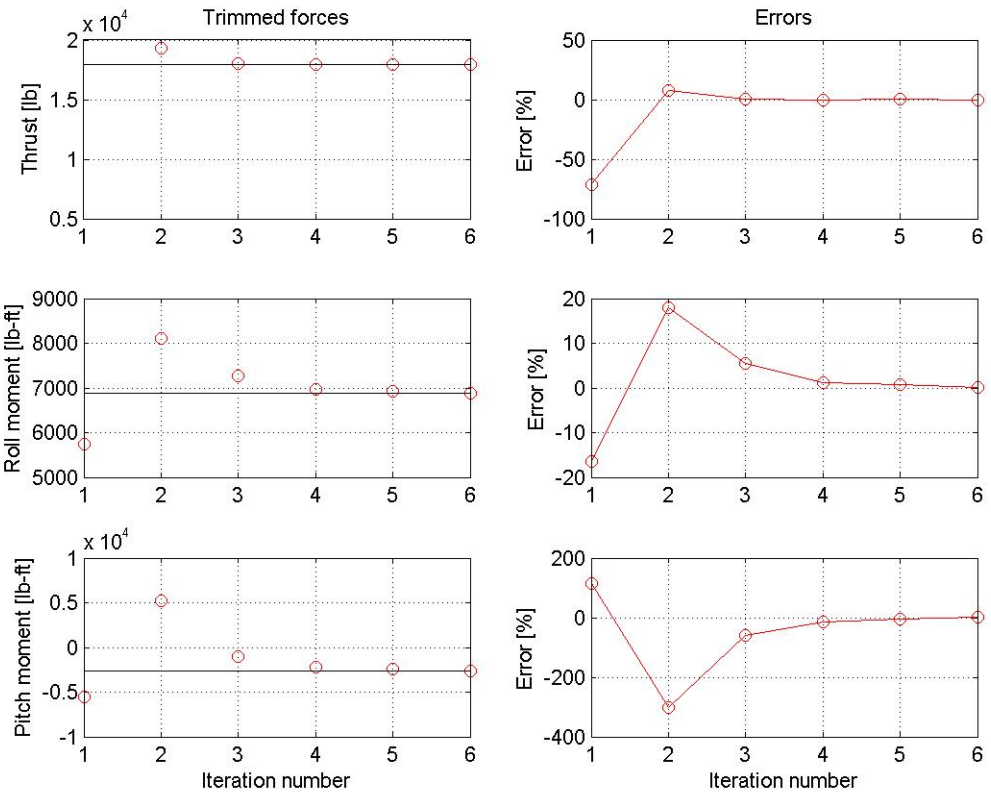

Figure 21: Trimmed thrust and moments, and errors, where the horizontal lines in the figures on the left are the target values [6].

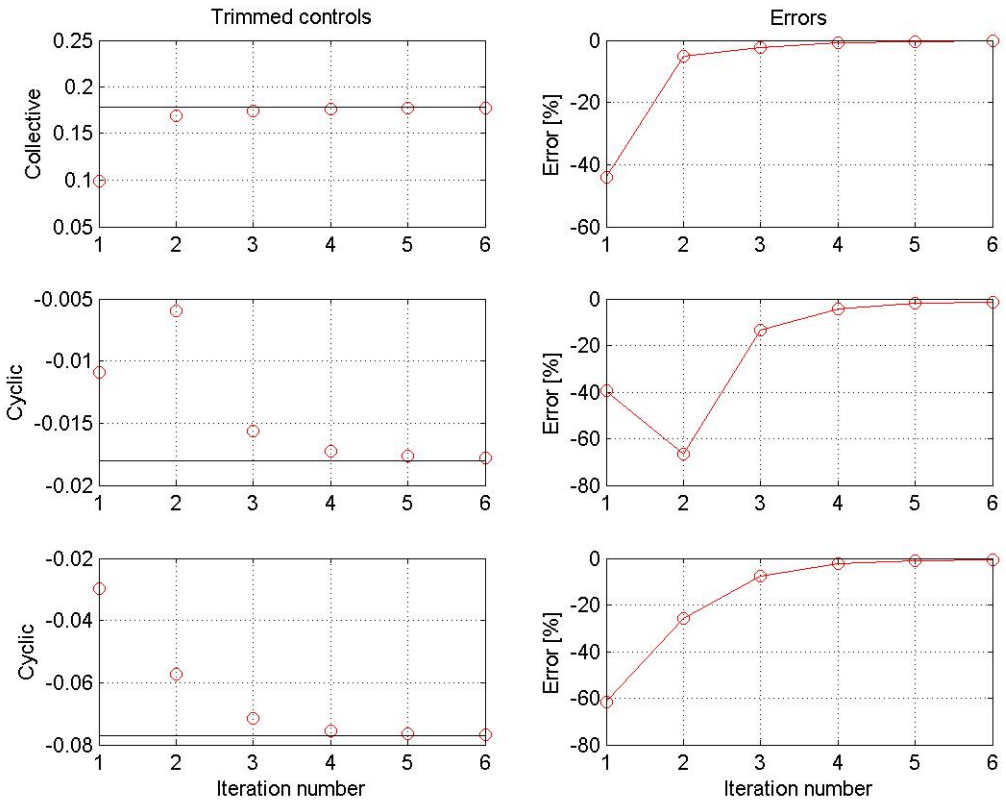

Figure 22: Trimmed swash plate displacement and tilt, and errors, where the horizontal lines in the figures on the left are the autopilot solutions [6].

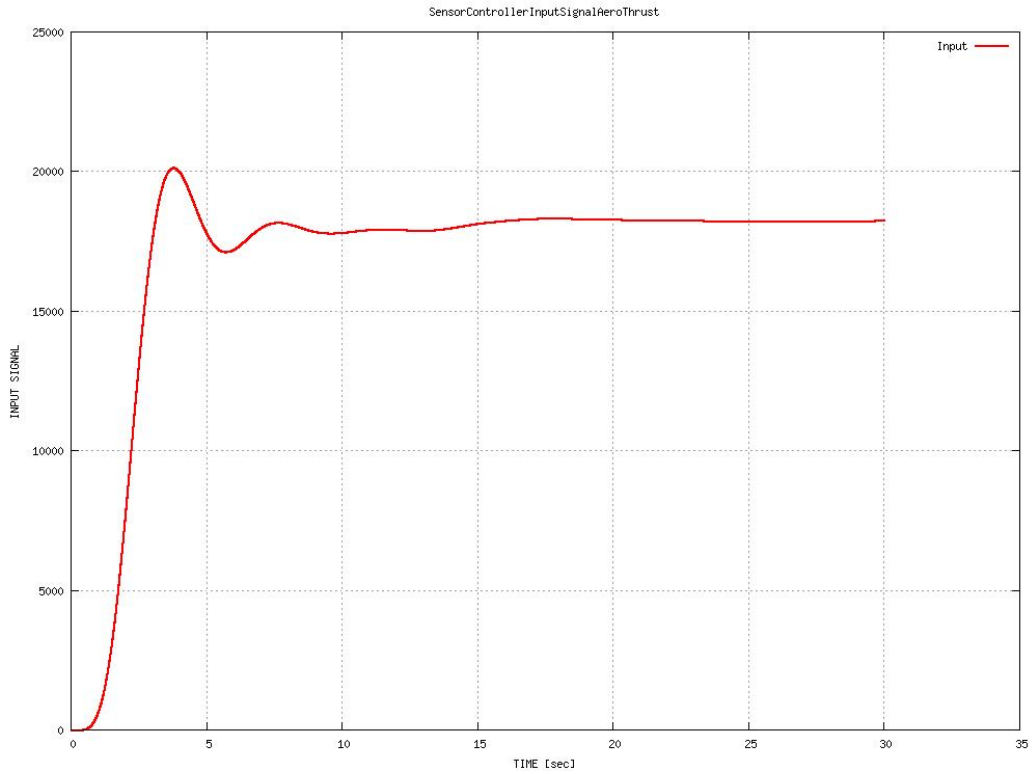

Figure 23: Time history of the thrust from quasi-steady trim run.

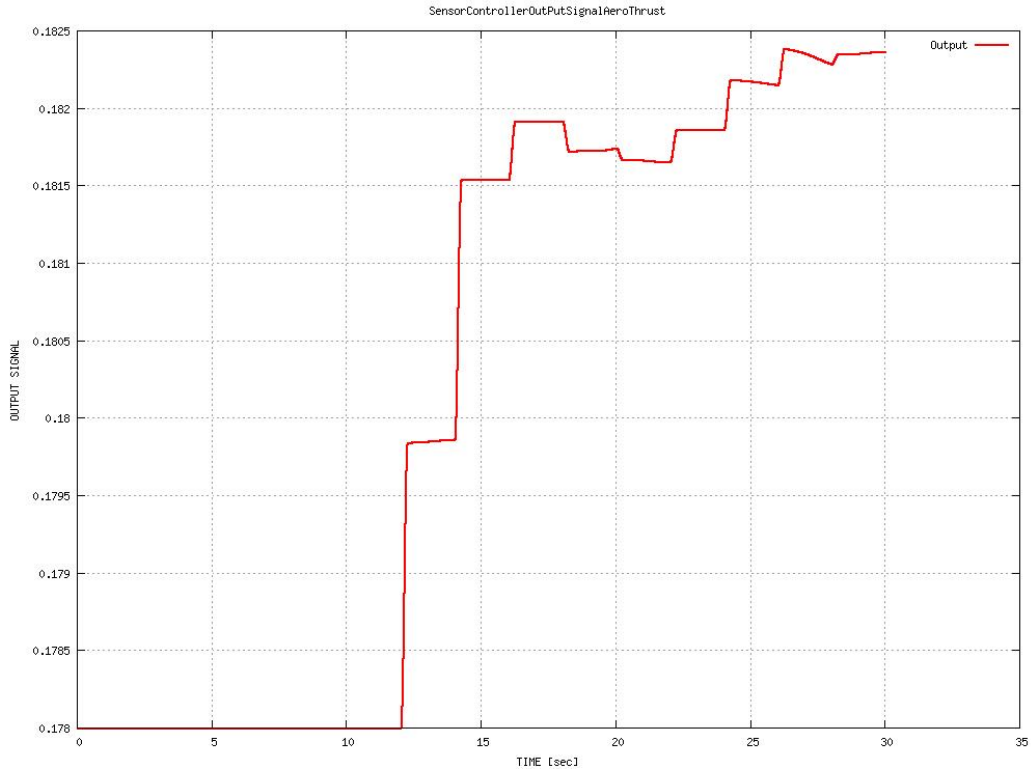

Figure 24: Displacement change of swash plate from quasi-steady trim run.

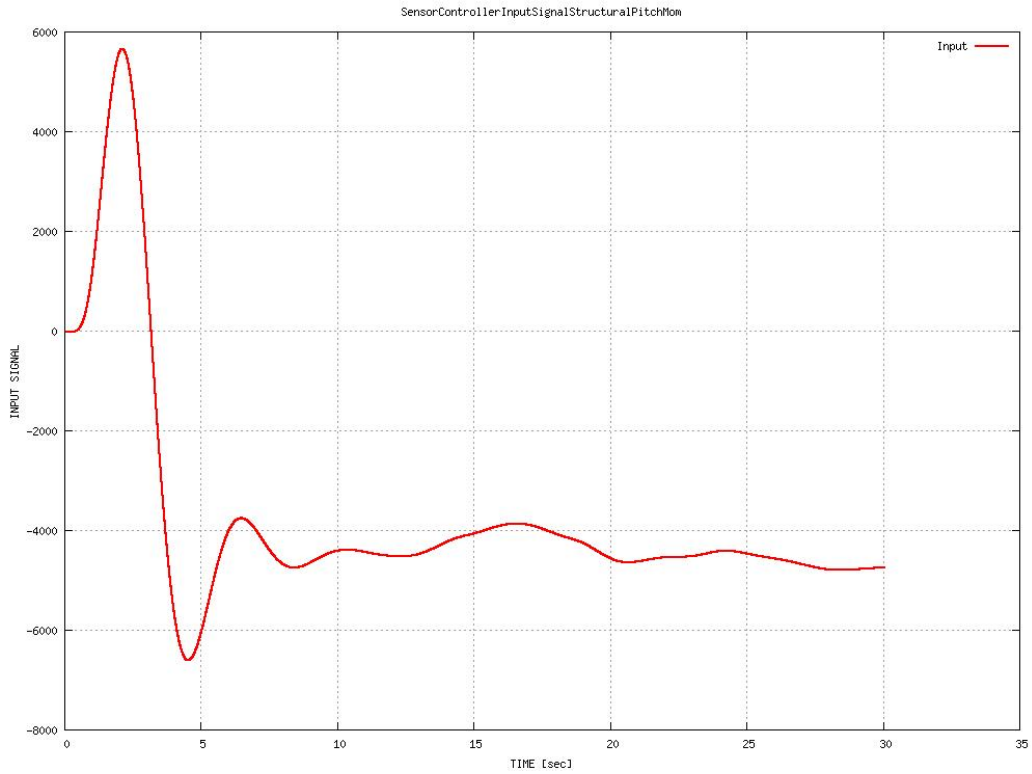

Figure 25: Time history of the rolling moment from quasi-steady trim run.

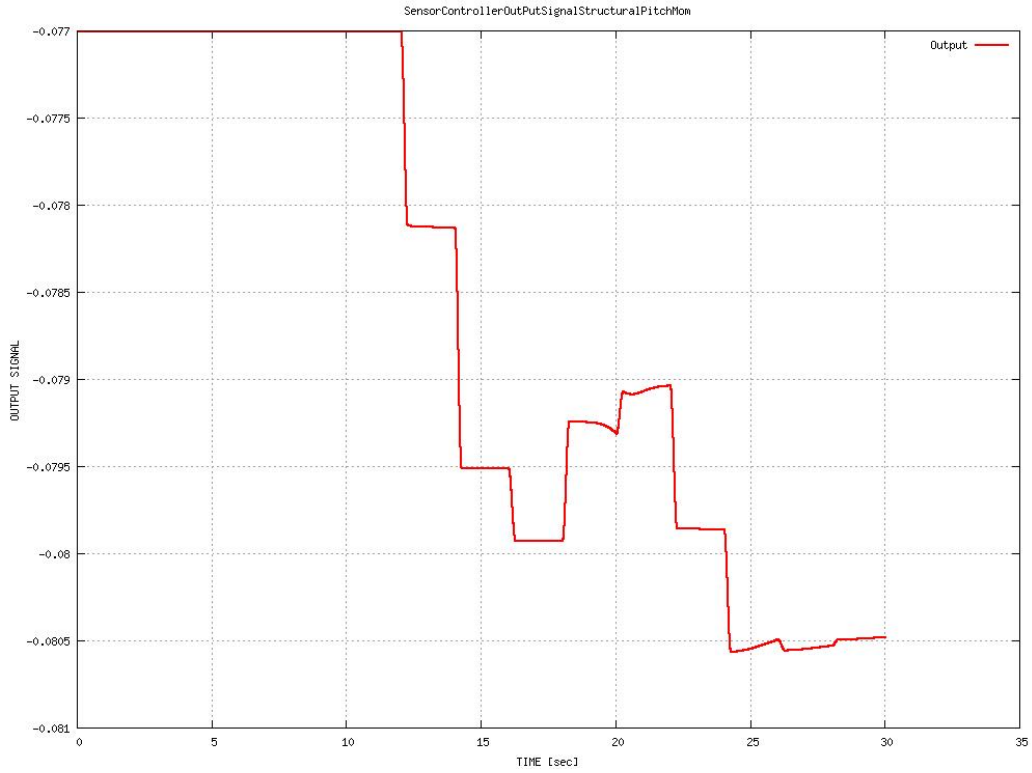

Figure 26: Change of the lateral tilt of swash plate from quasi-steady trim run.

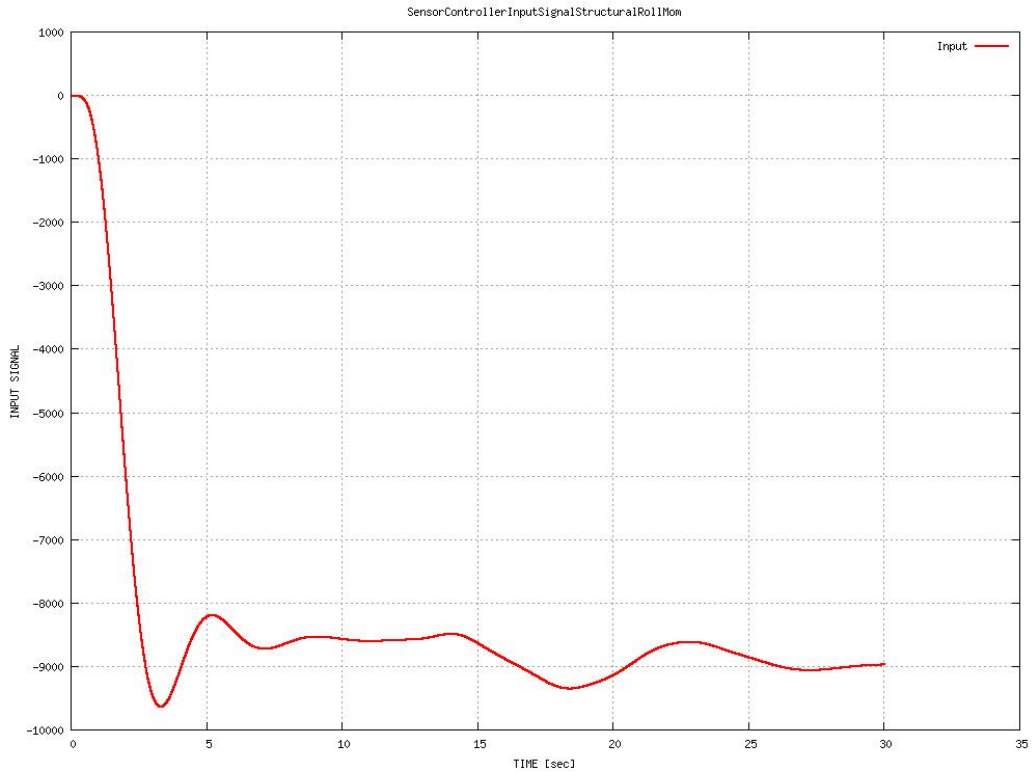

Figure 27: Time history of the pitching moment from quasi-steady trim run.

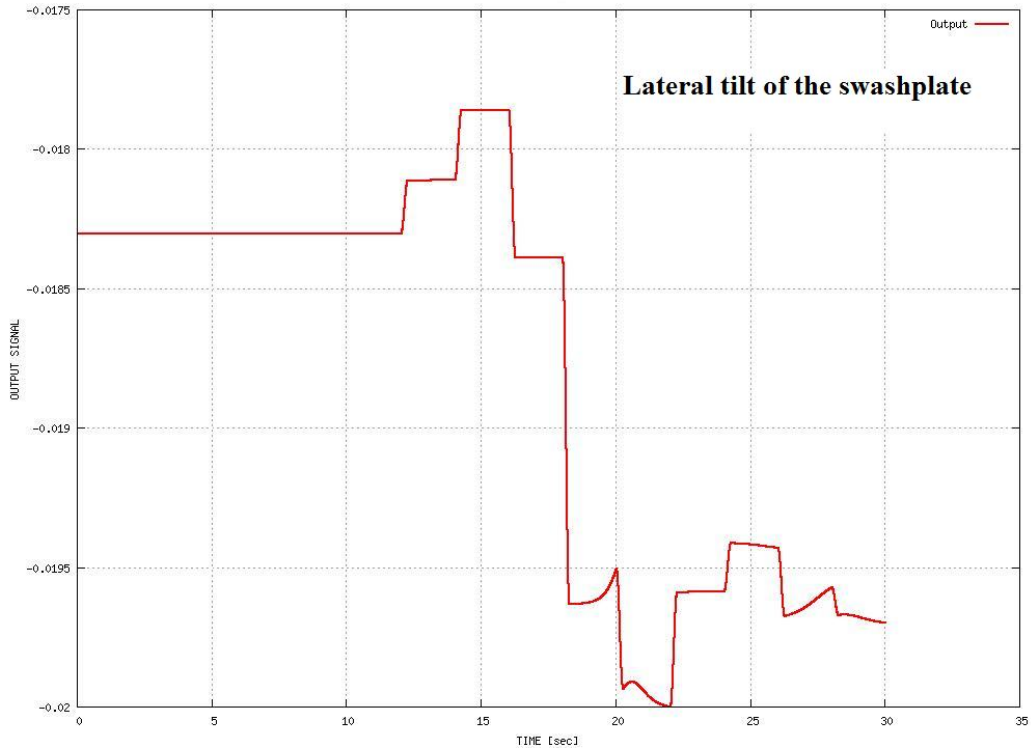

Figure 28: Change of the longitudinal tilt of swash plate from quasi-steady trim run.

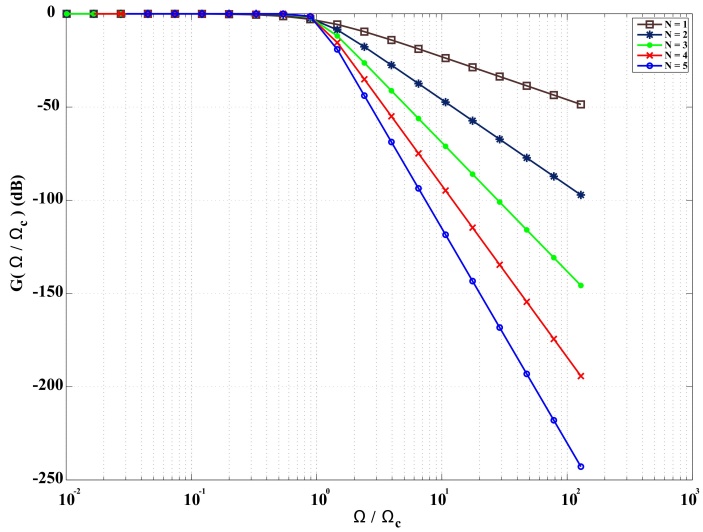

Figure 29: Gain of the normalized Butterworth low-pass filter for $N = 1, 2, \ldots, 5$.

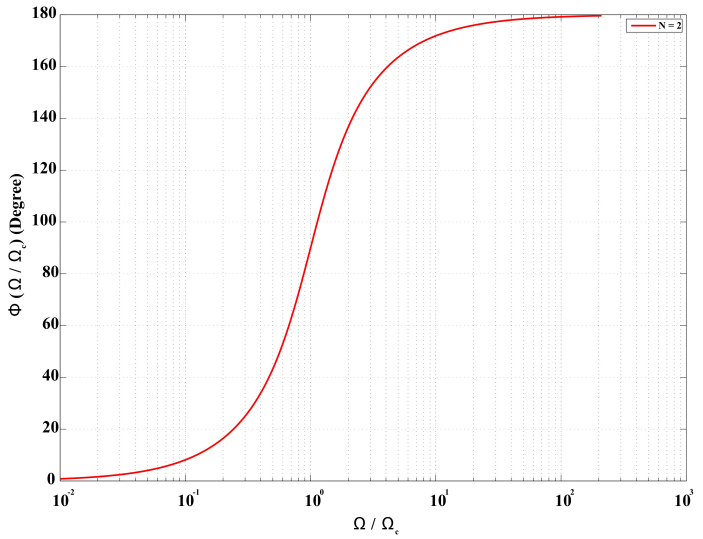

Figure 30: Phase of normalized Butterworth low-pass filter for $N = 2$.

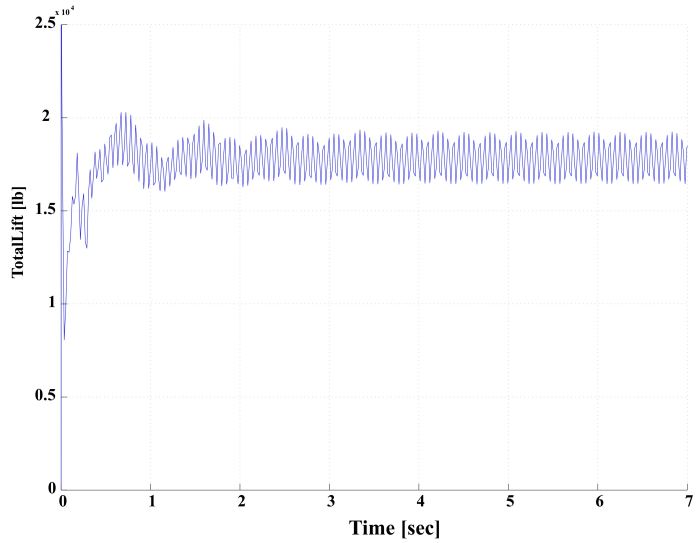

Figure 31: Output created by signal `SignalTotalLift`.

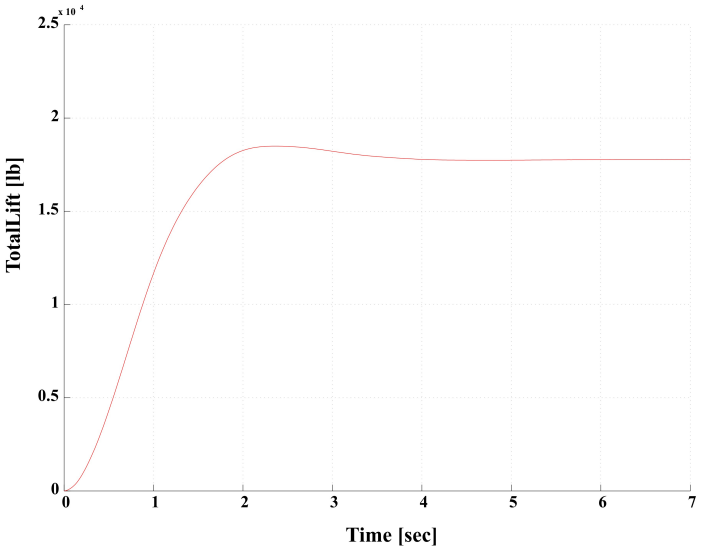

Figure 32: Output created by The lowpass filter `ButterWorth`.

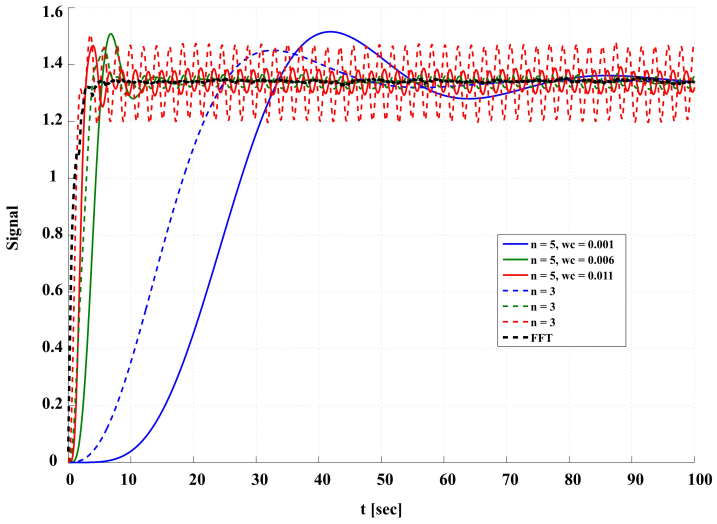

Figure 33: Comparing Butterworth filter to on-line FFT.

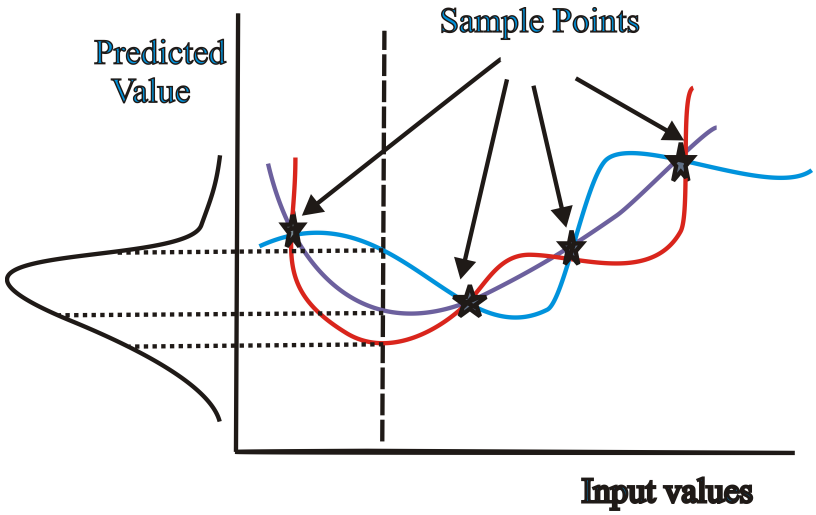

Figure 34: Possible various functions to fit the same set of data, yielding a distribution.

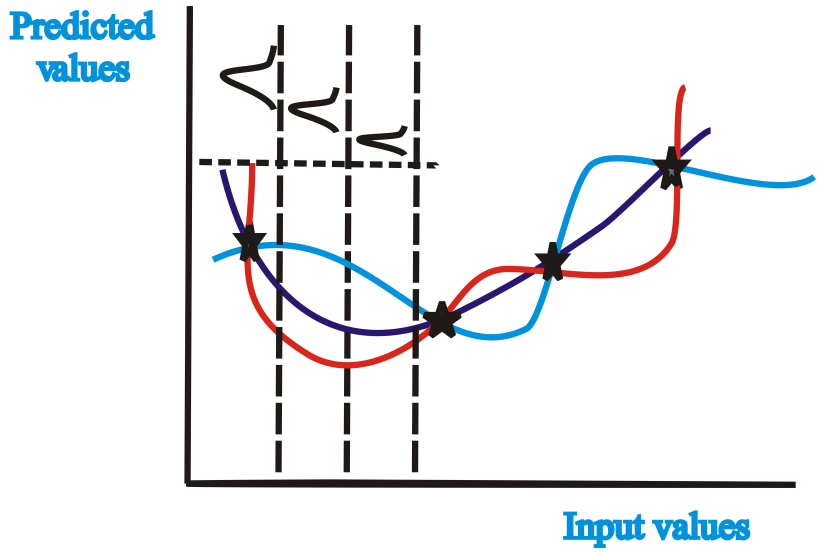

Figure 35: Change of the variance of the prediction depending on its distance from the sampled points.

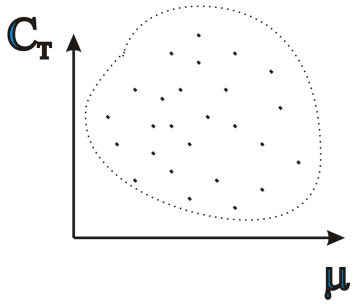

Figure 36: Example of design of experiment for rotorcraft simulation.

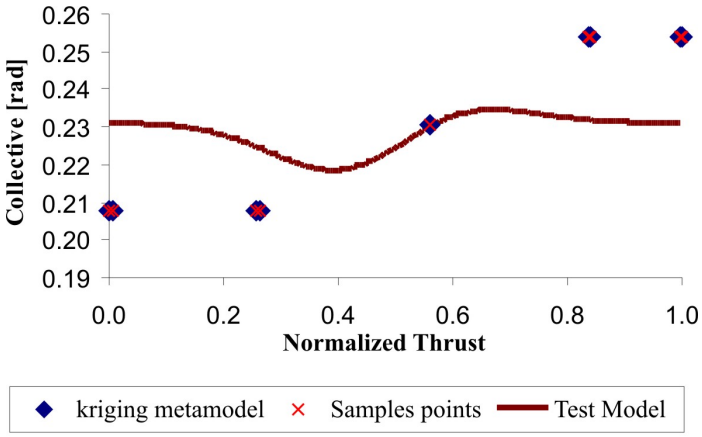

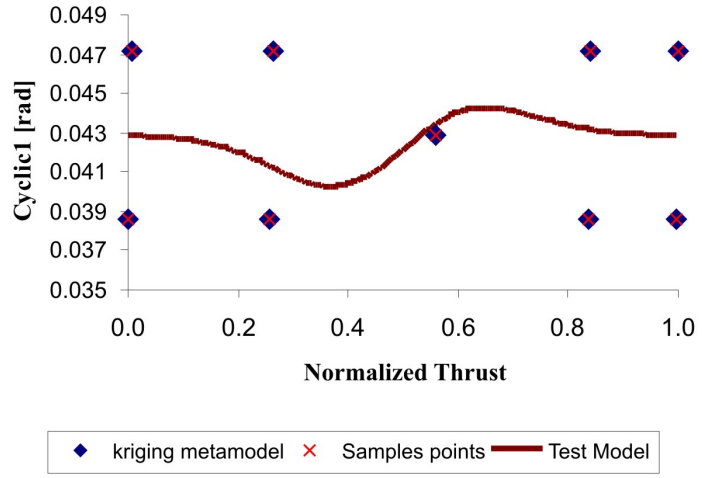

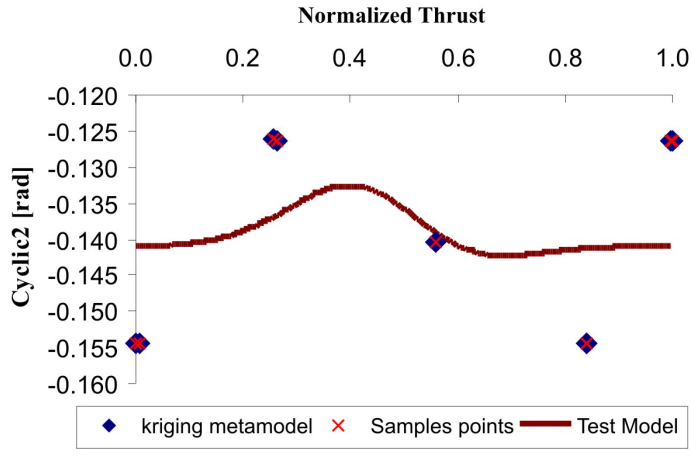

Figure 37: Normalized thrust - control meta-models

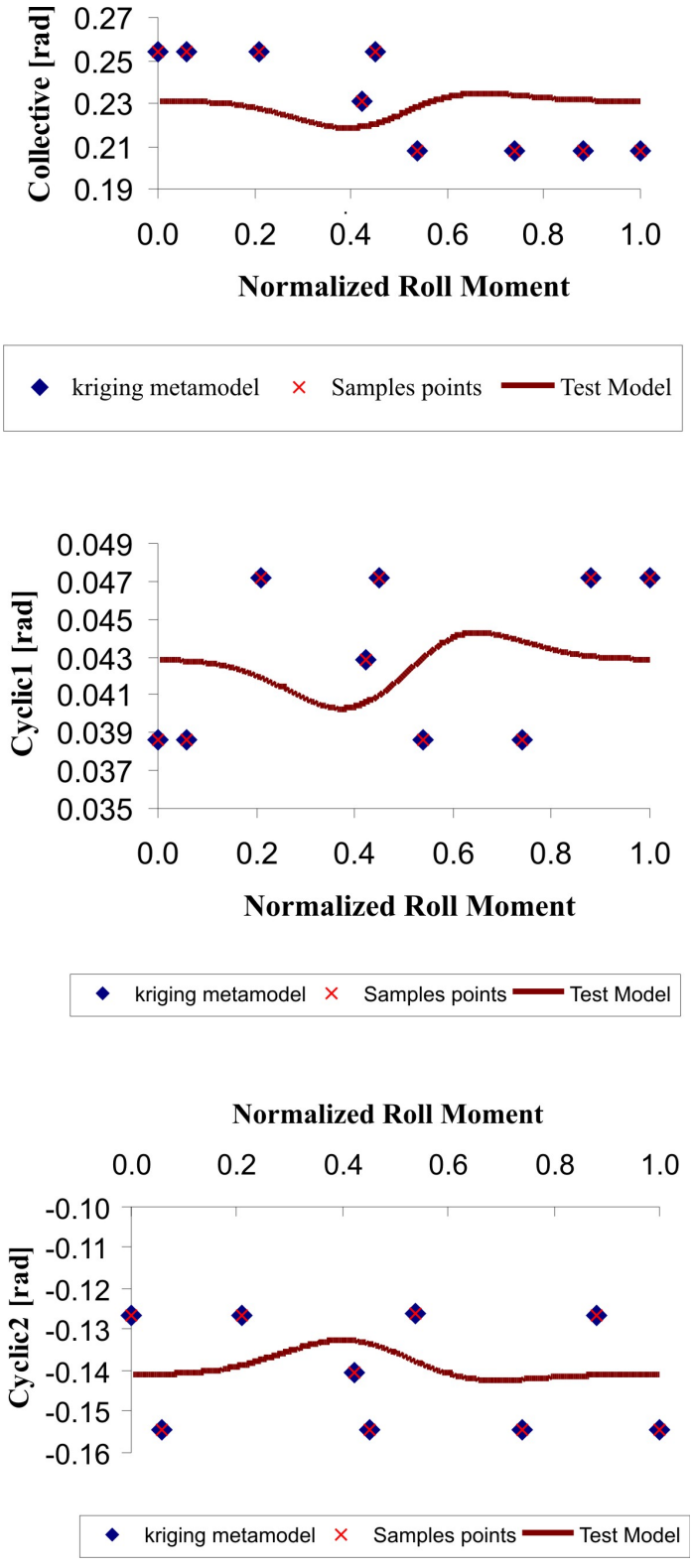

Figure 38: Normalized roll moment - control meta-models

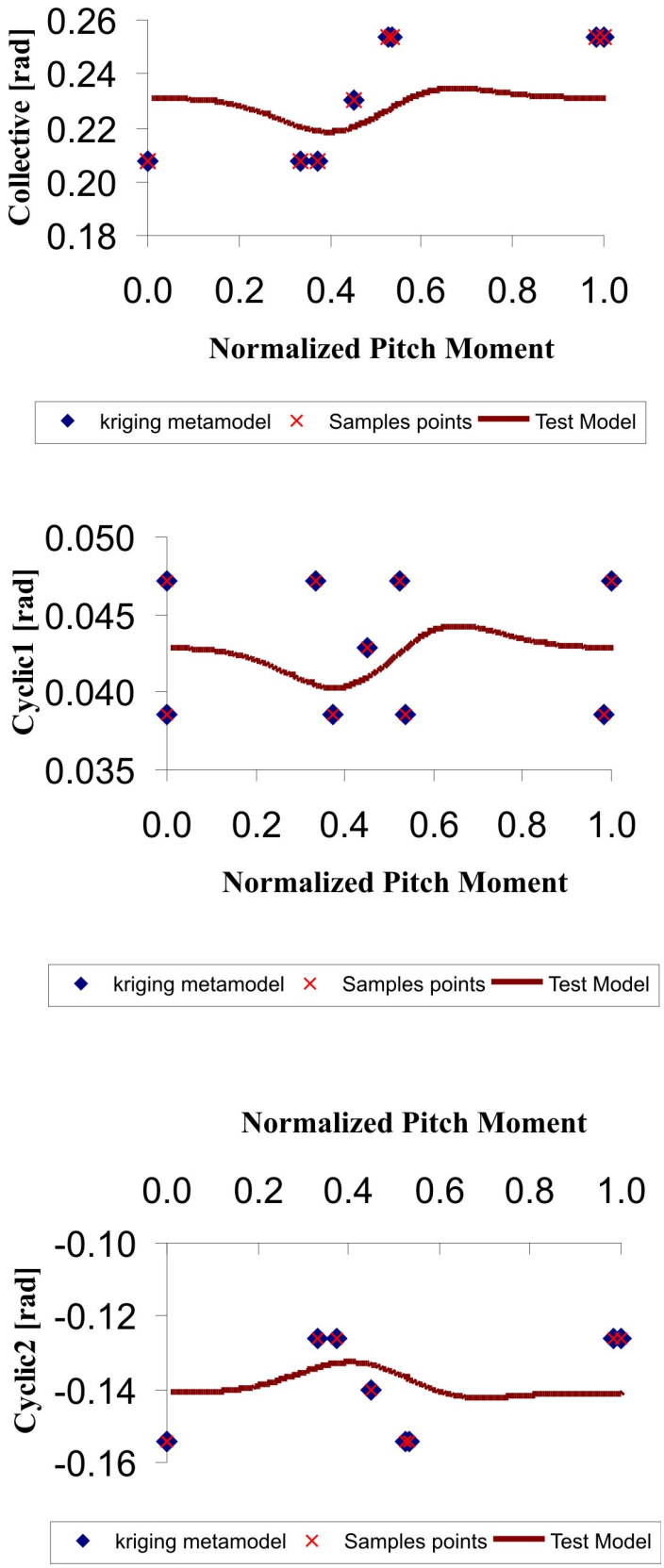

Figure 39: Normalized pitch moment - control meta-models

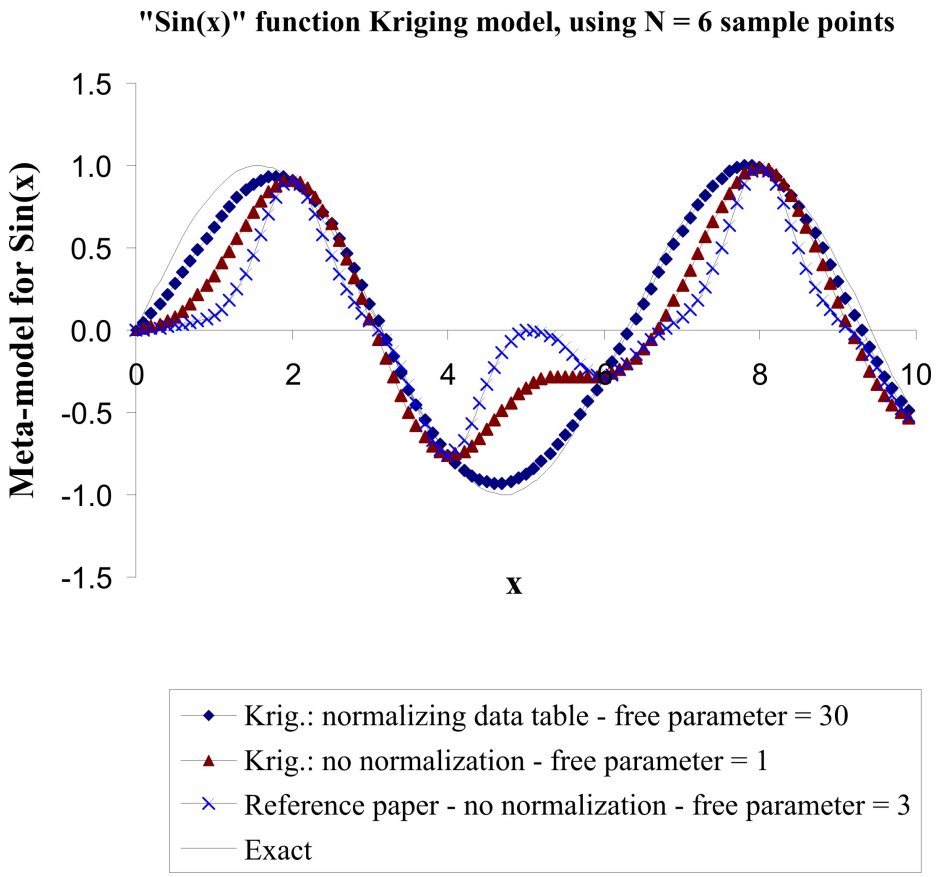

Figure 40: Comparing kriging meta-models predictions for different free parameters.

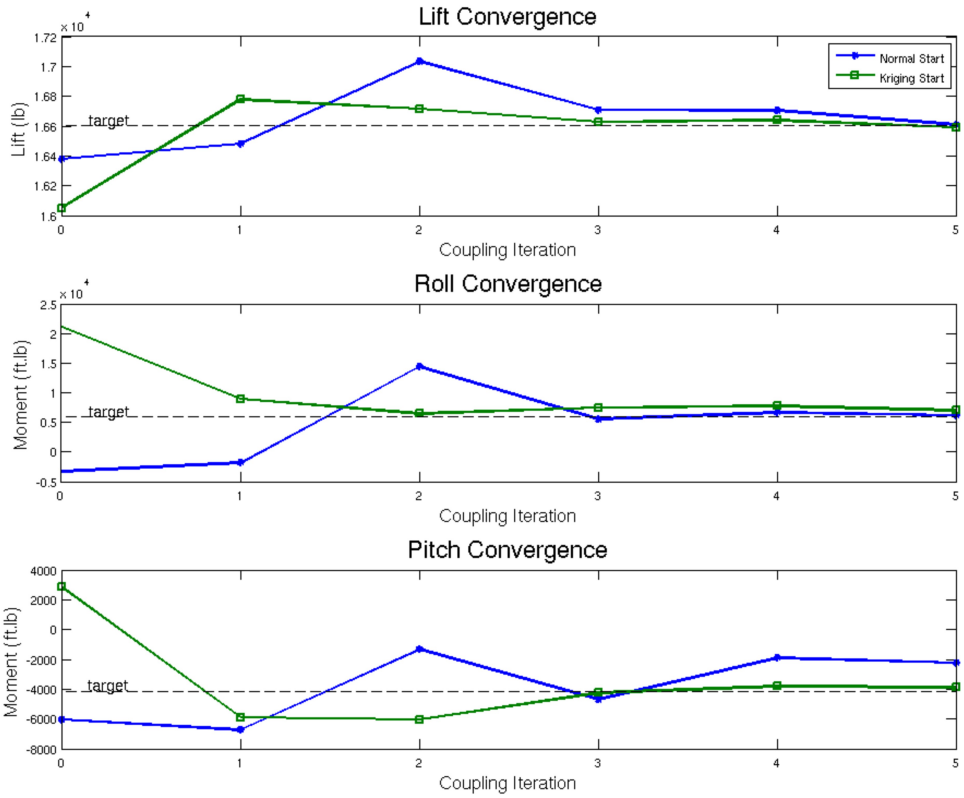

Figure 41: UH-60A case 8534 loads convergence using kriging to estimate the initial controls (collective, longitudinal and lateral cyclics) for a loose-coupling simulation and compared with a simulation using a traditional autopilot control estimates.

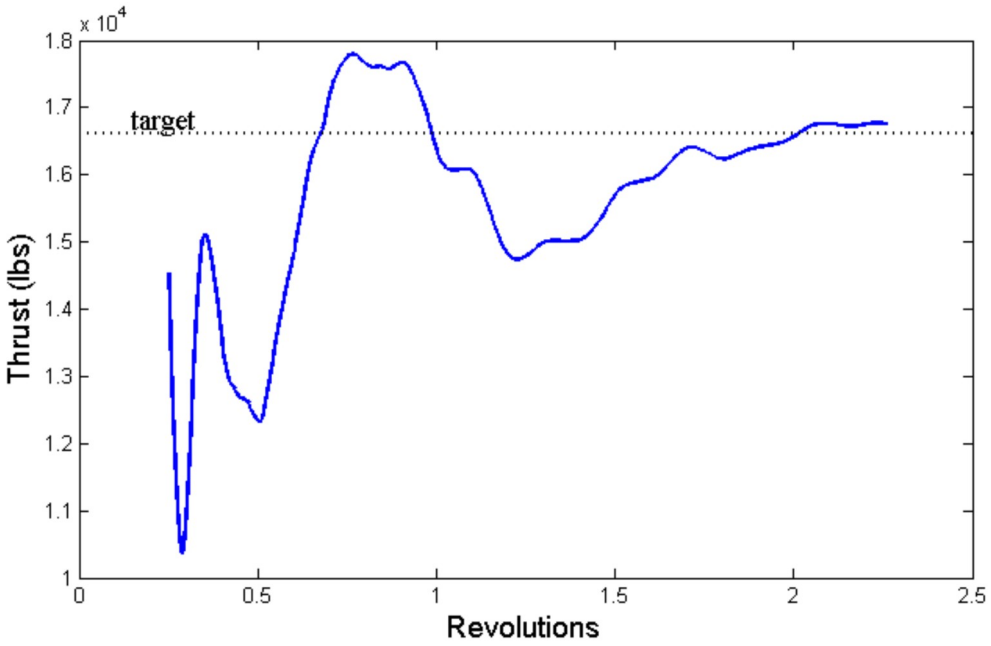

Figure 42: Thrust for the UH-60A case 8534 with trim at each CFD time step using kriging to estimate the appropriate control.

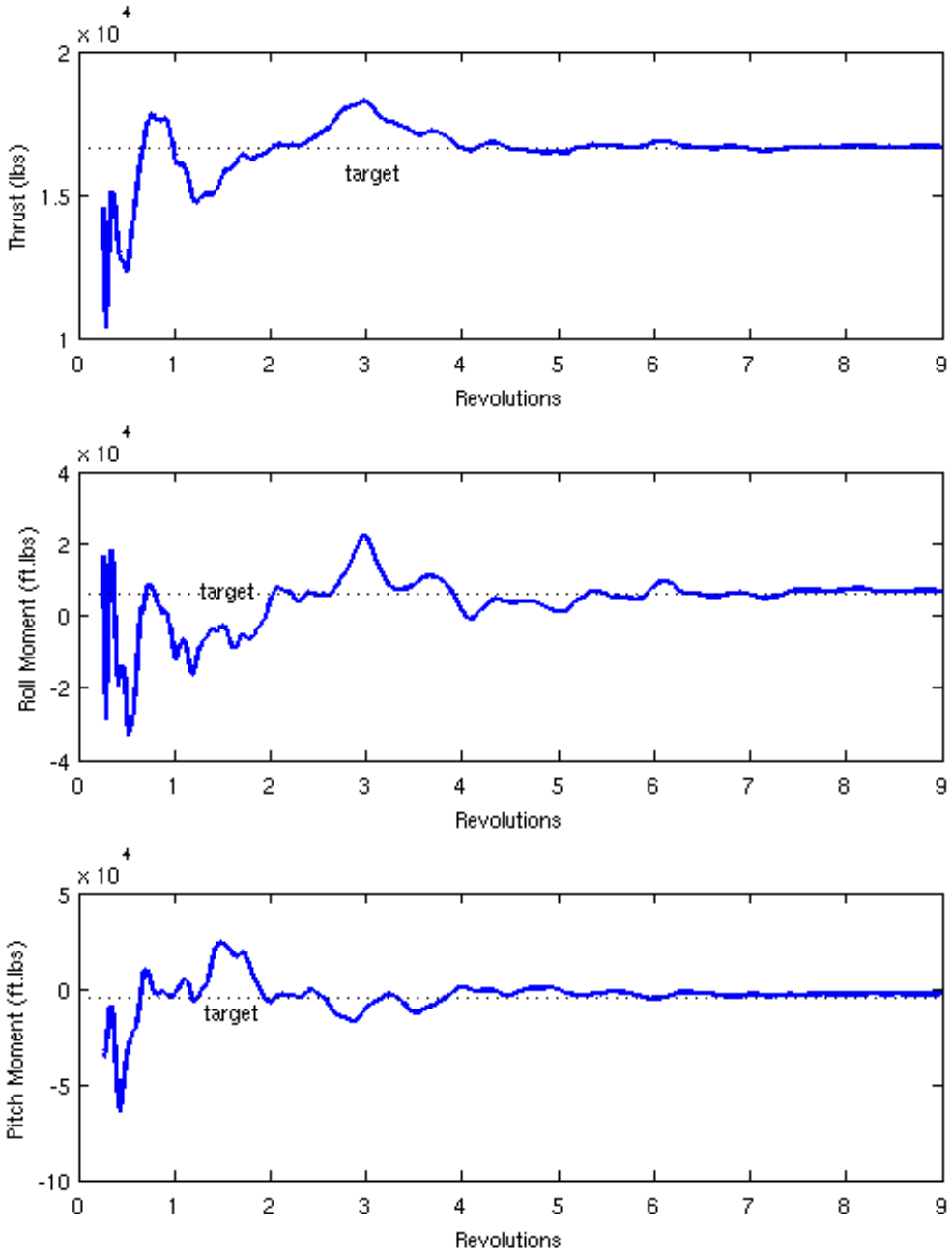

Figure 43: Airloads for the UH-60A case 8534 with trim at each CFD time step using kriging to estimate the appropriate control.

Chapter IV

CFD/CSD COUPLING INTERFACE

4.1 Introduction

As briefly mentioned in chapter 1, DYMORE was modified such that its three main stages: Initialization, Time step/Time loop and Post-processing are called by simple separated routines to allow an easy external call of these main functions, as shown in figure 44. This code organization allowed DYMORE to be coupled with any external CFD code, either by being compiled together or by using Python script as explained in the next section.

Figure 44: DYMORE three main stages.

A kinematic interface was created in DYMORE to provide airstations positions, orientations, linear and angular velocities. Similarly, a load interface was also created in DYMORE to allow a direct setting of the airstations airloads that are computed by the CFD code (or any other source). The structure of these interfaces is shown in figure 45.

First, both interfaces were tested and validated using DYMORE stand alone tests runs by checking the data gathered and set through them. Then the communication between CFD/CSD implemented interfaces codes was tested by validating the exchanged data between the interfaces and the translated data inside each code. The results validate the implemented interfaces: the exchanged data is properly handled to account for frames changes, sign conventions, blade number and sequence, and

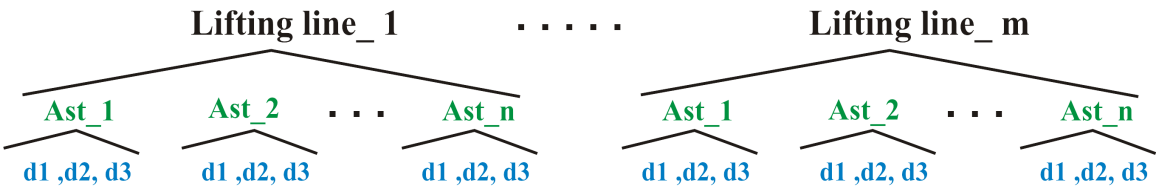

Figure 45: Structure of load and kinematic interfaces.

units.

For the work presented in this chapter and next, tight coupling was achieved by compiling the DYMORE code into a static library with a CFD interface that could then be linked into the OVERFLOW CFD code. This way, the CFD code controls the coupling process from inside itself. It is also possible to achieve tight coupling by linking the codes through Python or another scripting language. The overall tight coupling strategy is shown in figure 46. This tightly coupled time stepping continues until the simulation is complete, and then the CFD and CSD codes continue with their respective post-processing routines.

4.2 Computational Modeling

4.2.1 Computational Fluid Dynamics Method

The OVERFLOW [17, 18, 37] CFD methodology was chosen as the platform for the CFD/CSD runs presented in this chapter and the next one. Spatial algorithms within the code vary from 2^{nd} order central difference schemes to 6^{th} order WENO schemes. Second-order time accuracy is achieved through dual time stepping or Newton sub-iterations in conjunction with a first-order implicit time algorithm. Explicit boundary conditions are applied to all types of grids (O-,H-,C-). Several different turbulence models available in OVERFLOW includes the Menter kω-SST two-equation

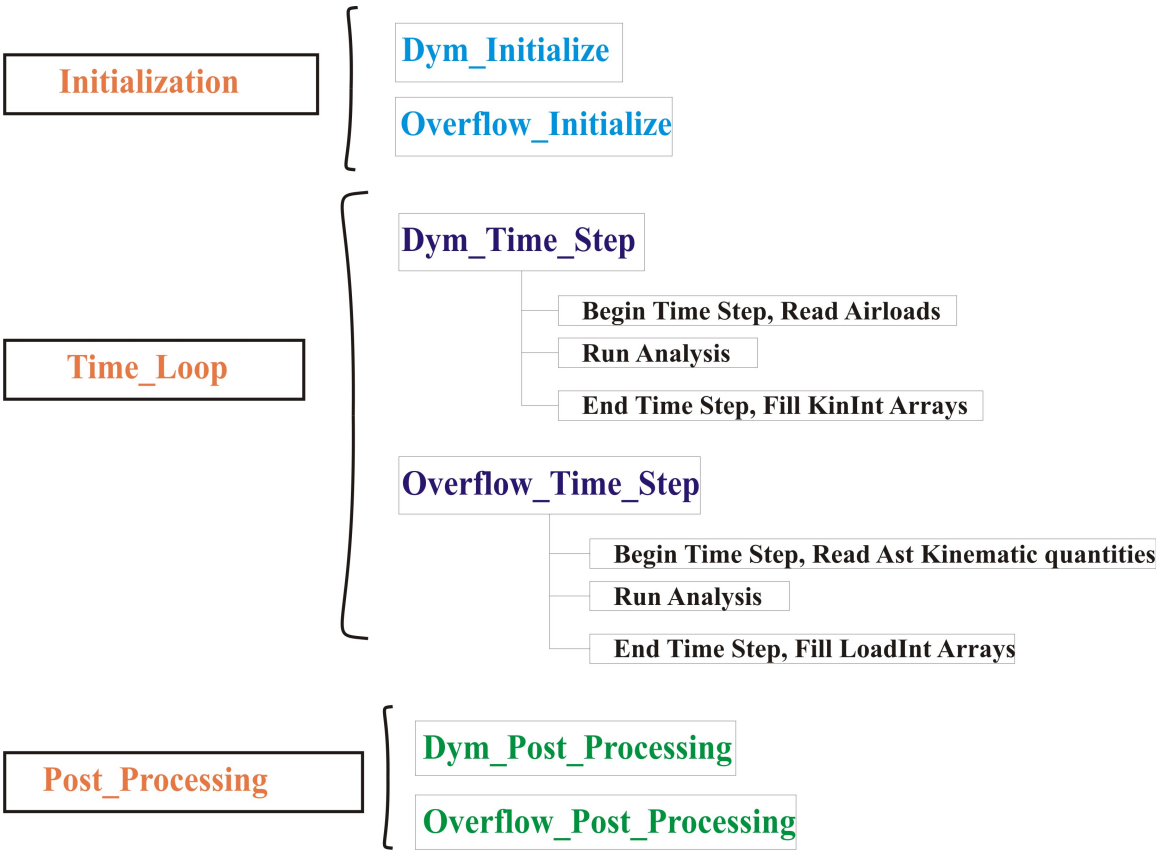

Figure 46: The overall tight coupling strategy.

turbulence model [61] and HRLES-SGS [56, 76, 78, 79]. HRLES hybrid model was developed by Sanchez-Rocha et al. [79], and is based on a two-equation RANS model, blended with an LES resolution of the k-equation, resulting in a modified value of the turbulent eddy viscosity [56].

4.2.2 Description of the rotor model used for runs

The UH-60A helicopter flight test database [45] has become the correlation standard for CFD/CSD coupling. The UH-60A rotor is a fully-articulated system that exhibits all possible motions and thus requires that all the hinge motions are modeled. The articulated motion consists of three components: pitch, flap, and lead-lag components beside a higher harmonic content that is greater than zero, as well as hinge offsets and shaft tilt.

The runs studied next deal with a detailed aeroelastic model of the UH-60A rotor system shown in figure 47. The description of the physical properties of the rotor can be found in reference [15]. The the UH-60A rotor aeroelastic simulation involves both structural and aerodynamic states.

The structural model of the UH-60A involves four blades connected to the hub through blade root retention structures and lead-lag dampers. Each blade was discretized by means of ten cubic finite elements using the finite element based multibody dynamics code described in reference [5]. The root retention that connects the hub to the blade was separated into three segments and modeled by one, two and two beam elements labeled segment 1, 2, and 3 in figure 47. The flap, lead-lag and pitch hinges of the blade were described by three revolute joints connecting the first two segments of the root retention structures. Prismatic joints were used to model the lead-lag dampers that are assumed to be dashpots with nonlinear properties.

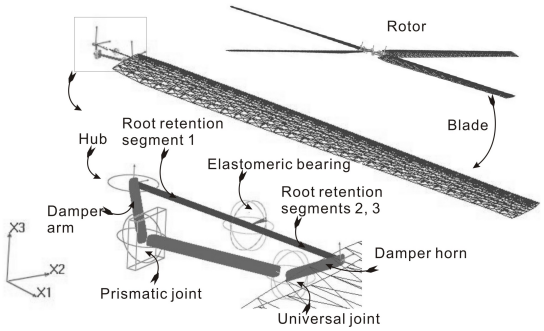

Figure 47: Schematic of the UH-60A rotor system.

The aerodynamics model of the UH-60A involves its four blades. CFD complete overset mesh of the UH-60A model is shown in figure 48(a) that contains all four blades. The complete overset grid has 44 grids for a total of 5.165 million points. Each blade shown in figure 48(b) has 81 spanwise stations. The stations of each blade are clustered at the root and tip (figure 48(c)) with 105 surface nodes in the chordwise direction at each station. Also each blade has a tip and a root cap grid at each of its ends. However these grids were not considered for calculating forces and

moments due to their small size and effect. Although the complete four blades overset shown in figure 48(a) does not represent the optimal CFD grid used for determining in particular the drag of the system, it is sufficient to demonstrate the ability to perform the CFD/CSD loose and tight coupling procedures.

4.2.3 CFD/CSD loose and tight coupling results

As mentioned previously, to incorporate the upgrades and modifications in both the CSD and the CFD codes used in this study (DYMORE and OVERFLOW), loose coupling runs were carried for two forward flights cases: case 8534 and case 9017 [1]. Their corresponding flight parameters are listed in table 16. The trimming procedure was carried out using the autopilot control law. Figures 49-50 show the

Table 16: UH-60A Flight Cases Counter

Counter	C_T/σ	μ	M_∞
case 8534	0.084	0.37	0.236
case 9017	0.129	0.24	0.157

loose coupling iteration history of the controls and loads respectively for the 8534 flight case. The results in these figures were obtained by using HRLES turbulence model with OVERFLOW. These results show that both the thrust and the roll moment after 5 iterations showed good convergence. As a conclusion this test converged to the target loads within some accepted error with respect to the pitching moment target value.

Figures 51-52 show the loose coupling iteration history of the controls and loads respectively for the 9017 flight case. The results in these figures were obtained by using HRLES turbulence model with OVERFLOW. While figures 53-54 show the convergence history for this same flight case but with the $k-\omega$ SST turbulence model. These results show much better improved convergence for the later case.

[1] See Acknowledgments.

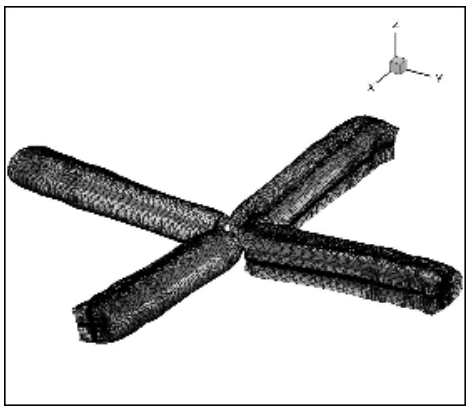

(a) UH-60A complete overset 4 blades CFD mesh.

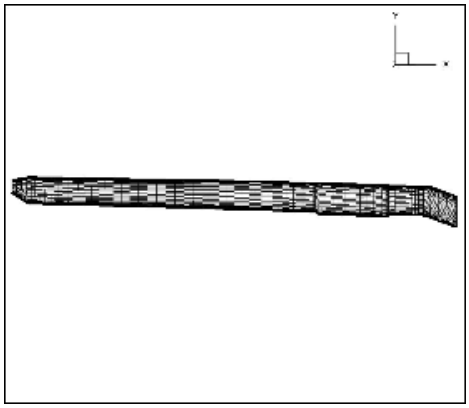

(b) UH-60A blade CFD mesh.

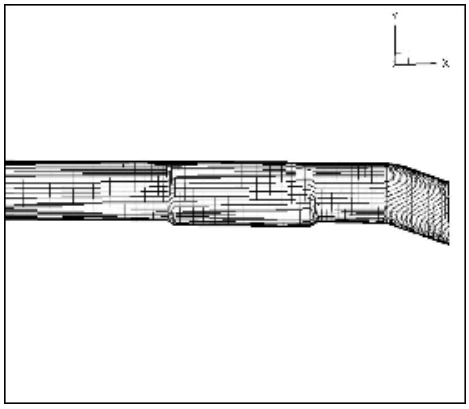

(c) UH-60A blade-tip CFD mesh.

Figure 48: UH-60A CFD mesh used to demonstrate the CFD/CSD tight coupling.

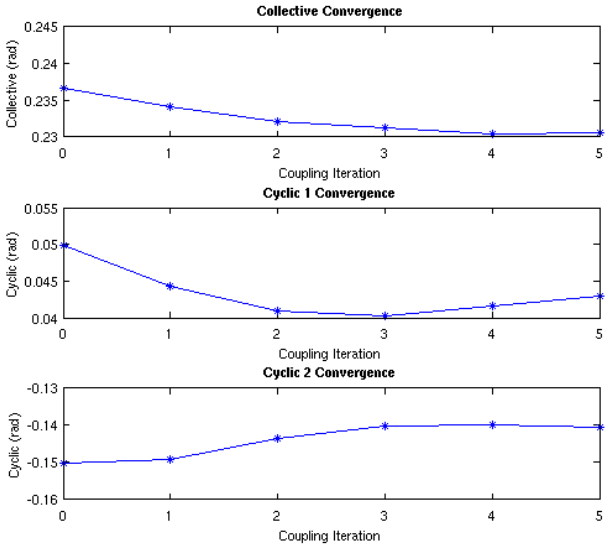

Figure 49: Loose coupling controls convergence history for case 8534 run with HRLES.

Finally, a tight coupling run was performed for case 8534, using the last loose coupling iteration as initial condition to start both DYMORE and OVERFLOW to minimize the transient perturbations once the two codes begin to run together for direct aeroelastic simulation. UH-60A runs were performed on 24 SGI processors. The simulation of each CFD/CSD quarter revolution took around 8.25 hours. Figures 55-57 show that after the tight coupling run for 2 revolutions, the loads predicted by the tight coupling almost matched the last loose coupling iterations. The results verify the tight coupling process carried through the two codes loads and kinematics interfaces. The results also prove the ability of the implemented interfaces to exchange the data and to translate these data correctly in respect to the right frames, directions, blades, and dimensions.

After the tight coupling was verified, the run was carried for several revolutions then moderate perturbation loads were applied (the perturbation loads should be carefully applied to not exceeds the limit that will destabilize this aeroelastic simulation), as explained in the next chapter.

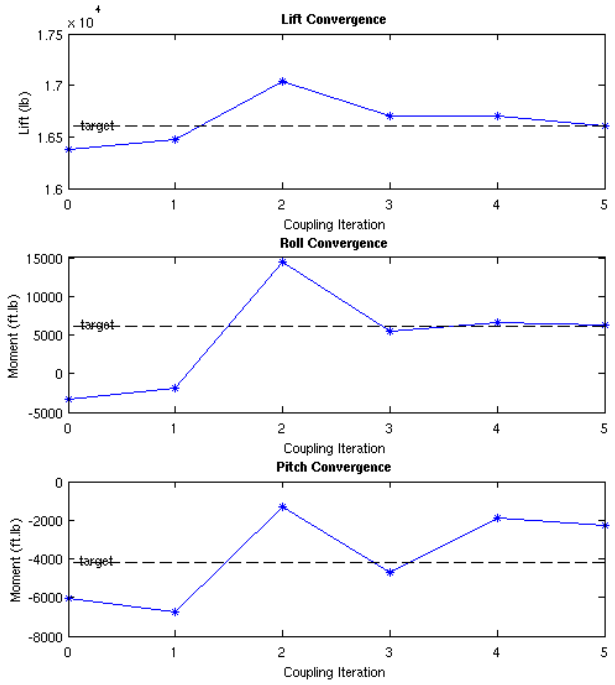

Figure 50: Loose coupling loads convergence history for case 8534 run with HRLES.

The CFD/CSD results presented in this chapter served to demonstrate the validity of the tight coupling process developed as part of this research effort. Additional results and analysis of the physics for various rotors can be found in Reveles [76] and Lynch [57], as well as future publications by these authors.

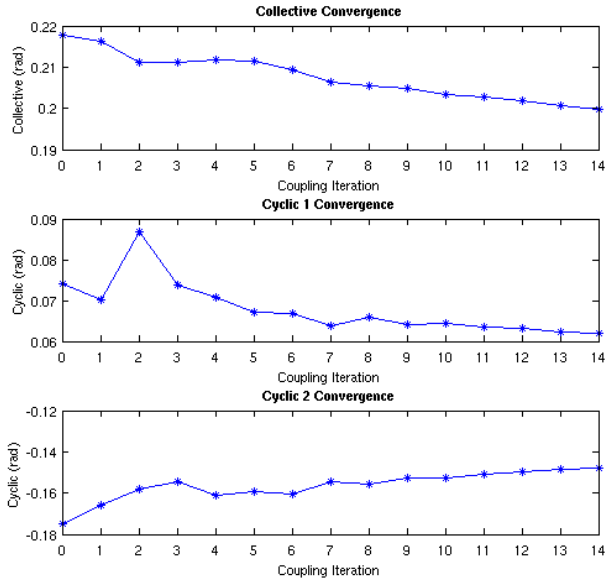

Figure 51: Loose coupling controls convergence history for case 9017 run with HRLES.

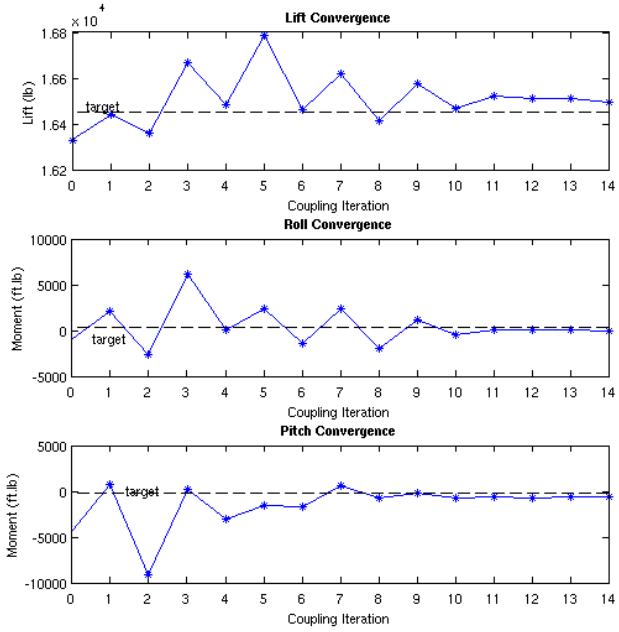

Figure 52: Loose coupling loads convergence history for case 9017 run with HRLES.

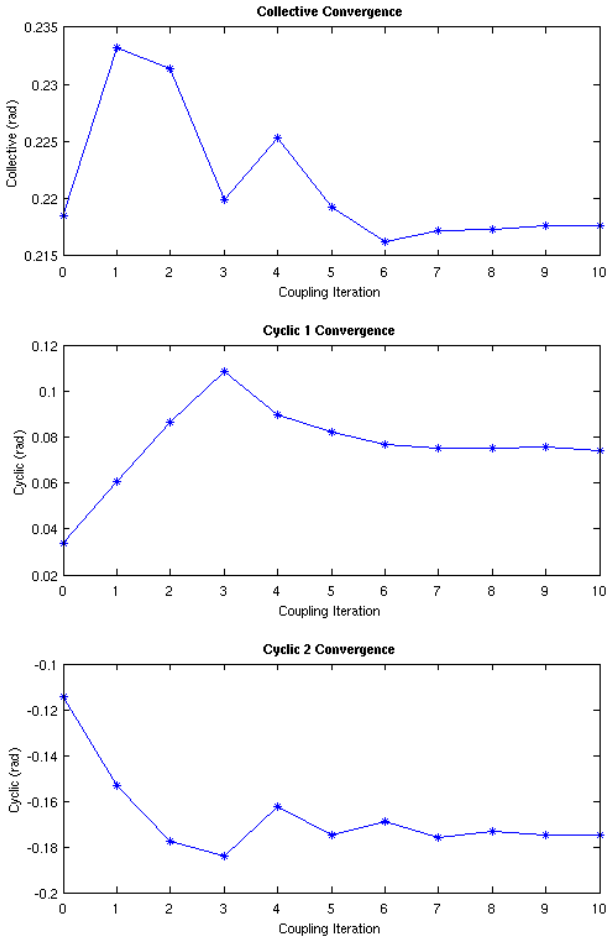

Figure 53: Loose coupling controls convergence history for case 9017 run with kwSST.

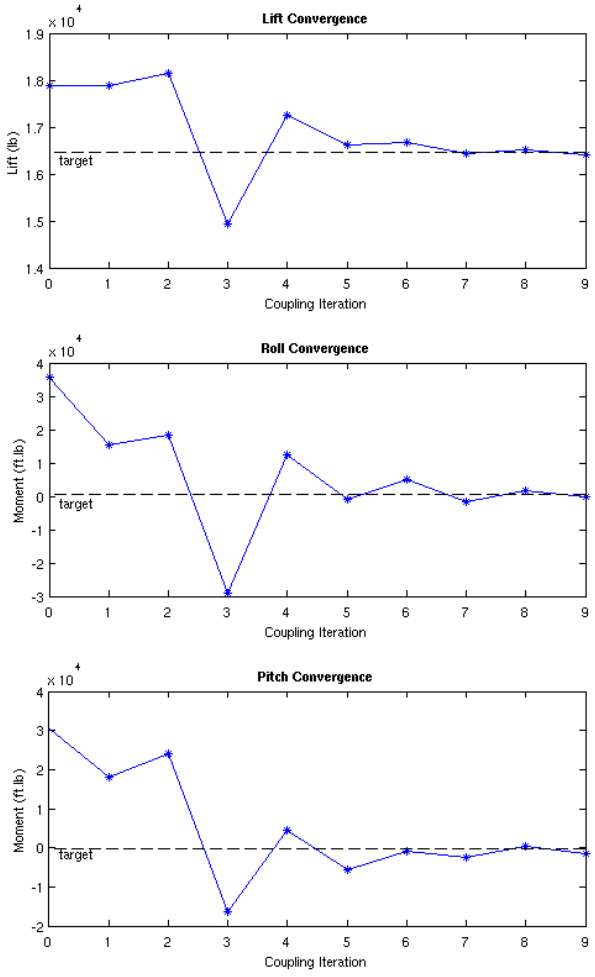

Figure 54: Loose coupling loads convergence history for case 9017 run with kwSST.

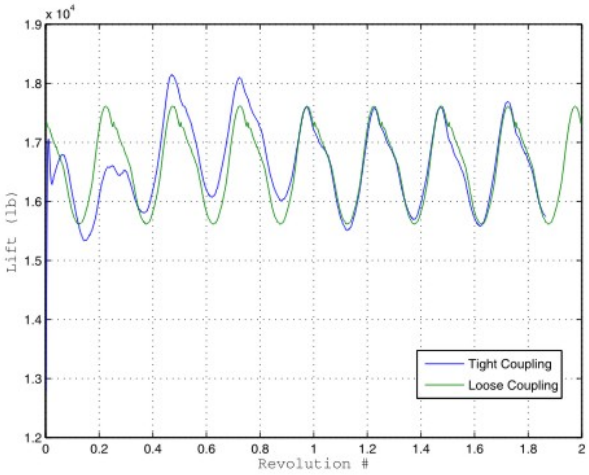

Figure 55: Loose and tight coupling thrust comparison.

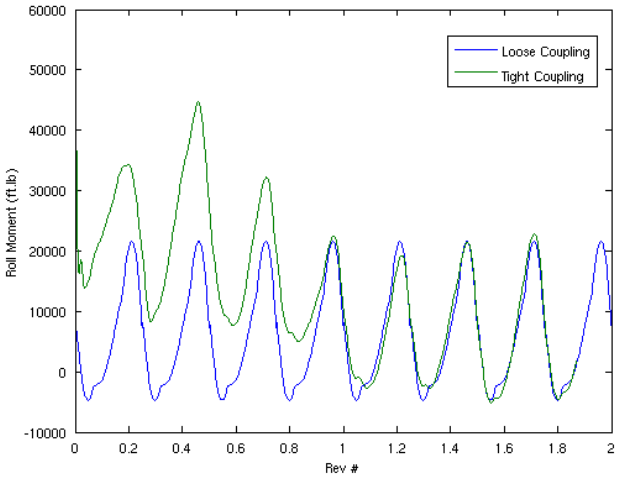

Figure 56: Loose and tight coupling roll moment comparison.

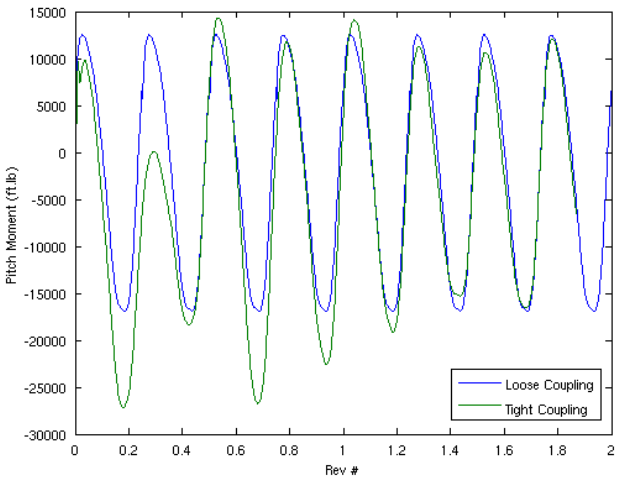

Figure 57: Loose and tight coupling pitch moment comparison.

Chapter V

STABILITY ANALYSIS

5.1 Introduction

The goal of this chapter is to demonstrate the ability of a tightly coupled CFD/CSD based methodology to assess the stability characteristics of complex rotorcraft problems. The stability assessment is undertaken using an algorithm based on a partial Floquet approach that has been successfully applied with CSD tools to rotors by Bauchau and Wang [9] and to wind turbines by Bauchau and Skjolden [82]. The stability analysis approach is computationally inexpensive and consists of post-processing aeroelastic data. This stability analysis approach can be used with any aeroelastic rotorcraft code or with experimental data. Unlike classical stability analysis methodologies, partial Floquet analysis does not require the linearization of the equations of motion of the system, which makes it ideally suited for use in conjunction with the proposed coupled CFD/CSD simulations.

5.2 Stability analysis of rotors and other complex multiply systems

A multibody system, such as a helicopter, can be modeled by a set of nonlinear equations of the form $\dot{\underline{y}} = \underline{g}(t, \underline{y})$, where $\underline{y}$ is a vector containing N state variables, t denotes time, and $\dot{(\cdot)}$ is the derivative with respect to time. The rotor in a level forward-flight can be assumed to initially operate at a constant mean rotor speed and a periodic steady state $\underline{y}_{ss}$. Assuming small perturbations $\underline{x} = \underline{y} - \underline{y}_{ss}$ about the steady state allows the nonlinear system to be approximated by a linear system with periodic coefficients

$$\dot{\underline{x}} = \underline{\underline{A}}(t)\underline{x} + \underline{f}(t) \tag{154}$$

where $\underline{\underline{A}}(t) = \underline{\underline{A}}(t+T)$ is the periodic system matrix of period $T = 2\pi/\Omega$. This system and small perturbations about it can then be analyzed through several different computational methods as described in the next section.

5.2.1 Partial Floquet analysis

The theoretical basis for the analysis of periodic systems, such as rotors, was developed by Floquet [29] who demonstrated that the response of a linear system with periodic coefficients can be modeled as the sum of modal contributions multiplied by an time-dependent exponential term $\rho_k = \exp(\lambda_k t)$. Floquet analysis determines the change in the states of the system at times t and $t + nT$, where nT is the time required for n integer-based periods of the system. λ_k are known as the characteristic exponents, each is defined as a complex variable of the form $\lambda_k = \sigma_k \pm i\omega_k$. The damping coefficient σ_k and principal frequency $\omega_{\mathrm{p},k}$ of mode k are determined from the eigenvalues ρ_k as

$$\sigma_k = \frac{1}{T}\ln(|\rho_k|) \tag{155a}$$

$$\omega_{\mathrm{p},k} = \frac{1}{T}\arctan(\rho_k), \quad \omega_{\mathrm{p},k} \in \,]-\Omega/2, \Omega/2] \tag{155b}$$

To obtain more physically meaningful frequencies for engineering analysis, integer multiples (j_k) of the rotor speed can be added to the principal frequencies as $\omega_k = \omega_{\mathrm{p},k} + j_k\Omega$. The damping ratio can be computed from $\zeta_k = -\sigma_k/(\omega_k\sqrt{1+\sigma_k^2/\omega_k^2})$. The system is stable if, for all values of k, $\zeta_k < 0$.

For large multibody models, a formal linearization of the governing equations is difficult and expensive to obtain for both time invariant systems and periodic systems. To overcome these difficulties, Bauchau and Wang [7,9,10] developed several approaches to stability analysis and demonstrated their applicability to large scale multibody systems. They also verified that these approaches provide identical results with a number of other more complex methods, such as Prony's method or Poincaré mapping.

A distinctive feature of these methods is that they can analyze one or multiple discrete time signals characterizing the dynamic response of the system for either time invariant or periodic systems. Also unlike classical stability analysis methodologies, they don't require the linearization of the system's equations of motion. Consequently, these approaches are computationally inexpensive, consisting of post-processing that can be used with any multi-physics computational tool or with experimental data. One of these approaches uses a singular value decomposition systematically as a mean of dealing with the noisy, highly redundant data sets obtained from nonlinear systems. This approach is referred to as the *Partial Floquet Analysis* (PFA).

The PFA is based on a number of time signals N_h, denoted $h_s(t)$, which are components of the response vector, $\underline{x}$. A typical signal is sampled at times $t = j\Delta t + \ell T$, where j denotes the time step number in the ℓ^{th} period. An array that stores m consecutive data points starting in period ℓ is saved, and n arrays obtained over n periods for all N_h signals are assembled into two Hankel-type matrices, denoted $\underline{\underline{H}}_0$ and $\underline{\underline{H}}_1$ [7, 9, 10], where $\underline{\underline{H}}_1 = \underline{\underline{Q}}\,\underline{\underline{H}}_0$ and $\underline{\underline{Q}}$ is an approximation of the transition matrix. Since all N state variables are not available over the n periods, an exact matrix can not be constructed. Instead, an approximate transition matrix $\underline{\underline{Q}} = \underline{\underline{H}}_1 \underline{\underline{H}}_0^+$ is constructed. The superscripts $(\cdot)^+$ denote Moore-Penrose inverses [33]. The $\underline{\underline{H}}_0$ matrix is factorized using singular value decomposition [33] to provide a factorization $\underline{\underline{H}}_0 = \underline{\underline{\mathcal{U}}}\,\underline{\underline{\mathcal{S}}}\,\underline{\underline{\mathcal{V}}}^T$. $\underline{\underline{\mathcal{U}}}$ contains the proper orthogonal modes of $\underline{\underline{H}}_0$, while $\underline{\underline{\mathcal{S}}}$ is a diagonal matrix storing the singular values of $\underline{\underline{H}}_0$, and $\underline{\underline{\mathcal{V}}}$ is an orthogonal matrix resulting from the factorization.

The singular values in the $\underline{\underline{\mathcal{S}}}$ matrix can be interpreted as a measure of the energy associated with each proper orthogonal mode. To reduce noise, only the largest singular values and the corresponding columns in $\underline{\underline{\mathcal{U}}}$ and $\underline{\underline{\mathcal{V}}}$ are retained. The r number of retained data is defined as the rank of matrix $\underline{\underline{H}}_0$. The Moore-Penrose

inverse of matrix $\underline{\underline{H}}_0$ can be expressed as

$$\underline{\underline{H}}_0^+ = \underline{\underline{\mathcal{V}}}_r \underline{\underline{\mathcal{S}}}_r^{-1} \underline{\underline{\mathcal{U}}}_r^T \tag{156}$$

while approximate $N_h m \times N_h m$ transition matrix is

$$\underline{\underline{Q}} = \underline{\underline{H}}_1 \underline{\underline{\mathcal{V}}}_r \underline{\underline{\mathcal{S}}}_r^{-1} \underline{\underline{\mathcal{U}}}_r^T \tag{157}$$

Matrix $\underline{\underline{H}}_0$ by definition will store data which is redundant. Since the rank r is typically less than the number of rows $N_h m$, only r eigenvalues of the resulting $N_h m$ eigenvalues of $\underline{\underline{Q}}$ will be physically meaningful. The remaining $N_h m - r$ eigenvalues are a function of the noise in the data within $\underline{\underline{Q}}$. Consequently, the approximate transition matrix $\underline{\underline{Q}}$ can be reshaped into the subspace defined by the r proper orthogonal modes of $\underline{\underline{H}}_0$ (in $\underline{\underline{\mathcal{U}}}_r$) to determine a reduced size $(r \times r)$ transition matrix

$$\underline{\underline{\hat{Q}}} = \underline{\underline{\mathcal{U}}}_r^T \underline{\underline{Q}} \underline{\underline{\mathcal{U}}}_r = \underline{\underline{\mathcal{U}}}_r^T \underline{\underline{H}}_1 \underline{\underline{\mathcal{V}}}_r \underline{\underline{\mathcal{S}}}_r^{-1} \tag{158}$$

The stability characteristics are then extracted from the r eigenvalues, or characteristic multipliers, of $\underline{\underline{\hat{Q}}}$ by use of eq. (155).

When eigenvalues of the transition matrix defined by eq. (158) are obtained, they will also provide the modal parameters of the system. These modal characteristics can then be used to reconstruct the original signal and ascertain the accuracy of the predictions resulting from the approximate transition matrix. The reconstructed signal $\hat{h}_s(t)$ based on the r characteristic exponents can be determined from

$$\hat{h}_s(t) = \sum_{k=1}^{r} c_{s,k}(t) e^{\lambda_k t} \tag{159}$$

where $c_{s,k}(t)$ are unknown periodic coefficients for each mode k determined by a least squares fit between the actual $(h_s(t))$ and the reconstructed $(\hat{h}_s(t))$ signals.

This PFA analysis can also be used with a Coleman transformation and moving window analysis to provide further information on the stability of the system.

5.2.2 Coleman transformation

Lyapunov [55] demonstrated that a linear system with periodic coefficients can be transformed into an equivalent time-invariant system. When dealing with periodic systems, the discrete time signals selected for the PFA must be sampled once per rotor revolution. Consequently, the system must be simulated over many rotor revolutions to obtain reliable estimates of the damping rates in an inertial frame. These samples form a heavy computational burden. The Coleman [20, 21] transformation allows the periodic system of linearized equations governing the dynamic response of isotropic helicopter rotors to be recast as a new system of equations in the rotating frame with constant coefficients known as the *Coleman inertial system equations*. A rotor is defined as isotropic if it consists of at least three blades, each blade coupling is symmetric. Although this transformation is a powerful and practical tool when applied to simple low dimensional models, it is impractical when dealing with large scale multi-physics models coupled to computational fluid dynamics codes or experimental data [82, 92].

The Coleman transformation may be applied to the original signals used for stability analysis rather than requiring a linearization of the equations of motion. In this case it becomes part of the signal post-processing procedure, known as *Coleman post-processing* (CPP), and it can completely eliminate the difficulties associated with Coleman's transformation [82, 92].

5.2.3 Moving window analysis

The approaches to stability analysis discussed earlier are temporal approaches for analyzing time-dependent signals that describe the dynamic response of a rotor. In practice, only a portion of the time series needs to be used for stability analysis corresponding to a window of size w starting at time t_s. If the signal corresponds to the response of a linear system with a single degree of freedom, it is associated with

a single frequency and damping rate. Any window of sufficient size to capture the frequency of the motion should yield the same modal parameters. If the system is nonlinear, these windows can lead to different stability parameters. For instance, if a system damping is amplitude dependent, the damping ratios extracted from different windows spanning the response to a perturbation will be different because the average signal amplitude will change. Thus, a moving window analysis can be used to obtain qualitative information about the nonlinearity of the system [82, 92].

Consider a window of size w that starts at time t_s. The PFA can then be used to estimate modal responses $\omega_k(t_s)$ and $\zeta_k(t_s)$. A new window of identical size but starting at a delayed time $t_s + \Delta t$ where Δt is the sampling rate will yield new modal responses denoted as $\omega_k(t_s + \Delta t)$ and $\zeta_k(t_s + \Delta t)$. If the PFA is applied to windows of identical size each starting at incremental time delays based on the sampling rate $i\Delta t$, it will yield modal parameters $\omega_k(t_s + i\Delta t)$ and $\zeta_k(t_s + i\Delta t)$ that are discrete functions of the *moving window* starting time. This analysis is known as the *moving window analysis* (MWA) [82, 92].

In the next sections, Partial Floquet stability analysis along with both the moving window analysis and Coleman post-processing will be applied first to the ADM (Advanced Dynamics Model) hingeless rotor at different advance ratios. The stability analysis of the ADM model is performed over simulation using DYMORE stand alone with its simplified aerodynamics, then stability analysis is done over simulation using DYMORE/OVERFLOW tight coupling solvers. The modal parameters identified by the stability analysis procedure are compared to both the available experimental data and to other comprehensive codes results. Then the stability analysis will be applied to the UH-60A (fully articulated rotor) for forward flight case 8534 using DYMORE/OVERFLOW tight coupling simulation. The ADM model is hingeless isolated rotor with very lightly damped regression lag mode with 1.05 rad/sec damping exponent (damping ratio of $\sim 2\%$). Also this rotor is rotating at very

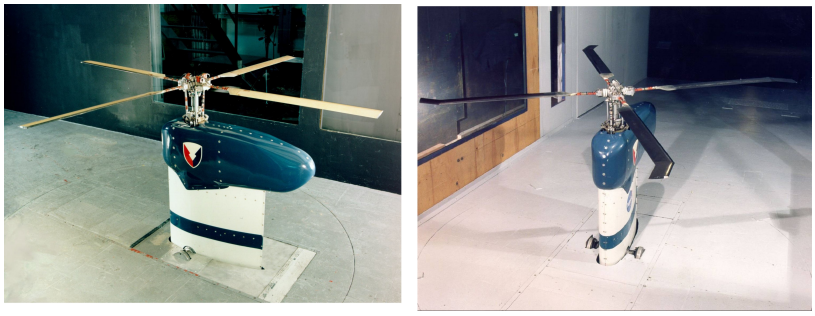

Figure 58: Straight and swept-tip models in Army/NASA 7 by 10 foot wind tunnel reference [91].

high rotational speed of 178 rad/sec. Hence its stability characteristics belongs to special category of rotors. While the UH-60A is a fully articulated rotor with both hinges and dampers, and the rotor with rotational speed of 27.02 rad/sec. All those parameters have strong effect on the type, results, and conclusions of the stability analysis methodology and the minimum length of the transient response sufficient to extract the modal parameters of each rotor.

5.3 Stability Analysis of the ADM model using DYMORE for advance ratio $\mu = 0.3$

ADM model is an isolated rotor that has four hingeless blades, and these blades are flexible in bending and torsion. Analysis on ADM investigates the regressing lag mode (RLM) aeroelastic instabilities [71]. The ADM experiments were conducted at AFDD (the US Army Aeroflight Dynamics Directorate) in the 1990s to provide a high quality aeroelastic stability database for validating aeromechanics prediction methodology for a typical hingeless rotor, with straight and swept-tip blades, operating at representative tip Mach numbers [91]. Figure 58 shows the two rotors installed in the wind tunnel on the Rotor Test Rig (RTR) [91].

DYMORE alone ADM test simulation was carried out for advanced ratio of 0.3. DYMORE with its internal aerodynamics (lifting line) was used to compute a converged trimmed solution for target airloads 240 lb, 2 lb.ft, and -2 lb.ft, for the thrust,

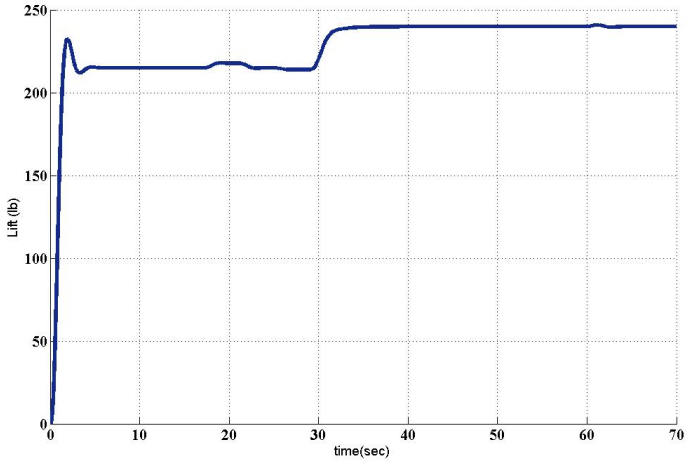

Figure 59: Lift history for the stability analysis for the ADM model.

roll and pitch moment, respectively. In reference [91], the collective angle was kept constant at 6 degrees. However, because the initial control settings corresponding to DYMORE alone ADM model for μ=0.3 were not known, the autopilot controller was used in DYMORE simulation to trim the model to the target loads; that is a total thrust of around 240 lb and almost zeros average pitch and roll moments. The resultant trimmed value of the collective control is 6.35 degrees which is very close to the constant collective angle of 6 degrees in reference [91]).

After the converged trimmed solution was reached, perturbation loads were applied to the model as described in reference [91]. Initially the model is simulated for a trimmed converged solution for 60 seconds, then periodic perturbation tip forces are applied on the four blades tips, with period 0.0117603 sec/rad, 0.25 rad phase shift, and magnitude 10 lb. The perturbation tip forces are applied for one revolution, then the ADM model is simulated for 10 seconds. In reference [91], perturbation tip forces were applied for three revolutions at the frequency of the regressing lag mode (and not at the frequency of the lag mode itself). The full time histories of the thrust, rolling and pitching moments are shown in figures 59-61. The corresponding controls time histories are shown in figures 62-64.

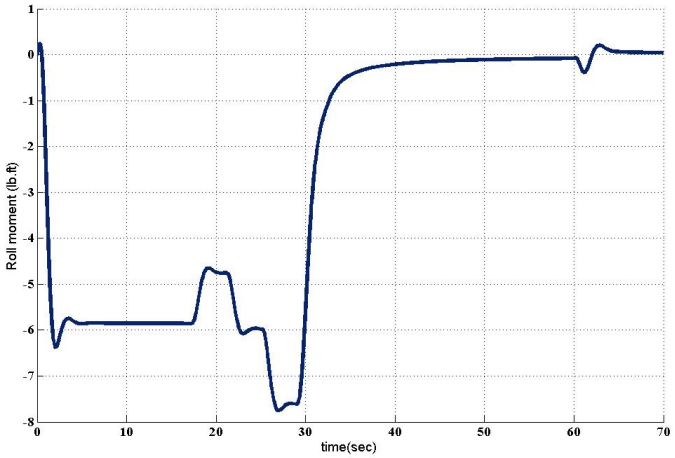

Figure 60: Roll Moment history for the stability analysis for the ADM model.

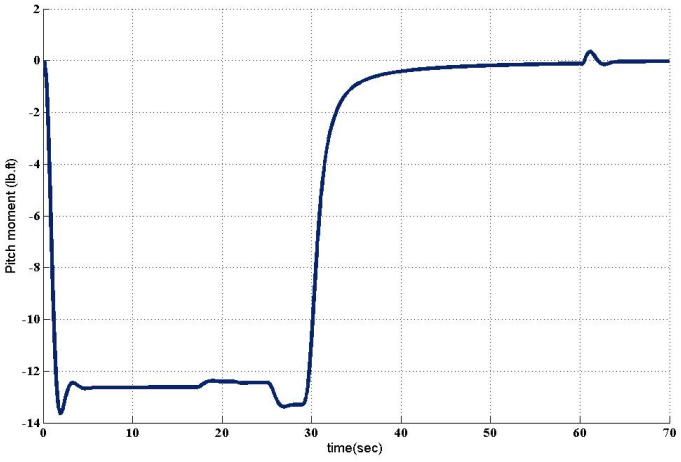

Figure 61: Pitch Moment history for the stability analysis for the ADM model.

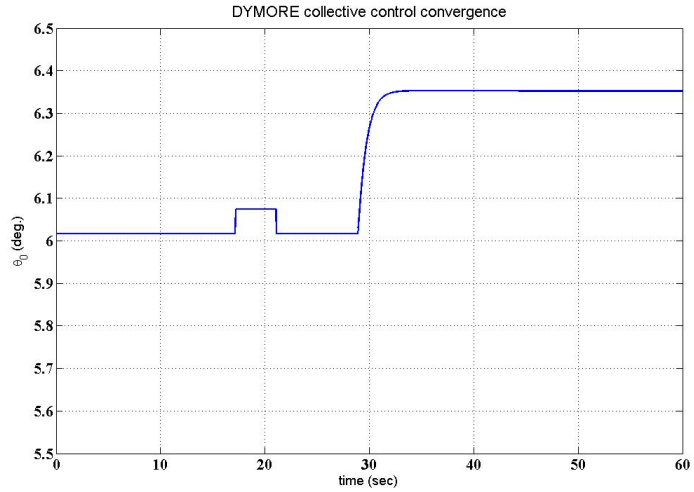

Figure 62: DYMORE run collective control convergence for the ADM model μ=0.3.

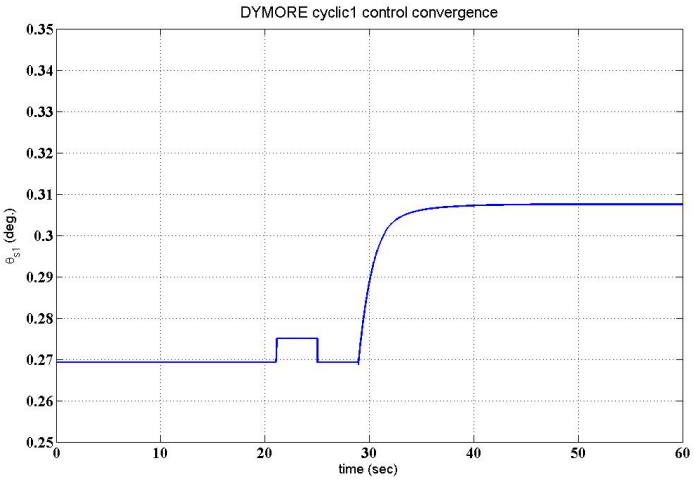

Figure 63: DYMORE run cyclic1 control convergence for the ADM model μ=0.3.

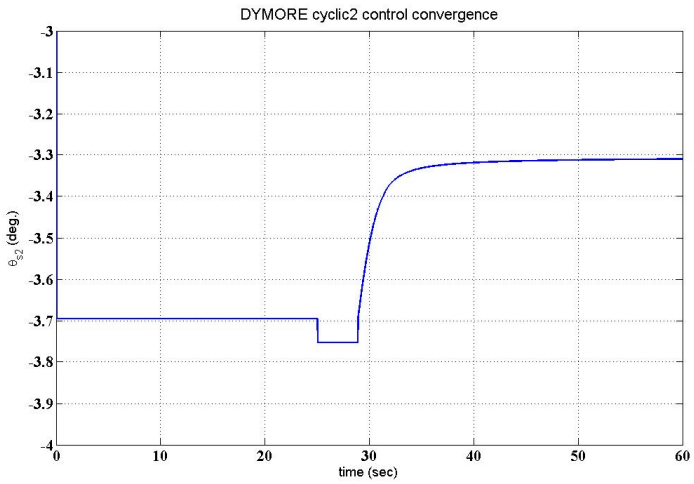

Figure 64: DYMORE run cyclic2 control convergence for the ADM model μ=0.3.

To identify the different modes of the ADM model, knowledge of their frequencies is required. According to reference [91], the ADM model's lag mode frequency is 115 rad/sec, while its experimentally determined frequency is 0.66/rev= $0.66 \times 178 \simeq 117$ rad/sec; the ADM model's regressing lag mode matches the experimentally determined frequency of $\sim$ 60 rad/sec with a damping exponent of approximately 1.05 rad/sec.

5.3.1 Stability analysis based on signals of blade 1

Stability analysis was done using PFA with rank numbers 12 and 18 after waiting for about 0.2 T of the application of the perturbation loads, where T is the system period. First stability analysis included six signals consisting from the three displacement and three rotation at the tip of first blade (blade 1). Moving window analysis was applied, with a moving window width of approximately 3.8 revolutions, on the total transient response simulation of about 25.5 revolutions. PFA with rank 12 resulted in a minimum computed frequency of 77 rad/sec with a large scatter in the damping indicating that the stability analysis might be capturing noise rather than a real mode. The next higher frequency captured, of 115 rad/sec, was that of the

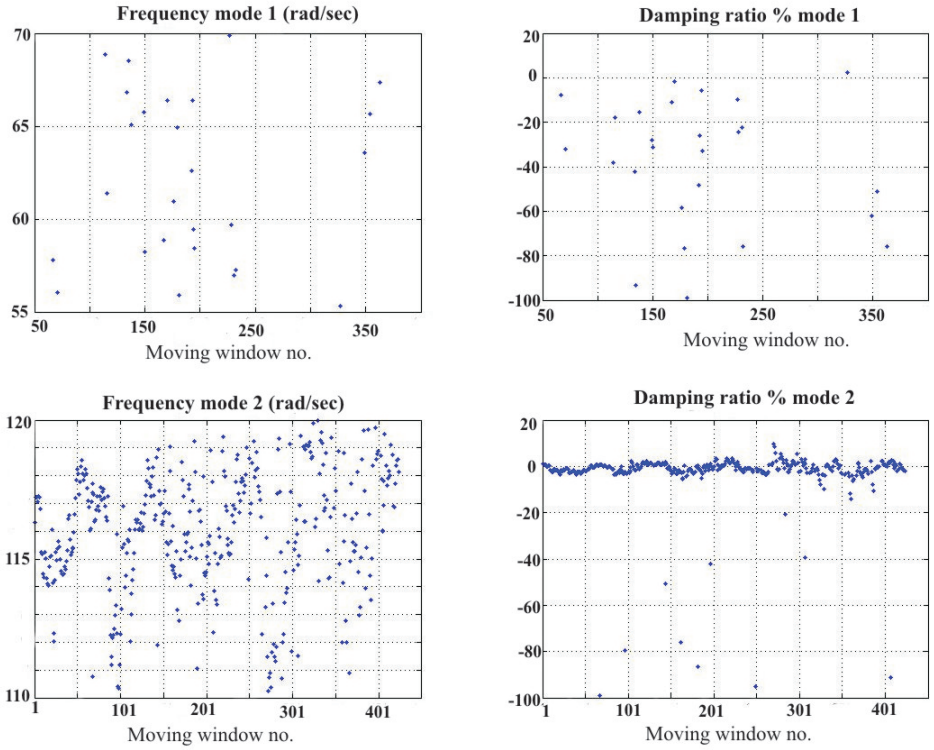

Figure 65: Moving window analysis for the ADM model using blade 1 signals using PFA rank 12.

lag mode with an average damping ratio of 1.2%. The variation of the frequency and damping for the first two modes as a function of moving window number are shown in Figure 65. In the second stability analysis, the rank number was increased to 18 and only three signals from blade 1 were used. The signals are blade 1 tip flap displacement and its lead-lag rotation and displacement, respectively. The variation of the computed frequency and damping for the first two modes as a function of moving window number are shown in Figure 66.

Using only blade 1 signals is not enough to accurately extract the modal parameters of the ADM model; the signals from the four blades should be included.

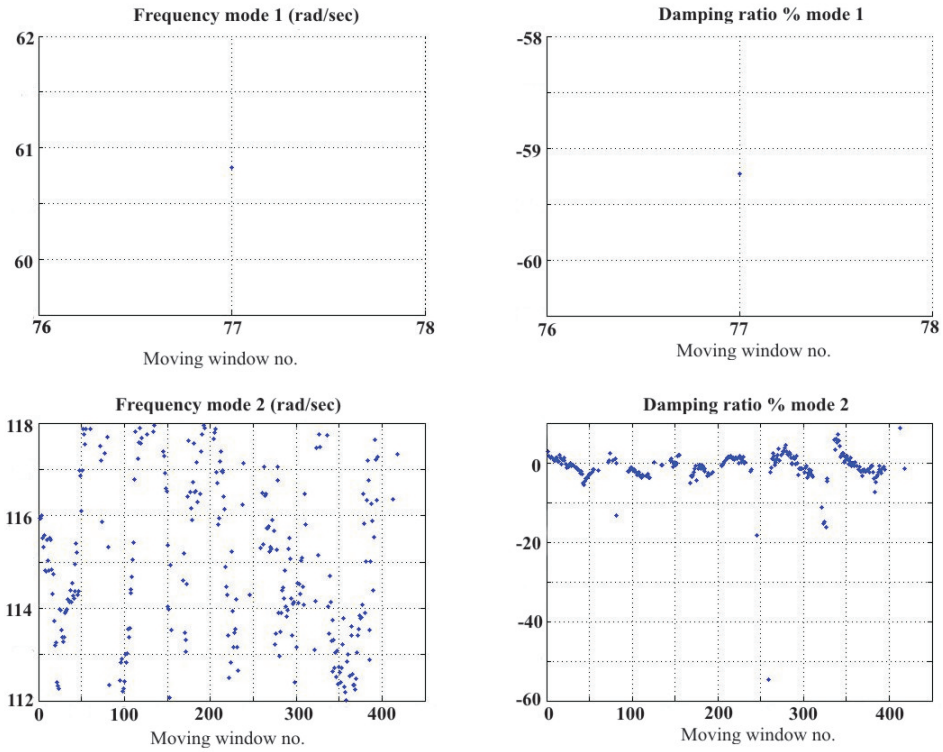

Figure 66: Moving window analysis for the ADM model using blade 1 signals using PFA rank 18.

5.3.2 Stability analysis based on 12 signals of the ADM model four blades

Since the data contained in blade 1 signals was not enough to extract the modal parameters of the rotor, another stability analysis was conducted. This stability analysis is based on the same lead-lag perturbation forces of period 0.0117603 sec/rad that represents a third of the system period, applied for one rotor revolution. Stability analysis is performed using PFA with rank 12, a moving window of width of approximately 14 revolutions and using 12 multi-blade transform signals of the four blades. The signals are the flap displacement, and the lead-lag displacement and rotation at each blade tip. The two first modes detected are at average frequencies of 62 and 115.6 rad/sec, with corresponding average damping ratios of 1.55% and 1.1%, respectively. These modes are shown in Figure 67 as a function of the moving window number. The frequency of the first detected mode is very close to that of the ADM lag mode and thus this stability analysis was unable to predict the regression lag mode frequency. The frequencies and damping ratios computed using the signals of the 4 blades show less scattering than those computed based on the signals of only blade 1 (Figures 65-66). The damping exponent is calculated from the damping ratio as follows: damping exponent = frequency $\times$ damping ratio. Hence the DYMORE damping exponent for the lag mode is equal to $62 \times 1.55\% \simeq 0.961$ rad/sec. There was no experimental data for the value of the ADM model lag mode damping exponent available in reference [91].

5.4 Stability Analysis of the ADM model using CFD/CSD Tight Coupling

In this section, the stability analysis of an isolated hingeless rotor is performed using its CFD/CSD tight coupling simulation. Stability analyses are carried out for advance ratios of $0.1 - 0.3$.

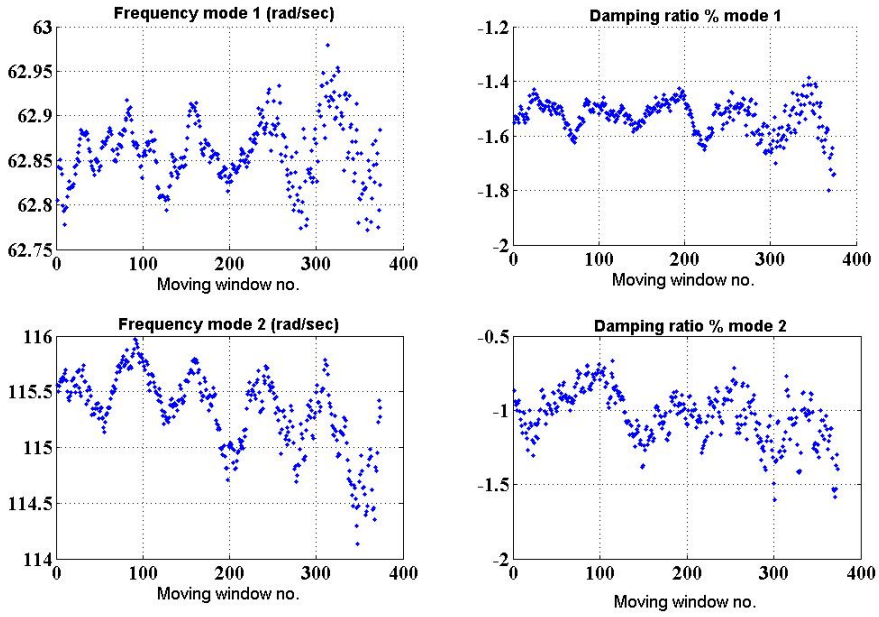

Figure 67: Moving window stability analysis results for ADM model PFA rank 12 using 12 multi-blade transform signals.

5.4.1 For advance ratio of 0.3

In this test DYMORE/OVERFLOW tight coupling was used to extract the damping of the ADM model regression lead-lag mode. CFD/CSD-coupled runs for the ADM model were performed on 32 2.4 GHz AMD Opteron processors [1]. The simulation of each CFD/CSD quarter revolution took around 2 hours. The CFD/CSD tight coupling simulation is performed as follows: Initially, DYMORE alone ADM deck was simulated for approximately 20 revolutions with control settings corresponding to 0.105019, 0.0067, and -0.0666 rad, for the collective, cyclic1, and cyclic2, respectively. The corresponding steady converged airloads are 239.367 lb of thrust, -3.129 lb.ft of pitch moment and 0.5802 lb.ft of roll moment. The resultant archival file of this DYMORE alone simulation is used as an initial condition starter for DYMORE/OVERFLOW tight coupling simulation. Tight coupling was run for 3 revolutions (0.1059 seconds). After a steady periodic solution is reached under tight

[1] See Acknowledgments.

coupling perturbed loads, as described in the previous section, were applied on the blades tips of the model for one whole revolution (0.0353 seconds). After the perturbation loads were removed, the ADM tight coupling simulation was run for 19 revolutions (0.6706 seconds). Plots of the tight coupling total airloads coefficients' histories are shown in Figures 68-70. Figures 68-70 show that the applied perturbation loads did not cause large transient loads on the rotor. The maximum change in the thrust coefficient was around 12% during the application of the perturbation loads.

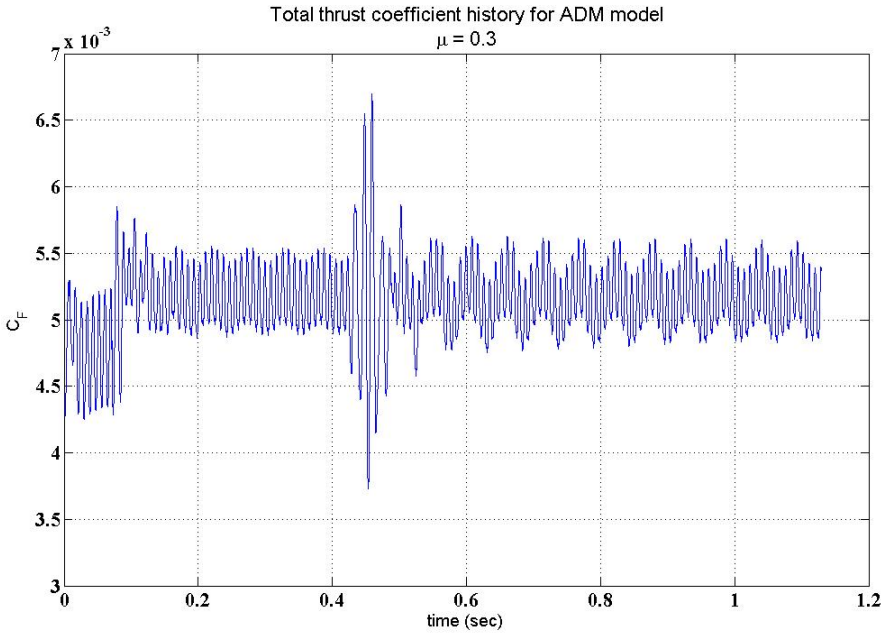

Figure 68: ADM tight coupling thrust coefficient history for $\mu = 0.3$.

Next, different sets of stability analysis were carried out using Partial Floquet analysis with several sets of signals and rank numbers. The analysis was performed on the whole available 18.8 revolutions tight coupling data (after waiting 0.2 T seconds after the application of the perturbation loads), as described next.

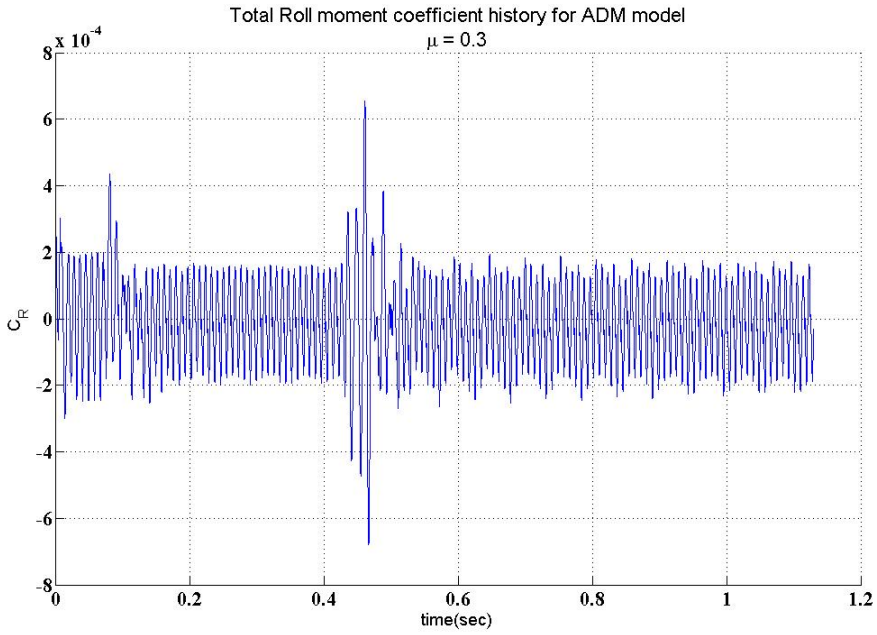

Figure 69: ADM tight coupling roll moment coefficient history for $\mu = 0.3$.

5.4.1.1 ***ADM stability analysis results using standard signals and multi-blade transform signals***

Two stability analysis of the ADM model were performed using the same set of signals from the 4 blades, once in their standard form and once in their multi-blade transform form. Both stability analyses are performed using Partial Floquet analysis and same rank numbers. For rank 12, the analysis were performed using 4 signals from each of the 4 blades: the flap and lead-lag displacements and the lead-lag rotation at each blade tip with respect to the rotating moving frame. The first stability analysis, called stability analysis 1, used the standard preconditioned signals. The accuracy of the computed mode's damping and frequency could be determined by comparing the original signals to the reconstructed ones as shown in Figures 71-73. In these figures, the signals are plotted versus normalized time range of $0 - 0.66$ seconds, representing a total of 18.8 revolutions transient response. Figures 71-73 show good agreement between the original and the reconstructed signals.

The minimum frequency detected by stability analysis 1 is equal to 116.258 rad/sec,

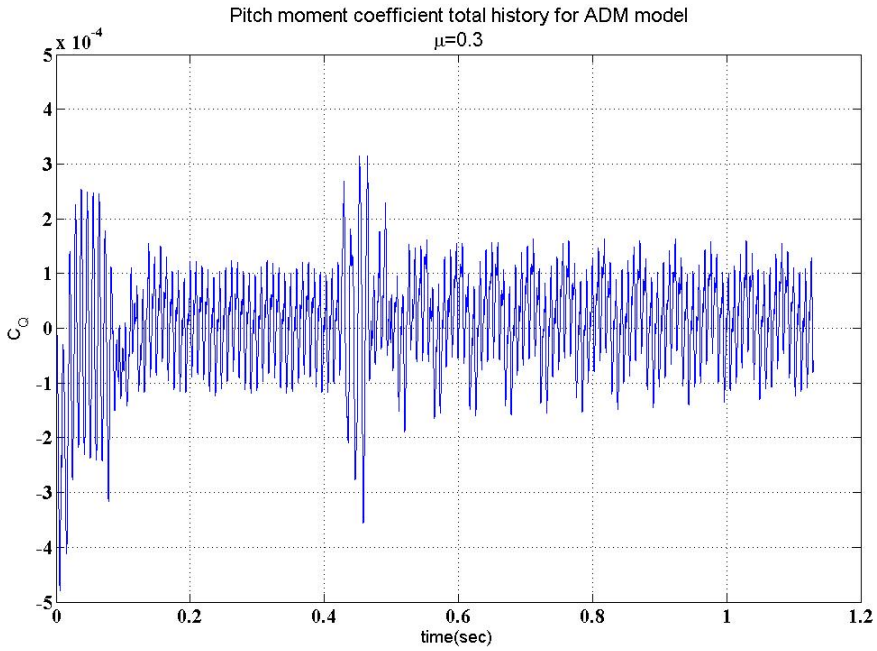

Figure 70: ADM tight coupling pitch moment coefficient history for $\mu = 0.3$.

which is the lag mode frequency, while the regression lag mode frequency was not detected.

The second stability analysis, called stability analysis 2, used the 12 Coleman post-processing multi-blade transform signals obtained from applying the Coleman post-processing transform on the same 12 standard signals used in stability analysis 1. The comparison of the original and the reconstructed signals of stability analysis 2 using PFA with rank 12 are shown in Figures 74-76. In these figures, the multi-blade transform signals are plotted versus normalized time range $0 - 0.663$ seconds, representing a total of 18.8 revolutions transient response.

It is clear that using the Coleman post-processing multi-blade transform signals in stability analysis 2 resulted in less accurate damping and frequency computations as shown in Figures 74-76. The difference between the original and the reconstructed signals are in both the amplitude and the oscillations, indicating that the Stability Analysis 2 computation for both the damping and the frequency, respectively, is not accurate enough to reconstruct the original signals. The Coleman post-processing

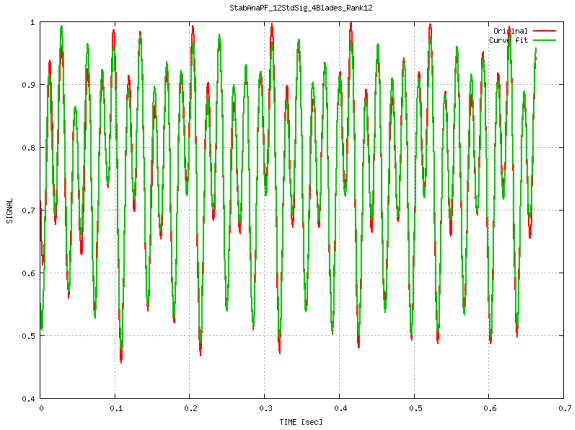

(a) Standard signal blade 1 tip displacement flap motion.

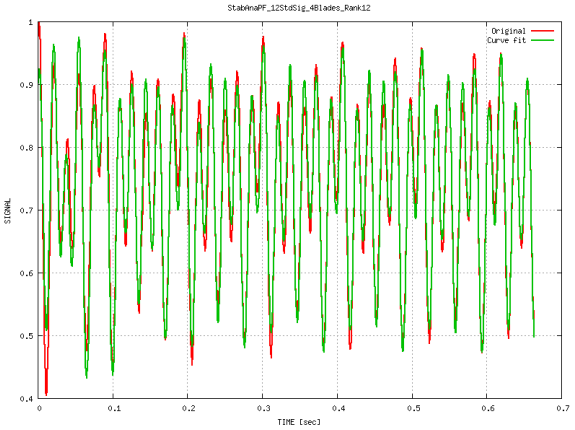

(b) Standard signal blade 2 tip displacement flap motion.

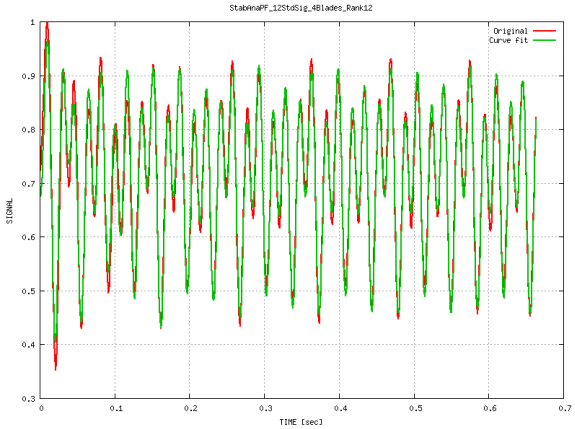

(c) Standard signal blade 3 tip displacement flap motion.

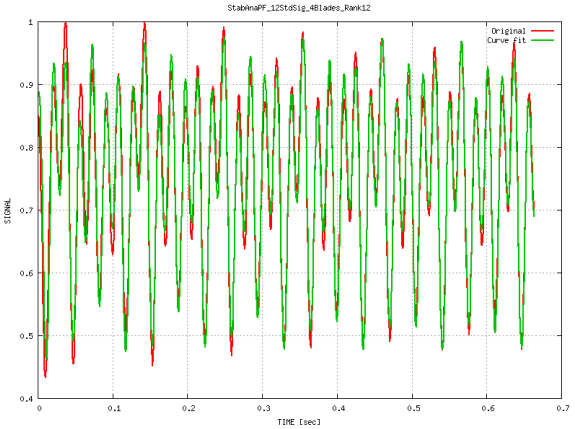

(d) Standard signal blade 4 tip displacement flap motion.

Figure 71: Comparing the original flap displacements signals to the reconstructed signals for ADM model stability analysis 1 PFA rank 12.

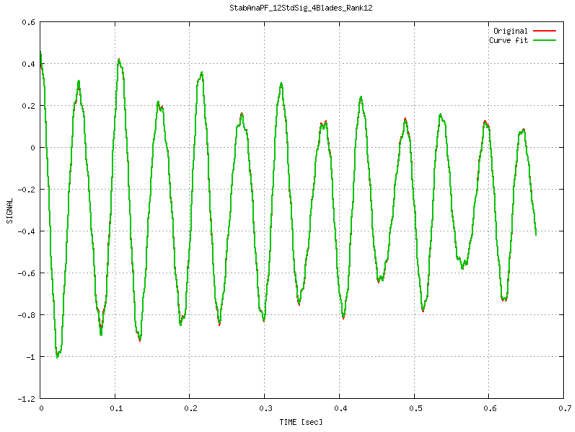

(a) Standard signal blade 1 tip displacement lead-lag motion.

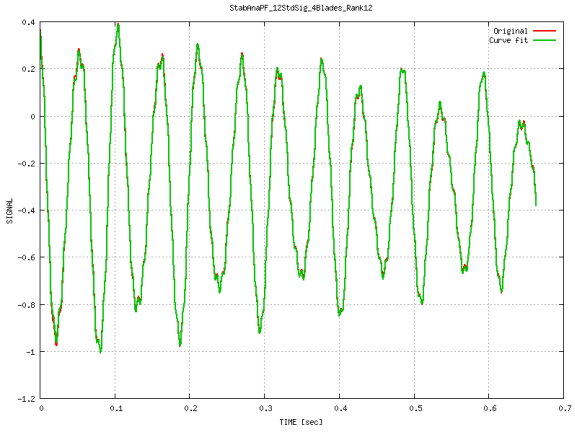

(b) Standard signal blade 2 tip displacement lead-lag motion.

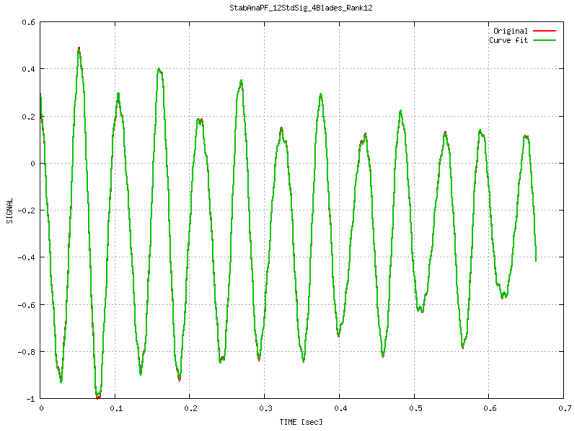

(c) Standard signal blade 3 tip displacement lead-lag motion.

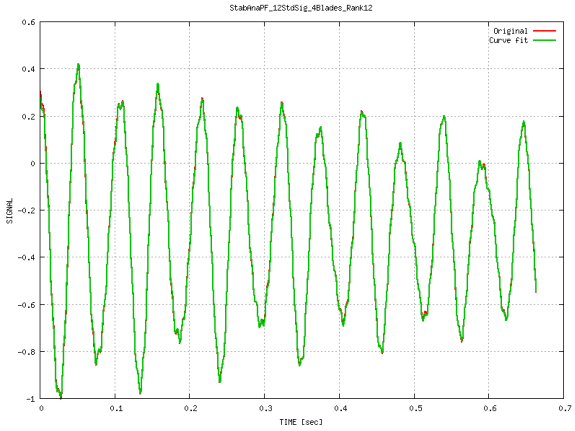

(d) Standard signal blade 4 tip displacement lead-lag motion.

Figure 72: Comparing the original lead-lag displacements signals to the reconstructed signals for ADM model stability analysis 1 PFA rank 12.

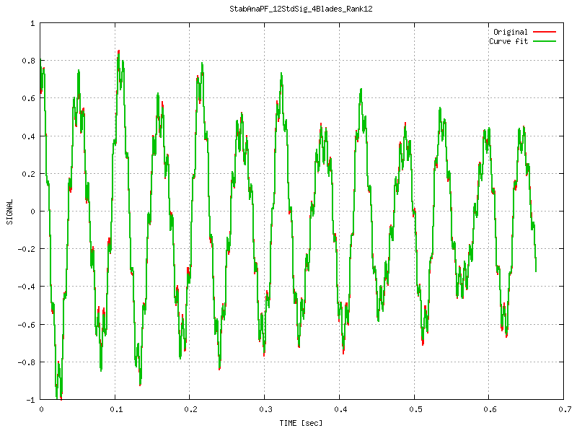

(a) Standard signal blade 1 tip lead-lag rotation.

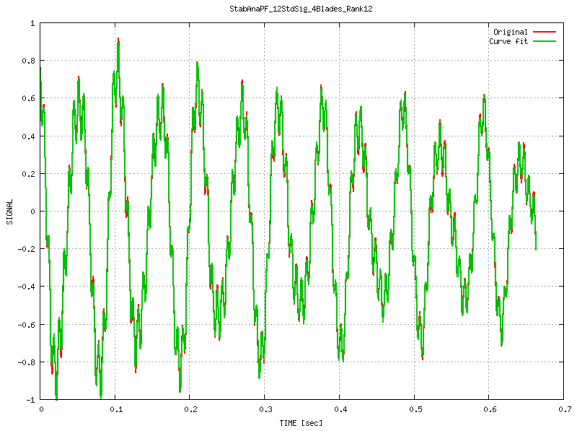

(b) Standard signal blade 2 tip lead-lag rotation.

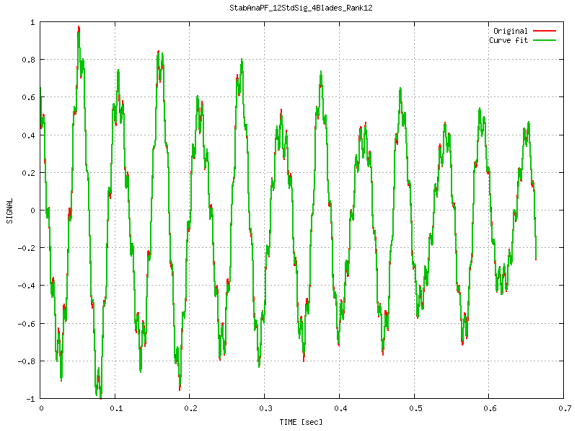

(c) Standard signal blade 3 tip lead-lag rotation.

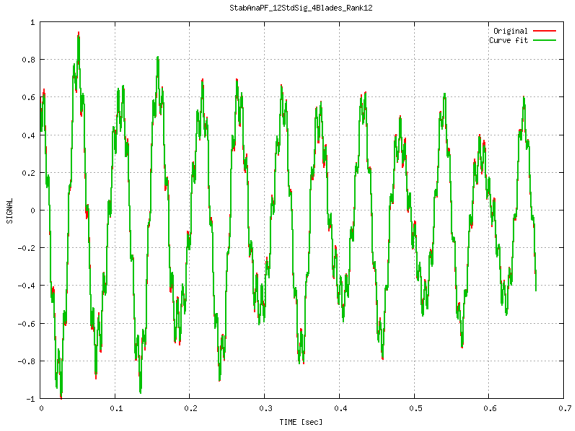

(d) Standard signal blade 4 tip lead-lag rotation.

Figure 73: Comparing the original lead-lag displacements signals to the reconstructed signals for ADM model stability analysis 1 PFA rank 12.

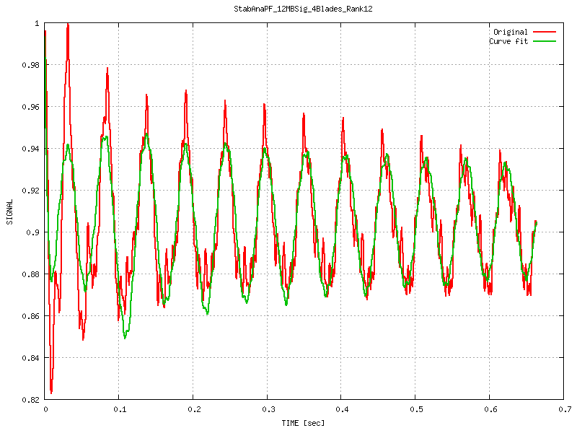

(a) Multi-blade transform signal 1.

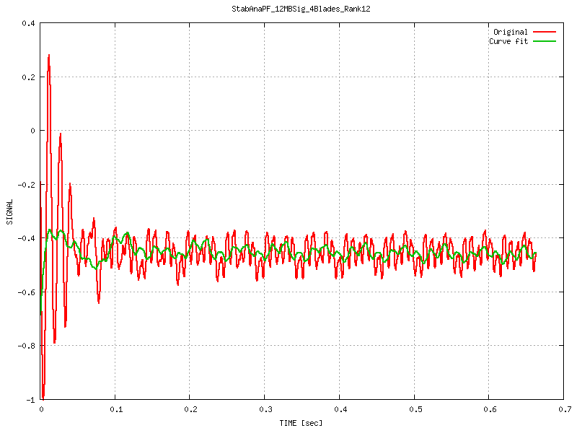

(b) Multi-blade transform signal 2.

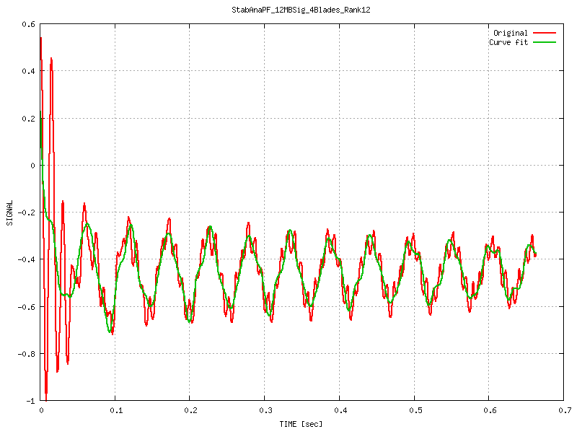

(c) Multi-blade transform signal 3.

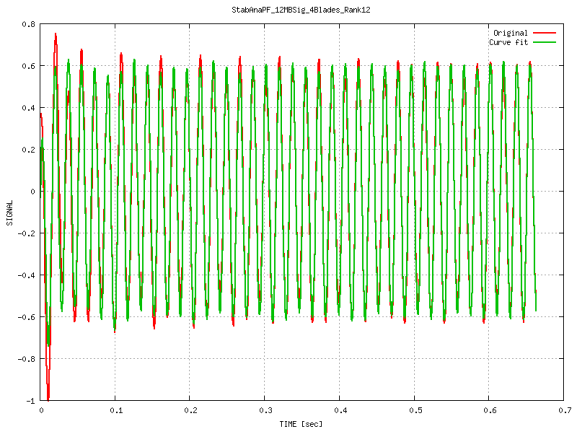

(d) Multi-blade transform signal 4.

Figure 74: Comparing the original 1-4 signals to the reconstructed signals for ADM model stability analysis 2 PFA rank 12.

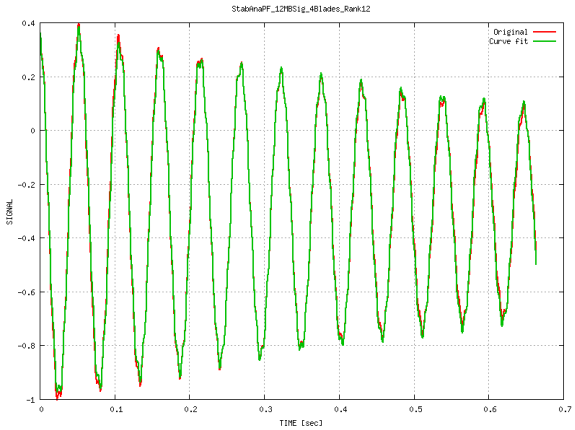

(a) Multi-blade transform signal 5.

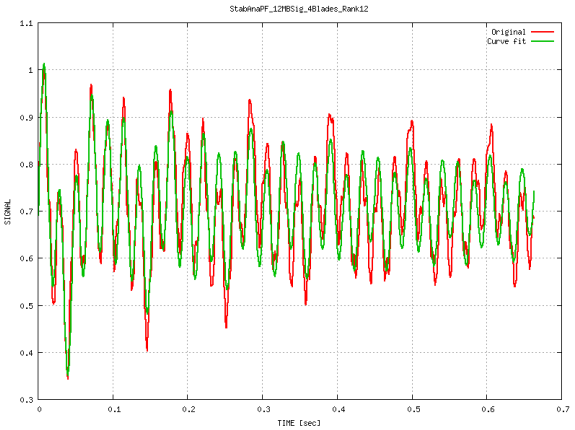

(b) Multi-blade transform signal 6.

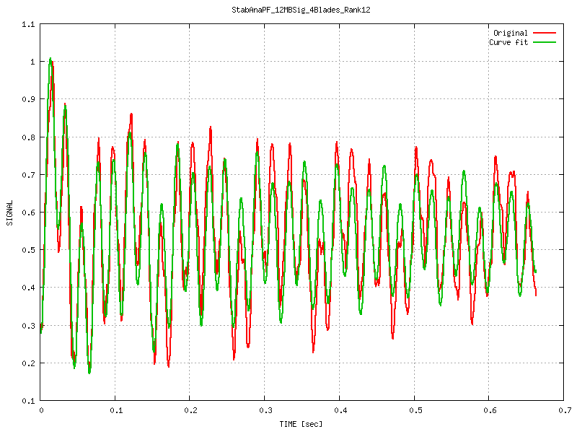

(c) Multi-blade transform signal 7.

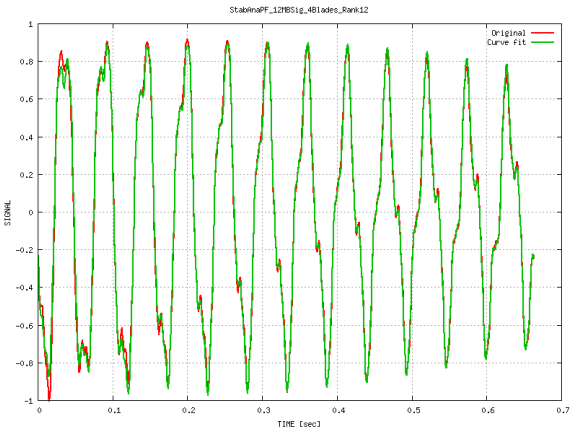

(d) Multi-blade transform signal 8.

Figure 75: Comparing the original 5-8 signals to the reconstructed signals for ADM model stability analysis 2 PFA rank 12.

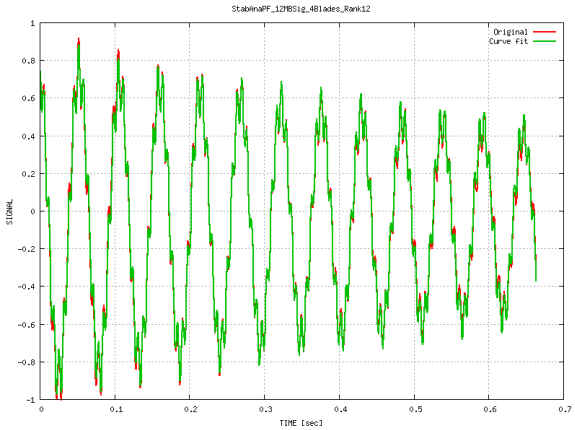

(a) Multi-blade transform signal 9.

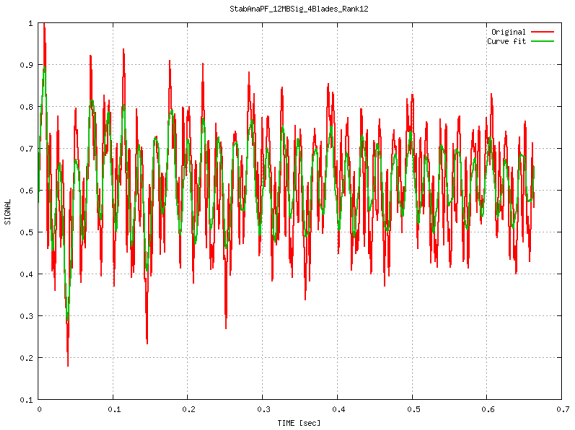

(b) Multi-blade transform signal 10.

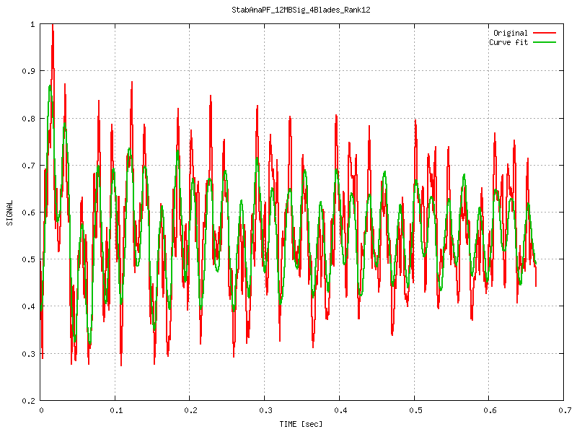

(c) Multi-blade transform signal 11.

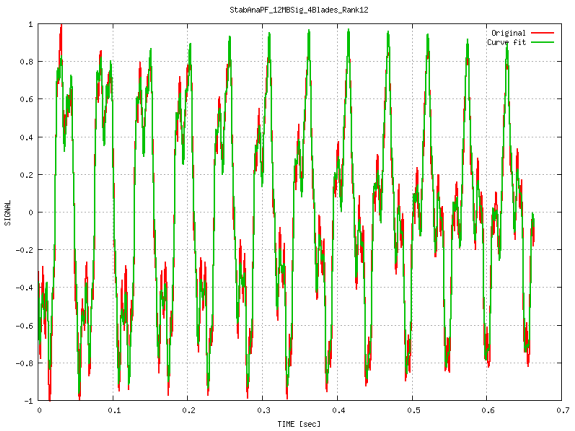

(d) Multi-blade transform signal 12.

Figure 76: Comparing the original 9-12 signals to the reconstructed signals for ADM model stability analysis 2 PFA rank 12.

transform should be applied to strictly periodic signals. Since the signals are still in their free decay phase after removing the perturbed loads, especially the lightly damped modes like the lead-lag mode, the Coleman post-processing should be applied after waiting for this transient response to decrease. However, in the same duration, the highly damped modes die out quickly and cannot be detected in the signals after a while. A special care should thus be taken in adjusting the waiting time to begin the application of the Coleman post-processing transform.

In the current study, different starting points were tested to apply the Coleman post-processing transform and they all ended up with similar results, namely, poor signal reconstruction indicating that the computed modal parameters were not accurate enough. This might be due to a need to increase the number of points per revolution included in the stability analysis along with the rank number required for this high rotational speed test case, which increases the size of the transition matrix leading to an increase in the numerical noise content in the stability analysis solution. More investigation is required to identify the exact reasons and the proposed solutions in the case of applying the Coleman post-processing transform to the signals from helicopter rotors characterized by large rotational speed.

Finally, stability analysis 1 that used the 12 standard signals of the 4 blades was repeated with rank 18. Increasing the rank number for stability analysis 1 led to the detection of the regression lag mode, as shown in table 18. However, results in table 18 show that the computed damping exponent of the regression lag mode by DYMORE/OVERFLOW using Partial Floquet Analysis is largely different from their experimental counterparts and the damping exponent computed by RCAS/OVERFLOW using the moving block analysis. To ascertain the accuracy of the computed frequencies and damping ratios by DYMORE/OVERFLOW PFA, signal reconstruction was performed. The signal reconstruction is shown in Figures 77-79. In these figures the signals are plotted versus normalized time range $0 - 0.663$

seconds, representing 18.8 revolutions of transient response.

The stability analysis signal reconstruction assesses the accuracy of the computed modal parameters. This means that the very small damping exponent computed by DYMORE/OVERFLOW captures the signal content and not numerical noise. Hence, more stability analyses have been performed in attempt to identify the reasons for the difference in the computed damping exponent between DYMORE/OVERFLOW and RCAS/OVERFLOW. The results of this test are shown in table 17 where the symbol '–' is used to indicate that the stability analysis was unable to predict the regression lead-lag mode. It was found that waiting for 4 to 8 revolutions for the transient response to decrease and performing the stability analysis was not sufficient and the regression lag mode frequency was not detected. However, applying the stability analysis on the signals after three revolutions was able to detect the regression lag mode with the damping exponent 46% different from its experimental value. This difference decreases to 41% when stability analysis was performed on the signals after waiting two revolutions as shown in table 17. When the stability analysis was performed after only one revolution of the application of the perturbation loads, the computed damping exponent was 29.3% different from its experimental value. Since the signals were reconstructed well from the computed modal parameters, the obtained damping values and frequencies represent the actual signals contents. Hence, the regression lag mode computed damping exponent dramatic change from 0.74 rad/sec to 1.54 rad/sec between the windows $1-18$ (0.0353-0.663 seconds) revolutions and $3-18$ revolutions (0.1059-0.663 seconds) is mostly due to the existence of system nonlinearity.

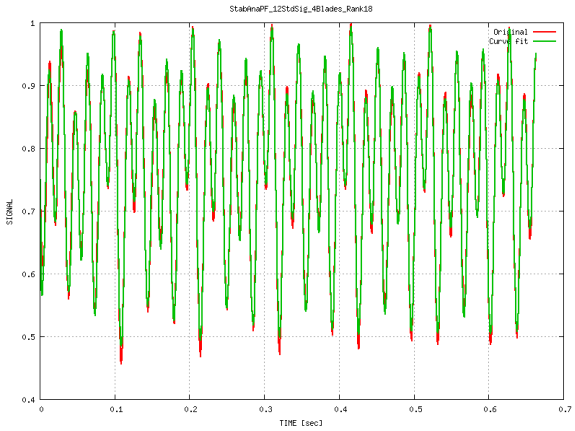

(a) Signal reconstruction blade 1 tip displacement flap motion $\mu = 0.3$.

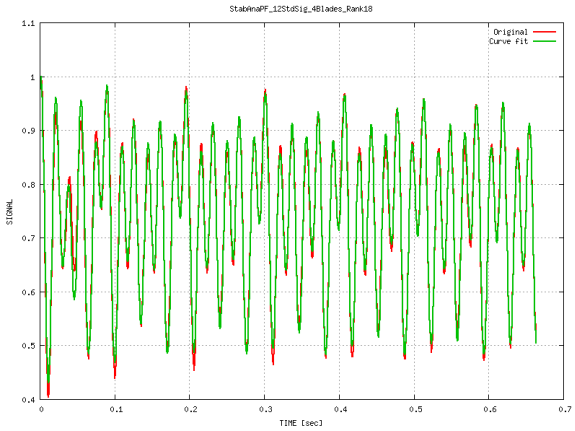

(b) Signal reconstruction blade 2 tip displacement flap motion $\mu = 0.3$.

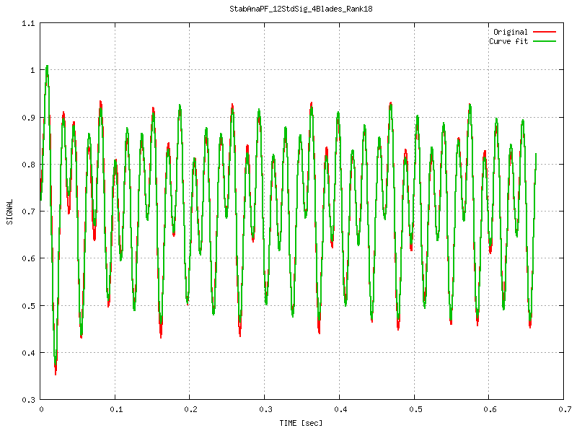

(c) Signal reconstruction blade 3 tip displacement flap motion $\mu = 0.3$.

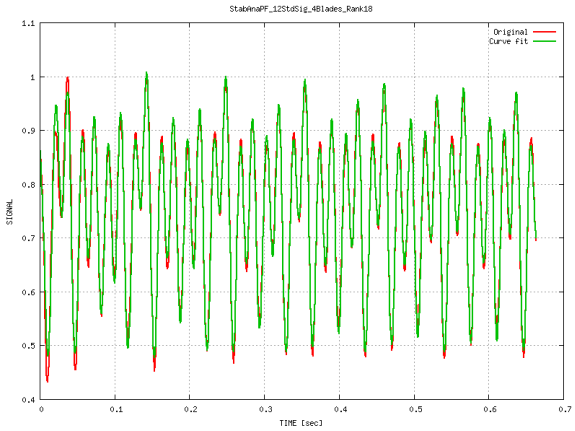

(d) Signal reconstruction blade 4 tip displacement flap motion $\mu = 0.3$.

Figure 77: Blades tip flap displacement signal reconstruction for $\mu = 0.3$ PFA rank 18.

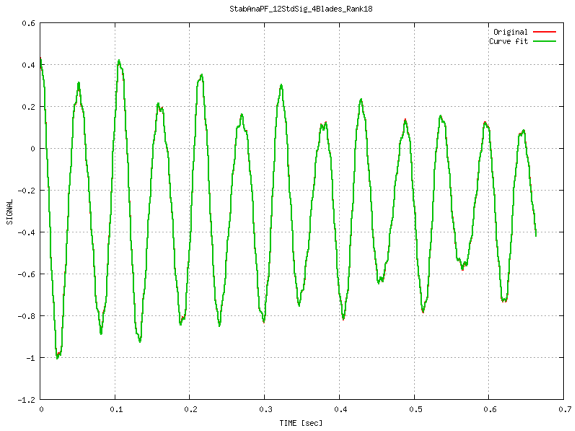

(a) Signal reconstruction blade 1 tip displacement lead-lag motion $\mu = 0.3$.

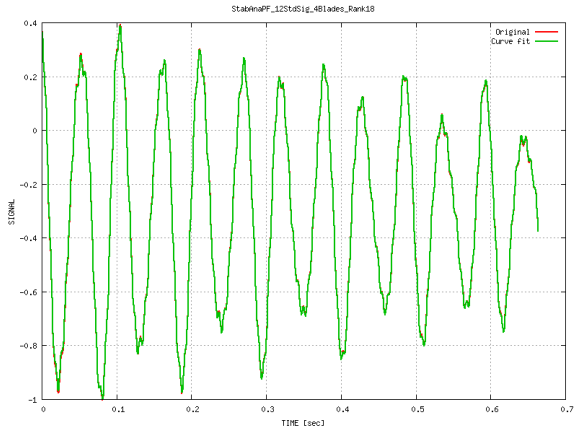

(b) Signal reconstruction blade 2 tip displacement lead-lag motion $\mu = 0.3$.

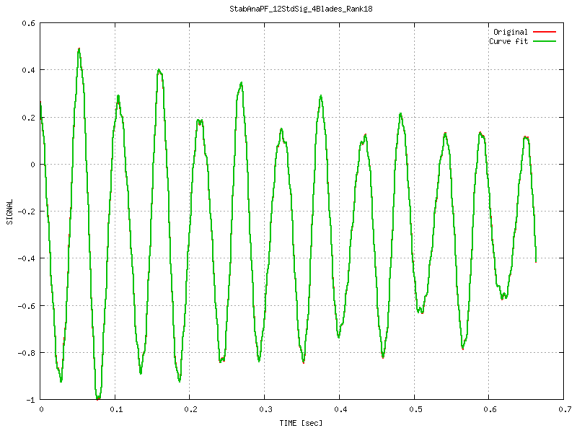

(c) Signal reconstruction blade 3 tip displacement lead-lag motion $\mu = 0.3$.

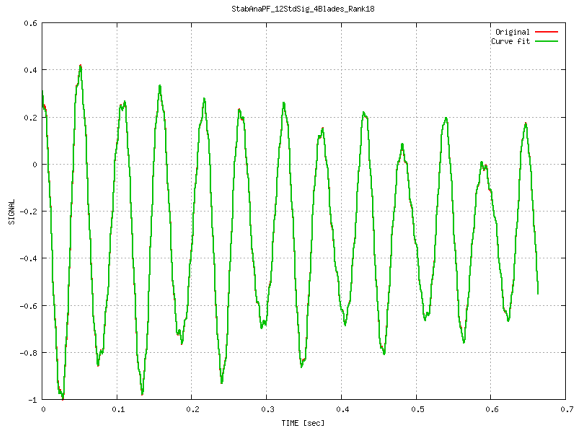

(d) Signal reconstruction blade 4 tip displacement lead-lag motion $\mu = 0.3$.

Figure 78: Blades tip lead-lag displacement signal reconstruction for $\mu = 0.3$ PFA rank 18.

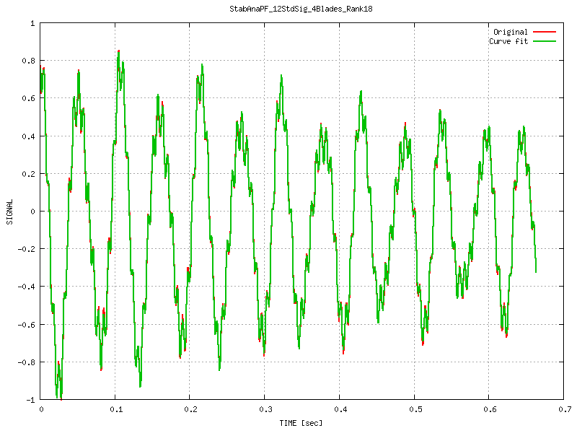

(a) Signal reconstruction blade 1 tip displacement lead-lag rotation $\mu = 0.3$.

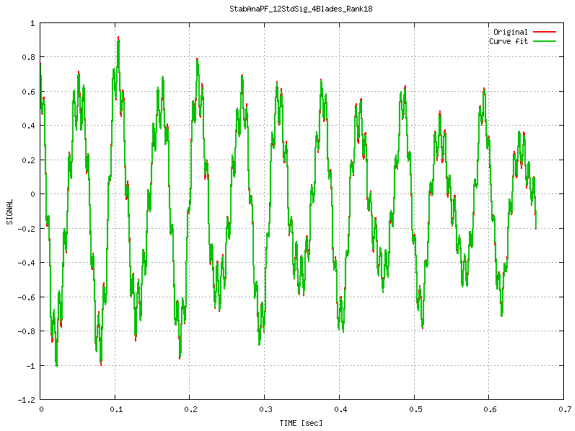

(b) Signal reconstruction blade 2 tip displacement lead-lag rotation $\mu = 0.3$.

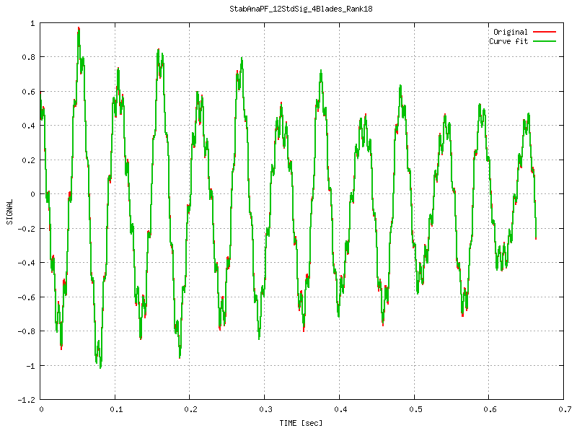

(c) Signal reconstruction blade 3 tip displacement lead-lag rotation $\mu = 0.3$.

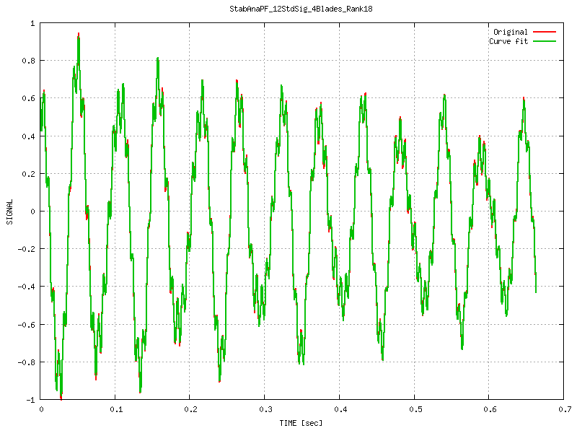

(d) Signal reconstruction blade 4 tip displacement lead-lag rotation $\mu = 0.3$.

Figure 79: Blades tip lead-lag rotation signal reconstruction for $\mu = 0.3$ PFA rank 18.

Table 17: Regression ADM lead-lag mode characteristics for $\mu = 0.3$, PFA rank 18.

Signals window	4-18	3-18 revs	2-18 revs	1-18 revs
Frequency (rad/sec)	–	62.969	62.53	62.423
Damping ratio (%)	–	2.404	2.3732	1.1886
Damping exponent (rad/sec)	–	1.514	1.484	0.742
Experimental damping exponent	1.05 (rad/sec)			
% Difference		44.19%	41.3%	-29.33%

5.4.2 For advance ratios of 0.1 and 0.2

The test was run for the ADM model with advance ratios of 0.1 and 0.2 [2]. Initially DYMORE/OVERFLOW loose coupling iterations were performed to obtain a converged trimmed solution, then the archival file of the last loose coupling iteration, for each advance ratio, was used as initial condition for the tight coupling simulation. Once the tight coupling begins, it is allowed to run for 0.1059 seconds (3 revolutions). After the periodic steady state is reached, lateral cyclic lead-lag perturbation loads were applied as described for the previous advance ratio $\mu = 0.3$ run. The simulation is allowed to run for 1.0564 seconds (30 revolutions) after the application of the perturbation loads. Total loads coefficients' histories for $\mu = 0.1$ are shown in Figures 80-82, and for $\mu = 0.2$ in Figures 83-85. These figures show the total tight coupling loads history for 48.4 revolutions.

The final comparison of DYMORE/OVERFLOW and RCAS/OVERFLOW results are shown in table 18. Tests for advance ratio of 0.1 were conducted on transient response of duration 17 revolutions. For advance ratio of 0.2, signal of duration 8 revolutions were initially used for testing. DYMORE/OVERFLOW computed damping exponent for $\mu = 0.1$ which differs from the experimental value by about 25%. For $\mu = 0.2$, DYMORE/OVERFLOW over-predicted the damping exponent dramatically, when only 8 revolutions of the transient data were used, with a 140% difference.

[2] See Acknowledgments.

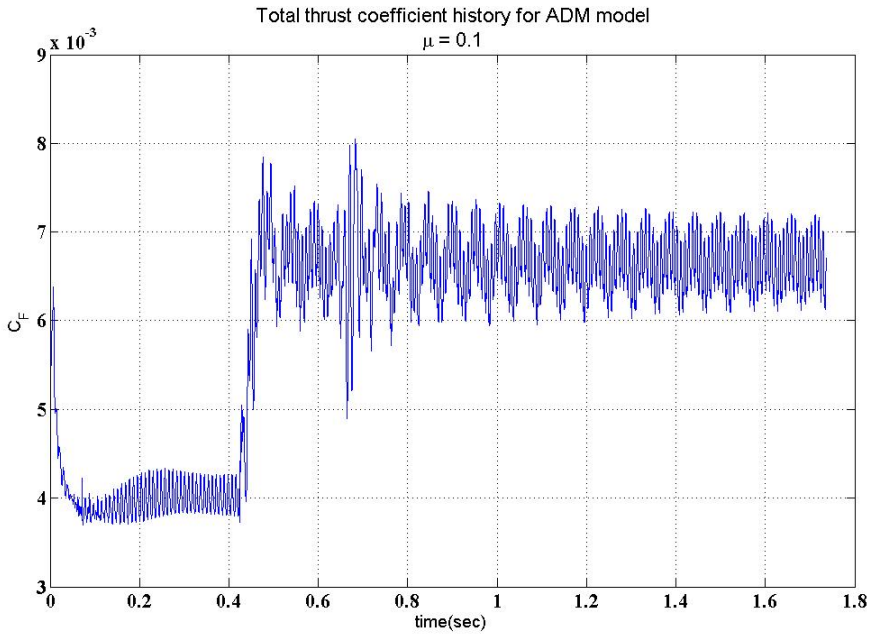

Figure 80: ADM thrust coefficient history for $\mu = 0.1$.

However, prediction was close to experimental results when the overall 30 revolutions of the simulated transient response were used (table 19). All stability analyses were conducted based on 12 standard signal from the 4 blades, using PFA with rank 18. To ascertain the accuracy of the computed frequencies and damping ratios by DYMORE PFA, signal reconstruction was performed. The signal reconstruction of the stability analysis for advance ratio $\mu = 0.2$ based on 8 revolutions are shown in Figures 86-88. In these figures the signals are plotted versus normalized time range $0 - 0.2824$ seconds representing the first 8 revolutions of the transient response.

To further investigate the cause of differences in the computed damping exponents between DYMORE/OVERFLOW and RCAS/OVERFLOW, several stability analyses were performed for $\mu = 0.2$ advance ratio. The results for these tests are shown in tables 19-20, where 'revs' is used to denote 'revolutions'. For $\mu = 0.2$, it is clear that the computed damping exponent extracted from the first 8 revolutions (0.2824 seconds) of the transient response was very high with a 104.67% difference from the experimental value and then decreased with the mode amplitude of excitation. Hence

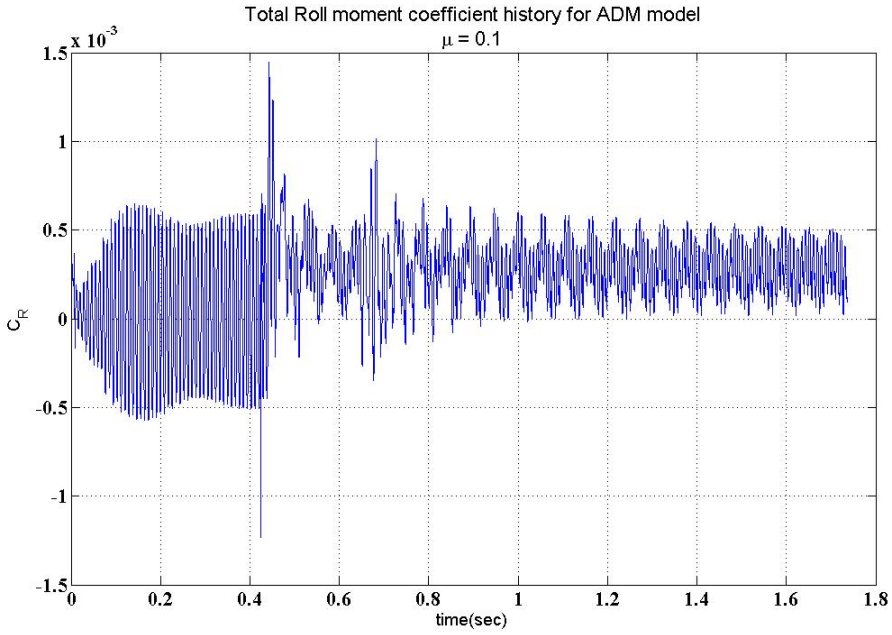

Figure 81: ADM roll moment coefficient history for $\mu = 0.1$.

the calculated damping exponent based on the last 22 revolutions (0.776 seconds) of the transient response was smaller than the damping exponent calculated from the first 8 revolutions and reached difference of 9.43% from the experimental value. As a result, the computed damping exponent based on the total 30 revolutions (1.0564 seconds) was eventually an averaged value of that of the first 8 revolutions (0-0.2824 seconds) and that of the last 22 revolutions (0.2824-1.0564 seconds), with only 0.833% difference from the experimental value. The observed damping exponent values of the regression lead-lag mode are a natural response of the system to the excitation loads as a function of its amplitude. The detailed stability analysis results for $\mu = 0.2$ are shown in table 19.

This observation was further proved by dividing the whole simulation of 30 revolutions (1.0564 seconds) to sequence of signals of length 8 revolutions (0.2824 seconds) approximately and performing on each part of the transient response the same PFA with rank 18. Results for this test are shown in table 20. Again, the change of the damping exponent with the stability analysis window is clear. The percentage

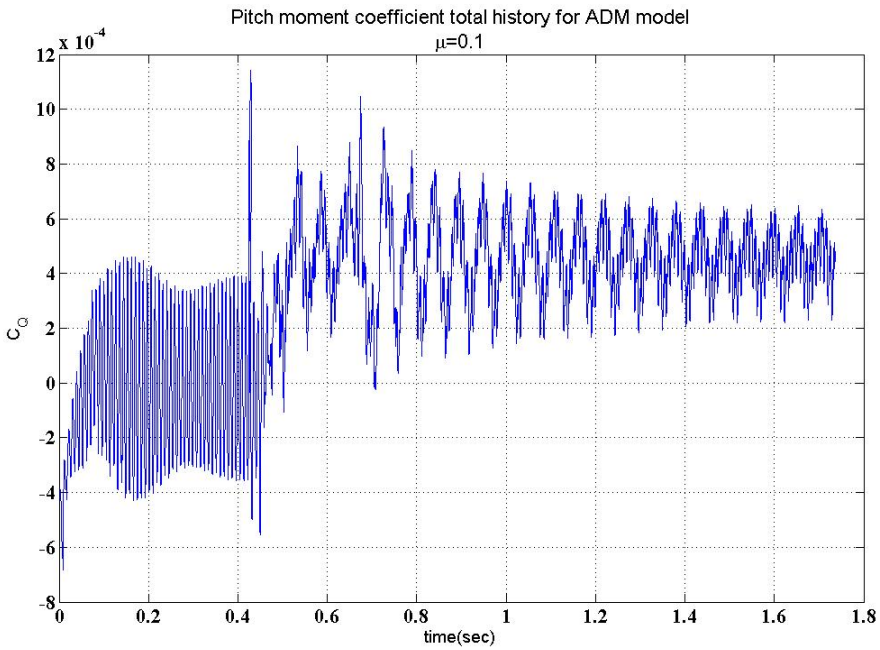

Figure 82: ADM pitch moment coefficient history for $\mu = 0.1$.

difference of the computed damping exponent compared to its experimental counterpart changes from 104.6% based on the first 8 revolutions of the transient response to -3.9% based on the 9-16 revolutions (0.2824-0.5648 seconds) of the transient response, and finally reached -11.28% based on the last 8 revolutions (0.774-1.0564 seconds) of the transient response simulation.

Table 18: Comparing the computed regression ADM lead-lag mode damping exponent (rad/sec) for several advance ratios.

Advance ratio	RCAS/ OVERFLOW Reference [91]	DYMORE/ OVERFLOW	Experimental test	% Difference columns 2-3
0.1	1.2	1.3117	1.05	24.9%
0.2	1.25	2.45	1.2	140%
0.3	1.2	0.742	1.05	-29.33%

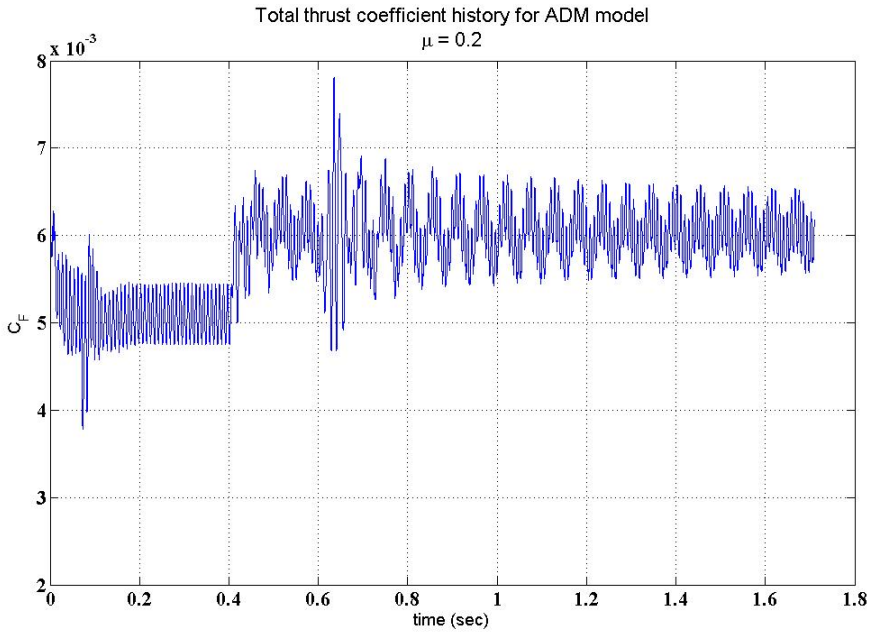

Figure 83: ADM thrust coefficient history for $\mu = 0.2$.

Table 19: Regression ADM lead-lag mode characteristics for $\mu = 0.2$, PFA rank 18.

Signals window	1-8 revs	8-30 revs	1-30 revs
Frequency (rad/sec)	66.322	61.95	62.21
Damping ratio (%)	3.7029	1.754	1.9129
Damping exponent (rad/sec)	2.456	1.0868	1.19
Experimental damping exponent [91]		1.2 (rad/sec)	
% Difference	104.67%	-9.43%	-0.833%

5.4.3 Discussion of the analysis

DYMORE/OVERFLOW tight coupling simulation was carried out for the hingeless rotor ADM model for several advance ratios. Stability analysis was undertaken using Partial Floquet approach along with the moving window analysis and Coleman post-processing analysis. Several stability analysis sets were performed on different windows of the transient response. Results showed that the computed damping exponents for the ADM regression lag mode were changing with the window of the signals used, and nonlinear behavior was observed in the computed regression lag damping

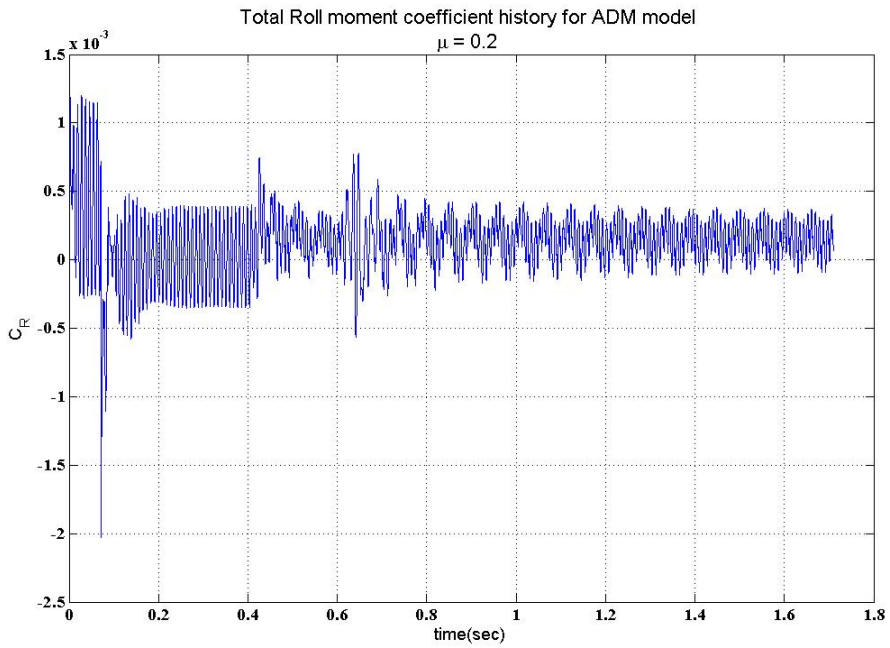

Figure 84: ADM roll moment coefficient history for $\mu = 0.2$.

Table 20: Regression ADM lead-lag mode characteristics for $\mu = 0.2$, PFA rank 18, signal length 8 revolutions.

Signals window	1-8 revs	9-16 revs	17-24 revs
Frequency (rad/sec)	66.322	61.773	61.9604
Damping ratio (%)	3.7029	1.866	1.718
Damping exponent (rad/sec)	2.456	1.1532	1.0646
Experimental damping exponent [91]	1.2 (rad/sec)		
% Difference	104.6%	-3.9%	-11.28%

exponents. This led to DYMORE/OVERFLOW with PFA requiring longer signals (30 revolutions) to predict damping exponents closer to their averaged experimental results than RCAS/OVERFLOW using the moving block analysis (used only 10 revolutions) (table 19). The longer signals led to the averaging of the non linear response observed.

Using Coleman post-processing multi-blade signals resulted in less accurate stability analysis compared to using the standard signals. Potential reason might be the need to increase the number of points per revolution included in the stability analysis

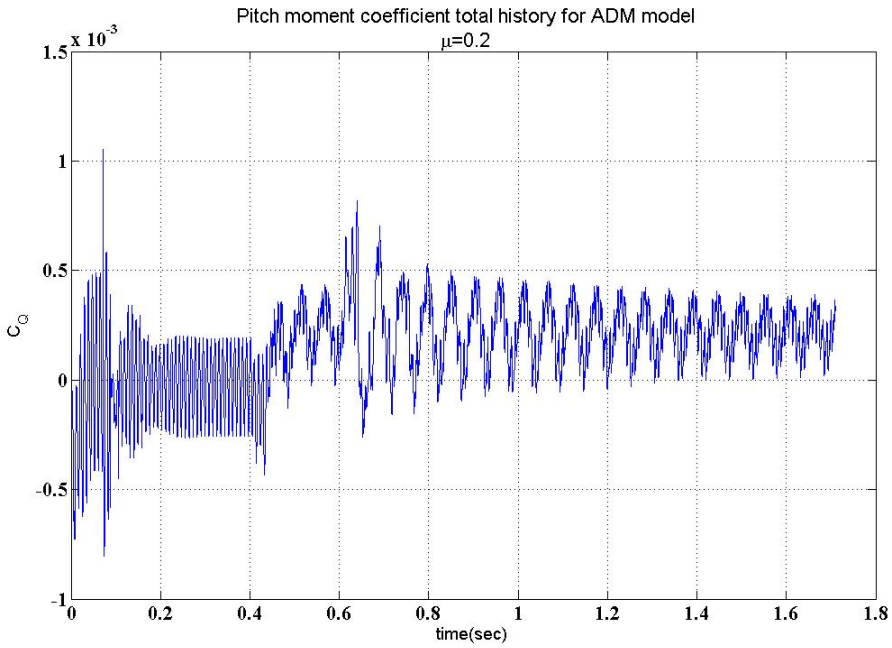

Figure 85: ADM pitch moment coefficient history for $\mu = 0.2$.

along with the rank number. However this increases the size of the transition matrix which will lead to the increase of the numerical noise content in the stability analysis solution.

In next section, the stability analysis is applied to UH-60A fully articulated rotor using high fidelity DYMORE/OVERFLOW tight coupling simulation, and the rotor computed stability characteristics for the relevant modes are compared to those computed by Bauchau et al. [10] using DYMORE alone code.

5.5 Stability Analysis of the UH-60A Case 8534 using CFD/CSD Tight Coupling

The UH-60A model has been chosen as the demonstration case for fully articulated rotor model. For the high speed 8534 case, the flight conditions are $\mu = 0.368$, $C_T/\sigma = 0.084$, $M_\infty = 0.236$, $M_t = 0.642$, $\alpha_s = -7.31^o$, and an altitude of 3273 ft. The target loads trim values used are $16,602$ lb thrust, 6042 lb.ft rolling moment, and -4169 lb.ft for the pitching moment.

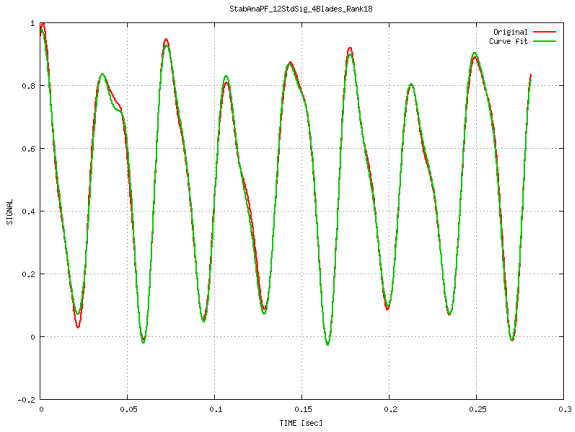

(a) Signal reconstruction blade 1 tip displacement flap motion $\mu = 0.2$.

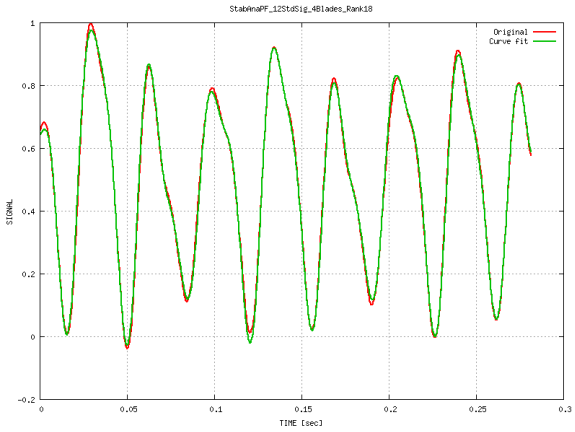

(b) Signal reconstruction blade 2 tip displacement flap motion $\mu = 0.2$.

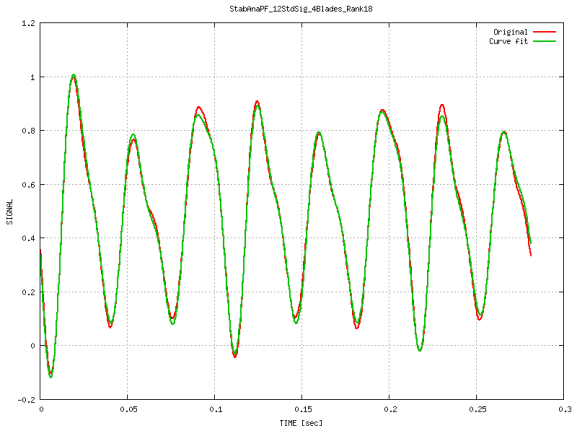

(c) Signal reconstruction blade 3 tip displacement flap motion $\mu = 0.2$.

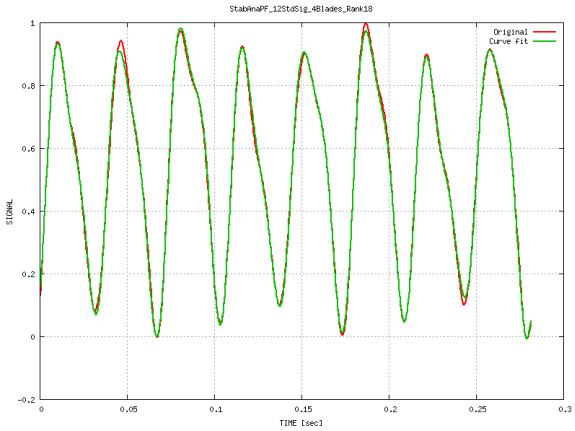

(d) Signal reconstruction blade 4 tip displacement flap motion $\mu = 0.2$.

Figure 86: Blades tip flap displacement signal reconstruction for $\mu = 0.2$.

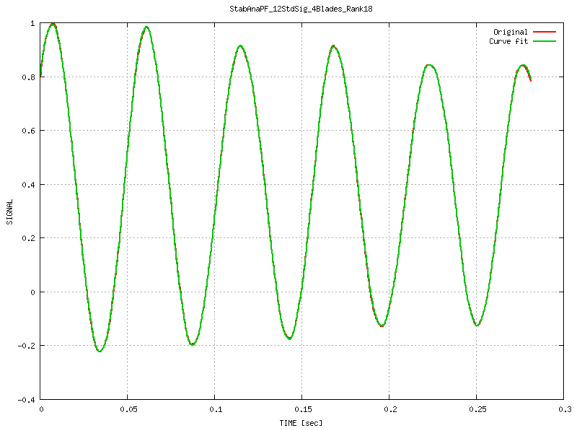

(a) Signal reconstruction blade 1 tip displacement lead-lag motion $\mu = 0.2$.

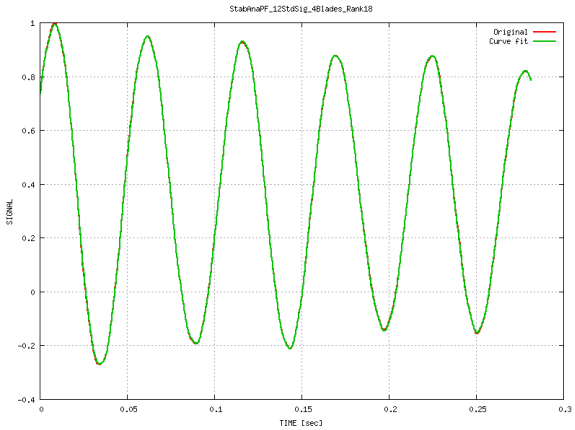

(b) Signal reconstruction blade 2 tip displacement lead-lag motion $\mu = 0.2$.

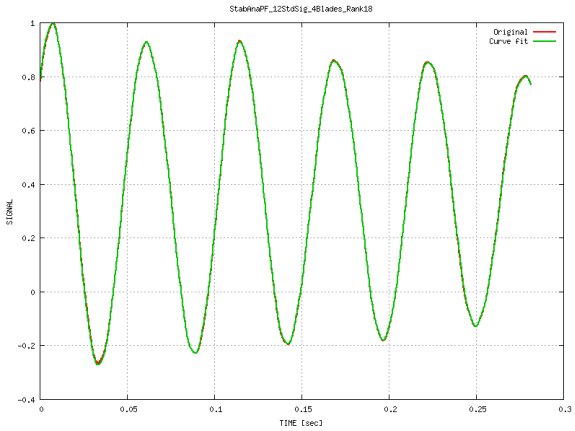

(c) Signal reconstruction blade 3 tip displacement lead-lag motion $\mu = 0.2$.

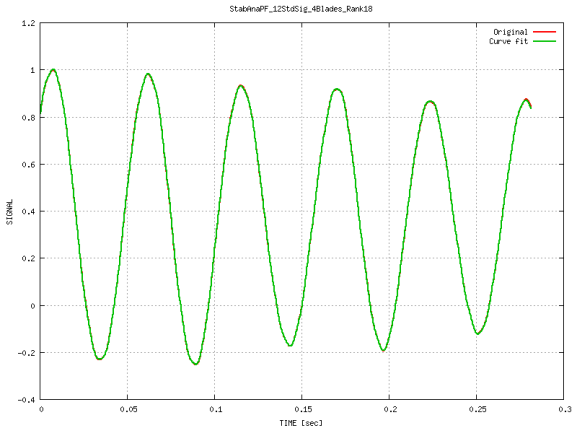

(d) Signal reconstruction blade 4 tip displacement lead-lag motion $\mu = 0.2$.

Figure 87: Blades tip lead-lag displacement signal reconstruction for $\mu = 0.2$.

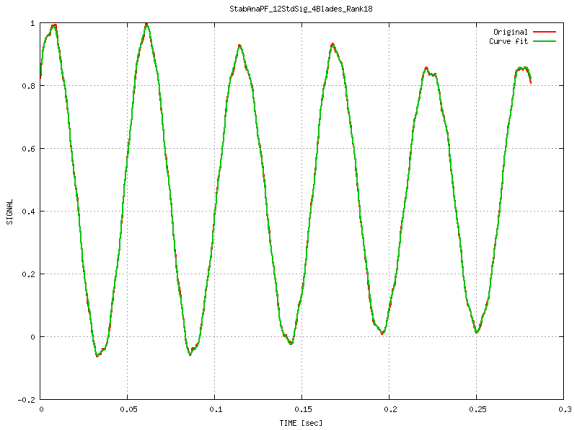

(a) Signal reconstruction blade 1 tip displacement lead-lag rotation $\mu = 0.2$.

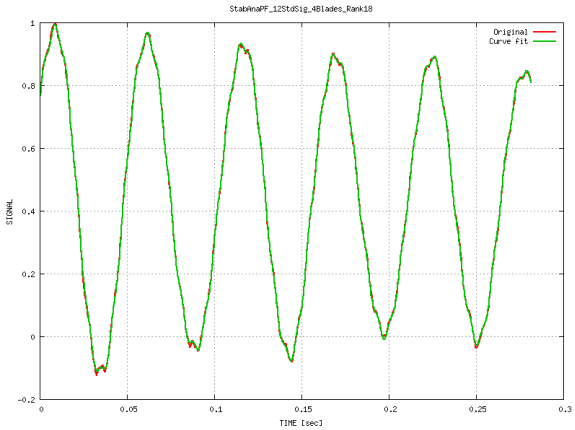

(b) Signal reconstruction blade 2 tip displacement lead-lag rotation $\mu = 0.2$.

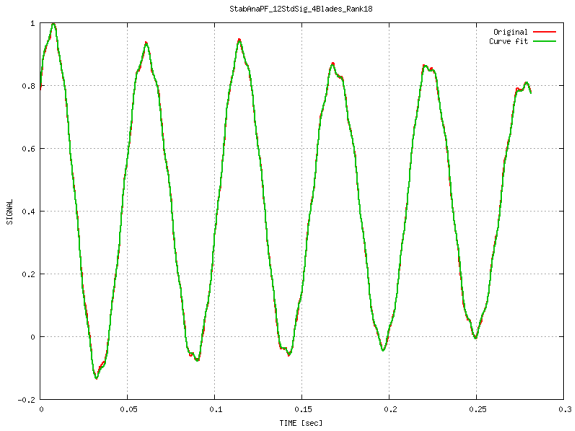

(c) Signal reconstruction blade 3 tip displacement lead-lag rotation $\mu = 0.2$.

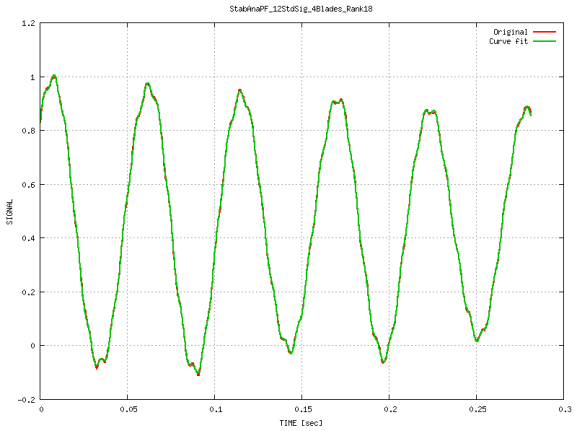

(d) Signal reconstruction blade 4 tip displacement lead-lag rotation $\mu = 0.2$.

Figure 88: Blades tip lead-lag rotation signal reconstruction for $\mu = 0.2$.

First, the loose coupling strategy with the delta-airloads approach was used to obtain a converged, periodic solution for the UH-60A case 8534 flight conditions. Next, using this solution as an initial condition, the tight coupling procedure was applied to predict the aeroelastic response of the system. A perturbation was applied to the system, which consisted of three time-dependent concentrated loads applied at the blade's three-quarter span ($75\%R$) location: a load applied upward in the direction perpendicular to the rotor plane, a load acting in the plane of the rotor directed towards the trailing edge, and a torque. These three loads were applied as over time as linearly increasing to the maximum and then decreasing to zero. This loading created triangular pulses with maximum amplitudes of 500 lb, 100 lb, and $2,200$ lb.ft, respectively in the normal, in-plane and torsional directions. For each case the triangular pulse lasted for 0.1 revolution.

The applied perturbation changed the blade aeroelastic response causing modification in the airloads. After the end of the perturbation, the released rotor continued to respond to the perturbation and the subsequent aeroelastic effects. Four signals were identified for the stability analysis procedure: the flap and lag displacements, the lag rotation angle at the blade three-quarter span location, and the root flap angle. All four signals were sampled at 180 or 290 points per revolution.

Finally, both PFA and Prony stability analysis methods [7] were applied to the resulting CFD/CSD response. Very similar results were obtained from both approaches. A window starting 0.01 seconds after the end of the perturbation and lasting for 3.5 revolutions was investigated. Table 22 lists the damping ratios for the 1^{st} lead-lag, 1^{st} flap, 2^{nd} flap, and 1^{st} torsion modes. Five different approaches (table 21) were applied to evaluate the system modal parameters. The first two approaches use the PFA with rank numbers of 32 and 16, and sampling rates of 180 and 290 points per revolution, respectively. The last three approaches use Prony's method with rank numbers of 32, 16 and 18, and sampling rates of 180, 180 and 290 points per revolution, respectively.

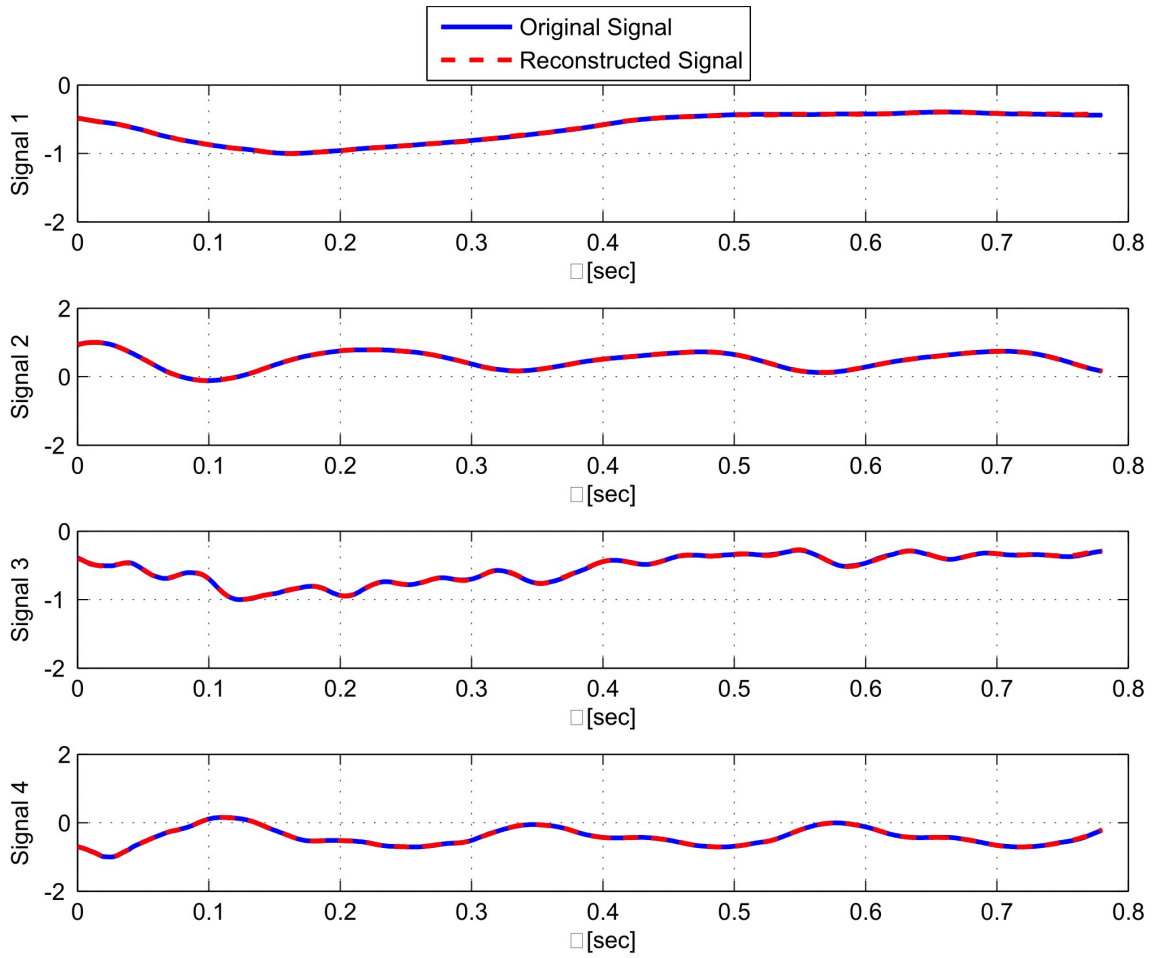

Figure 89: Comparison of the original and reconstructed signals for the four signal locations.

The various signals were reconstructed based on the identified modal parameters to ensure the validity of the prediction. Figure 89 illustrates the original and reconstructed signals for the four signals selected for the analysis. The excellent correlations observed between the original and the reconstructed signals indicates the accuracy of the stability analysis results. Predicted frequencies are shown in Figure 90, and as expected they are in good agreement with the frequencies predicted with lower-order aerodynamic models [9].

Figure 91 shows the corresponding damping ratios. Table 22 lists the damping ratios for the five approaches. Predictions are consistent for the four rotor modes. As expected, the first flap mode is well damped in contrast with the second flap and

Table 21: Characteristics of the stability approaches.

Notation	Algorithm	Rank number	Sampling rate [/rev]
PF	Floquet	32	180
PF6	Floquet	16	290
PR	Prony	32	180
PR2	Prony	16	180
PR5	Prony	18	290

torsion modes which are very lightly damped. Note that the signal length of 3.5 revolutions data used here is not long enough to obtain reliable predictions of these lightly damped modes.

The results presented in figure 91 show that the identified damping of the first lag mode is very high, about 35%. These results are unexpected since the first lag mode of the UH-60A rotorcraft is known to be very lightly damped. Upon investigation, it was first observed that CFD analysis predicted a doubling of the overall lift over the perturbation time period compared to a 40% increase for lower-fidelity aerodynamics. The elastic deflection from that loading indicated a significant, but physically feasible, response in the blade attitude as shown in figure 92. The UH-60A case selected for demonstration, case 8534, is a high-speed flight case and the tip may enter the transonic regime. Increases in twist angle will cause the blade outer span to enter further into the transonic regime, giving rise to shocks which can dramatically influence the lead-lag damping. The Mach contours on the upper surface of the rotor at the 90° azimuth for the advancing side of the rotor in figure 93 clearly illustrate this aerodynamic phenomenon. The perturbation immerses the rotor outer span in a higher transonic flow compared to the pre-perturbed state, and this state remains for a significant portion of the window used for the stability analysis. The result of the transonic flow comes via the presence of stronger shocks, which dramatically increase the drag. Thus, the damping in the lead-lag mode is disproportionately high

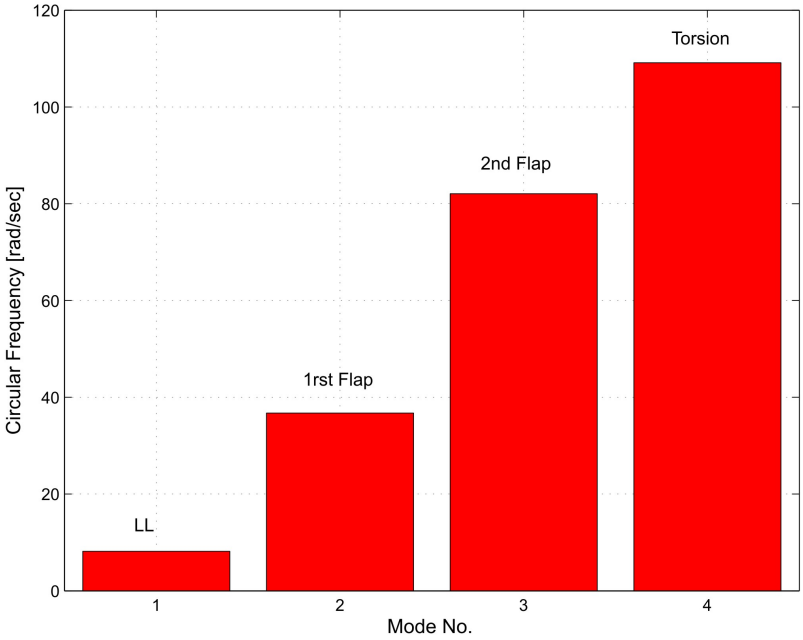

Figure 90: Predicted frequencies for the four rotor modes.

compared to the damping encountered during most of the level flight regime.

Table 22: Damping ratios for the four rotor modes.

Case	Lead-lag	1st Flap	2nd Flap	Torsion
PF	-31.85	-21.24	0.13	-0.66
PF6	-47.11	-30.84	-0.87	-0.25
PR	-31.85	-21.24	0.13	-0.66
PR2	-48.37	-30.90	-0.86	-0.254
PR5	-32.44	-17.49	-0.23	-0.39

5.5.1 Conclusions

A number of observations can be made based on the results presented here:

- The predicted frequencies of the rotor modes correlate well with the known rotor frequencies of the UH-60A.
- Signal reconstruction indicates that the PFA reliably extracts the modal parameters from the computed signals.

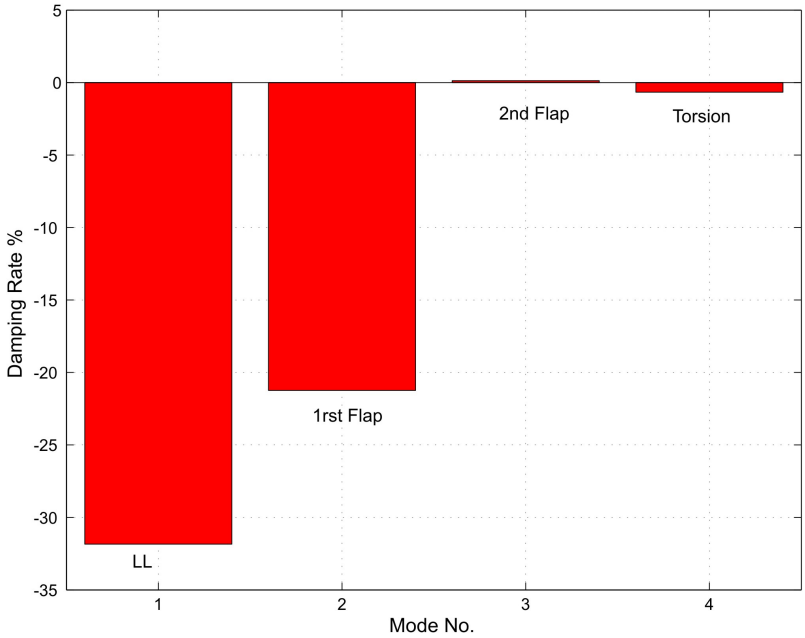

Figure 91: Predicted damping ratios for the four rotor modes.

- Using as few as 3.5 revolutions after the system is perturbed yields good predictions of the rotor frequencies, but it is not long enough to reliably predict the damping characteristics of the lightly damped modes.

- The number of CFD/CSD revolutions to determine the stability characteristics after releasing the perturbation appears to be dependent on the magnitude of the perturbation.

- A large perturbation in high speed forward flight may generate large damping ratios in lead-lag due to the presence of strong shocks.

- It is not a trivial task to identify the different modes frequencies and damping from one stability analysis run, as the results of the stability analysis are contaminated with noise, specially with the increasing of the perturbation and the rank number, and it depend on the windows size too.

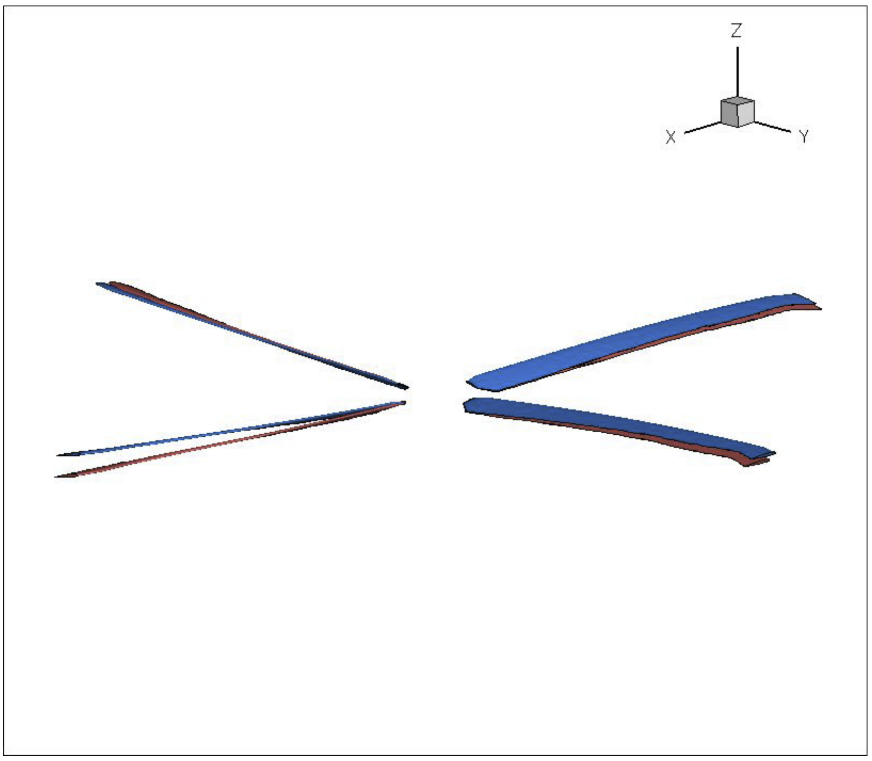

Figure 92: Blade response at the maximum perturbation location.

5.6 Stability Analysis of the UH-60A Case 8534 using DYMORE alone with and without the Hydraulic damper

To identify the suspected source of the computed lead-lag damping, stability analysis (described previously in section 5.5) is carried using DYMORE stand alone solver to simulate the UH-60A forward flight case 8534 without the use of the lead-lag hydraulic damper in the modeling of the UH-60A deck. The model was simulated for a periodic steady solution then perturbation loads were applied exactly like the one applied in the CFD/CSD run mentioned previously. This perturbation consisted of three time-dependent concentrated loads applied at the blade's three-quarter span ($75\%R$) location: a load applied upward in the direction perpendicular to the rotor plane, a load acting in the plane of the rotor directed towards the trailing edge, and a torque. These three loads were applied as over time, as linearly increasing to the maximum and then decreasing to zero. This loading created triangular pulses with

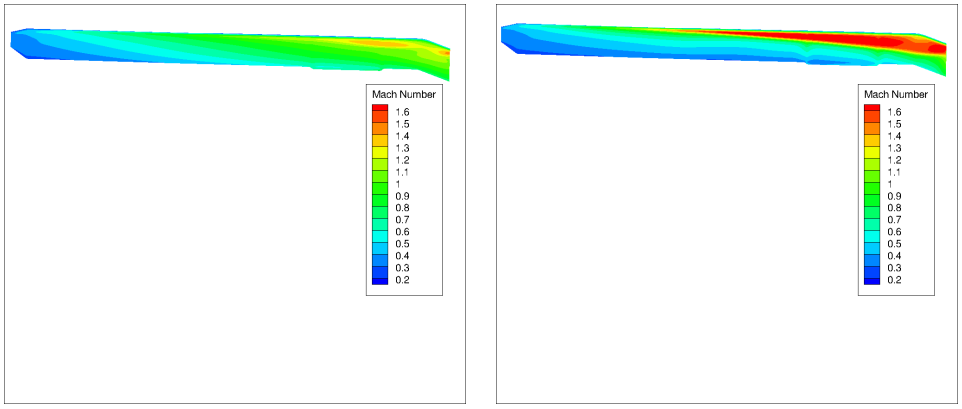

(a) Prior to perturbation.

(b) During perturbation.

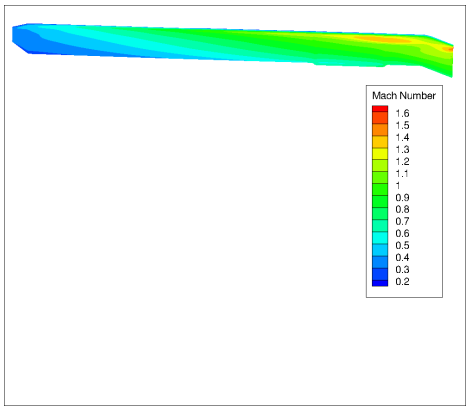

(c) Three revolutions after perturbation.

Figure 93: UH-60A CFD mesh used to demonstrate the CFD/CSD based stability analysis.

maximum amplitudes of 500 lb, 100 lb, and $2,200$ lb.ft respectively in the normal, in-plane and torsional directions. For each case, the triangular pulse lasted for 0.1 revolution.

Next, signals were considered starting 0.01 seconds after the end of the perturbation and lasting for 26 revolutions. Moving window analysis was applied with each window width of 3.9 revolutions. PFA with rank number of 24 and sampling rate of 20 points per revolution was applied to the signals. Results are compared in figure 94, using both the Coleman transform and the standard signals, for both the UH-60A run with and without the hydraulic lead-lag damper, which shows that there is a lot of scatter in the data with the damper because the signal dies out very quickly, and hence, it is difficult to accurately measure frequencies. The damping ratio changed dramatically from around -50% with the hydraulic damper, to around -9% without it, which means that the very high computed damping ratio for the lead-lag mode is mainly the damping of the hydraulic damper and not aerodynamic or structural damping. Thus the hydraulic lead-lag damper is the main source of the lag mode high damping ratio computed by the stability analysis.

This same test could be performed using CFD/CSD tight coupling simulation of the UH-60A without including the lead-lag hydraulic damper in the structural model, to compare the results to those of section 5.5. This comparison will help identifying the real source of the computed lead-lag damping ratio, and determine if its main cause might be the hydraulic lead-lag damper.

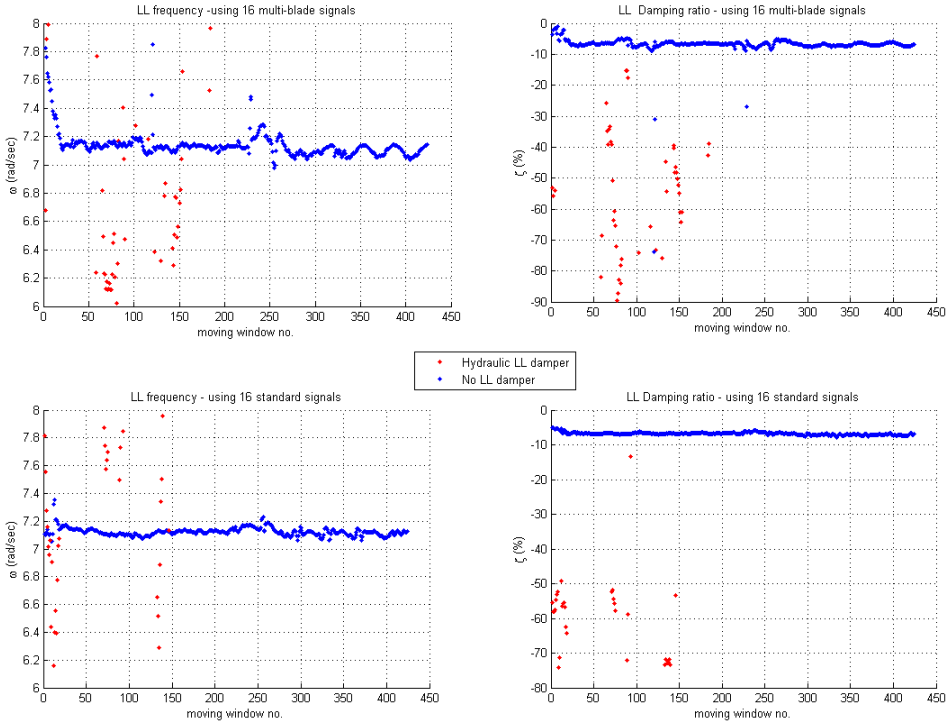

Figure 94: Comparing UH-60A case 8534 stability analysis results with and without the hydraulic LL damper.

Chapter VI

CONCLUSIONS

- Leishman-Beddoes unsteady aerodynamics model including its semi-empirical dynamic stall model and ONERA EDLIN dynamic stall model were evaluated to determine their ability to improve finite-state-based dynamic stall predictions within a computational structural dynamics method. The advanced Leishman-Beddoes semi-empirical dynamic stall model did not improve the blade airload predictions with an increase of the number of the wake inflow modes. The three-dimensional finite-state generalized dynamic wake theory was also found to be unstable as the number of inflow modes increased.

- The performance of the quasi-steady trimmer was evaluated by trimming a fully articulated rotor using a comprehensive structural dynamics solver. As expected, the lift converged fast to its target value, whereas the pitch and roll moments were much slower to converge.

- Kinematic and load interfaces were added to a comprehensive structural dynamics code (DYMORE) to enable its coupling (tight or loose coupling) with any external computational fluid dynamics code. The coupling is performed by automated data exchange through memory allocation of the interchanged data, alleviating the need for flags files or I/O formatted data files. The upgrades and modifications in both the computational structural dynamics code and the computational fluid dynamics code were tested in loose coupling runs for a rotor in two forward flights cases. Tight coupling run was successfully performed. The results proved the ability of the implemented interfaces to exchange the data and to translate these data correctly in respect to the right frames, directions,

blades, and dimensions.

- Using the kinematic and load interfaces implemented in the structural and fluid dynamics solvers, along with the quasi-steady trimmer and ordinary kriging meta-model, a fully articulated rotor model was successfully trimmed in forward flight under tight coupling simulation. The kriging meta-model was trained using 9 sample points obtained using the two solvers loose coupling simulations. This kriging meta-model was used to predict control settings corresponding to the target loads. The predicted control settings were used as the initial control settings for loose coupling run. Loose coupling simulation was trimmed more efficiently and it has been found to save typically $1-3$ coupling iterations compared to simulations that apply controls computed by the standard trim process. This meta-model was also used to compute the Jacobian matrix required for the trimming of the model under tight coupling, hence replacing the lengthy and expensive system identification technique in providing a reliable Jacobian matrix. The kriging meta-model accuracy was shown to depend on the number of sample data points and their locations, as expected.

- The Partial Floquet stability analysis along with the moving window analysis and Coleman post-processing were applied to compute the modal parameters of a hingeless rotor at different advance ratios. The stability analysis was performed on the simulation of a computational structural dynamics and computational fluid dynamics method tight coupling simulations. Obtained stability analysis modal parameters were compared to the available experimental data. The stability analysis was also performed to a fully articulated rotor in forward flight using the structural and the fluid computational solvers tight coupling simulation. Signal reconstruction was used to assess the accuracy of the computed modal parameters.

- For the hingeless rotor, performing stability analysis over several windows of the transient response at its different phases showed that the lag mode damping exponent was function of the moving window starting point which mostly is due to the existence of system nonlinearity.

- For the fully articulated rotor, it was found that the predicted frequencies correlate well with the known rotor frequencies. Using as few as 3.5 revolutions after the system is perturbed yields good predictions of the rotor frequencies, but it was not long enough to reliably predict the damping characteristics of the lightly damped modes.

- The sufficient number of tight coupling revolutions of the numerical structural dynamics method and the numerical fluid dynamics method was found to depend on the magnitude of the perturbation. A large perturbation in high speed forward flight may generate large damping ratios especially in lightly damped lead-lag mode due to the presence of strong shocks.

- It is not a trivial task to identify a rotor modal parameters from one stability analysis run, as the results of the stability analysis are contaminated with noise, specially with the increasing of the perturbation and the rank number, and it depend on the length of the transient response too.

Chapter VII

RECOMMENDATIONS FOR FUTURE WORK

Based on the computational studies and the conclusions drawn from them, the following recommendations are made for future research:

1. Enhance the implementation of the Leishman-Beddoes semi-empirical dynamic stall model in DYMORE to enable the user to specify the semi-empirical model parameters at all the airstations as function of the Mach number and the airfoil shape. The semi-empirical model parameters can be computed from the available static and dynamic wind tunnel experimental data.

2. Test the application of the quasi-steady trimmer along with the kriging meta-model for the simulation of rotor in maneuvering flight conditions.

3. Using the CFD/CSD tight coupling simulation to perform stability analysis for the UH-60A in forward flight without using the hydraulic lead-lag damper in the model, to identify the source of the computed lead lag mode damping (aerodynamics, structural or just from the lead-lag damper).

4. Qualitative study of the effect of the moving window length on the stability analysis results.

5. For the ordinary kriging application, study of the sequential sampling technique by directing the new sample points to regions characterized by larger errors to select the training data points locations, and to decide the minimum number of data points to efficiently train the kriging meta-model.

REFERENCES

[1] Abras, J., Lynch, C. E., and Smith, M., "Rotorcraft Methodology For Unstructured CFD-CSD Coupling," *Journal of the American Helicopter Society*, to appear, 2012.

[2] Abras, J. and Smith, M. J., "Rotorcraft Simulations Using Unstructured CFD-CSD Coupling," in *Proceedings of the AHS Specialists Meeting*, (San Francisco, CA), January 2008.

[3] Anon., "RCAS Theory Manual, Version 2.0," Technical Report USAAMCOM/AFDD TR 02-A-005, U.S. Army Aviation and Missile Command, Moffett Field, California, June 2003.

[4] Bauchau, O. and Bottasso, C., "Unsteady Rotorcraft Trim," in *ASME International Design Engineering Technical Conferences*, (Las Vegas, Nevada), September 2007.

[5] Bauchau, O., Bottasso, C., and Nikishkov, Y., "Modeling Rotorcraft Dynamics with Finite Element Multibody Procedures," *Mathematical and Computer Modeling*, vol. 33, no. 10-11, pp. 1113–1137, 2001.

[6] Bauchau, O. and Smith, M., "Innovative Strategies for Rotary-Wing Coupled Aeroelastic Simulations," Tech. Rep. Interim Progress Report, NRA Grants NNX07AP43A, NASA, June 2008.

[7] Bauchau, O. and Wang, J., "Stability Analysis of Complex Multibody Systems," *Journal of Computational and Nonlinear Dynamics*, vol. 1, no. 1, pp. 71–80, 2006.

[8] Bauchau, O. and Wang, J., "Stability Evaluation and System Identification of Flexible Multibody Systems," *Multibody System Dynamics*, vol. 18, no. 1, pp. 95–106, 2007.

[9] Bauchau, O. and Wang, J., "Efficient and Robust Approaches to The Stability Analysis of Large Multibody Systems," *Computational and Nonlinear Dynamics*, vol. 3, no. 1, pp. 1–12, 2008.

[10] Bauchau, O. and Wang, J., "Efficient and Robust Approaches for Rotorcraft Stability Analysis," *Journal of the American Helicopter Society*, vol. 55, no. 3, pp. 032006 1–9, 2010.

[11] Beddoes, T., "Practical Computation of Unsteady Lift," *Vertica*, vol. 8, no. 1, pp. 55–71, 1984.

[12] Bhagwat, M. J., Ormiston, R. A., Saberi, H. A., and Hong, X., "Application of CFD/CSD Coupling for Analysis of Rotorcraft Airloads and Blade Loads in Maneuvering Flight," *Proceedings of the American Helicopter Society 63rd Annual National Forum*, 2007.

[13] Bisplinghoff, R., Ashley, H., and Halfman, R., *Aeroelasticity*. Reading, Massachusetts: Addison-Wesley Publishing Company, second ed., 1955.

[14] Bousman, W., "Airfoil Dynamic Stall and Rotorcraft Maneuverability," in *NASA/TM-2000-209601, AFDD/TR-00-A-008*, (Ames Research Center, Moffett Field, California), July 2000.

[15] Bousman, W. and Maier, T., "An Investigation of Helicopter Rotor Blade Flap Vibratory Loads," in *American Helicopter Society* 48^{th} *Annual Forum Proceedings*, (Washington, D.C.), pp. 977–999, June 3-5 1992.

[16] Bousman, W. and Winkler, D., "Application of the Moving-Block Analysis," in *Proceedings of the 22th Structures, Structural Dynamics, and Materials Conference, Dallas, TX, April 17-20*, 1981.

[17] Buning, P., Gomez, R., and Scallion, W., "CFD Approaches for Simulation of Wing-Body Stage Separation," in *22nd Applied Aerodynamics Conference and Exhibit*, (Providence, Rhode Island), August 2004.

[18] Chan, W., Meakin, R., and Potsdam, M., "CHSSI Software for Geometrically Complex Unsteady Aerodynamic Applications," in *AIAA 39th Aerospace Sciences Meeting and Exhibit, AIAA Paper 2001-0593*, (Reno, NV), January 2001.

[19] Clark, B., "Modeling Dynamic Stall Of Sc-1095 Airfoil At High Mach Numbers," Master's thesis, Georgia Institute of Technology, 2010.

[20] Coleman, R., "Theory of Self-Excited Mechanical Oscillations of Hinged Rotor Blades," Tech. Rep. WR-L-308, NACA Report, Langley Research Center, 1943.

[21] Coleman, R. and Feingold, A., "Theory of Self-Excited Mechanical Oscillations of Helicopter Rotors with Hinged Blades," Tech. Rep. 1351, NACA Report, 1956.

[22] Cressie, N., *Statistics for Spatial Data.* New York: John Wiley & Sons, 1993.

[23] Currin, C., Mitchell, T., Morris, M., and Ylvisaker, D., "Modeling and Solution Methods for Efficient Real-Time Simulation of Multibody Dynamics," *Multibody System Dynamics*, vol. 1, no. 3, pp. 259–280, 1997.

[24] Daberkow, D., *A Formulation Of Metamodel Implementation Processes For Complex Systems Design*. PhD thesis, Georgia Institute of Technology, Atlanta, GA, 2002.

[25] Daberkow, D. and Mavris, D., "An Investigation of Metamodeling Techniques for Complex Systems Design," in *9th AIAA/ISSMO Symposium on Multidisciplinary Analysis and Optimization, AIAA Paper 2002-5457*, (Atlanta, GA), 4-6 September 2002.

[26] Datta, A. and Chopra, I., "Prediction of UH-60A dynamic stall loads in high altitude level flight using CFD/CSD coupling," in *American Helicopter Society 61st Annual Forum*, (Grapevine, Texas), June 1-3 2005.

[27] Davis, S. and Malcolm, G., "Experimental Unsteady Aerodynamics of Conventional and Supercritical Airfoils," Tech. Rep. TM 81221, NASA, 1980.

[28] Duque, E., Sankar, L., Menon, S., Ruffin, S., Smith, M., Ahuja, A., Brentner, K. S., Long, L. N., Morris, P. J., and Gandhi, F., "Revolutionary Physics-Based Design Tools for Quiet Helicopters," *44th AIAA Aerospace Sciences Meeting and Exhibit, AIAA Paper 2006-1068*, January 9-12, 2006.

[29] Floquet, G., "Sur Les Équations Différentielles Linéaires à Coefficients Périodiques," *Annales scientifiques de l'École Normale Supérieure*, vol. 12, pp. 47–88, 1883.

[30] Friedmann, P., "Numerical Methods for Determining the Stability and Response of Periodic Systems with Applications to Helicopter Rotor Dynamics and Aeroelasticity," *Computers and Mathematics with Applications*, vol. 12A, pp. 131–148, 1986.

[31] Gaonkar, G. and Peters, D., "Review of Floquet Theory in Stability and Response Analysis of Dynamic Systems with Periodic Coefficients," in *R.L. Bisplinghoff Memorial Symposium Volume on Recent Trends in Aeroelasticity, Structures and Structural Dynamics*, pp. 101–119, Gainesville: University Press of Florida, Feb 6-7 1986.

[32] Giunta, A., *Aircraft Multidisciplinary Design Optimization Using Design of Experiments Theory and Response Surface Modeling.* PhD thesis, Department of Aerospace and Ocean Engineering, Virginia Polytechnic and State University, Blacksburg, VA, 1997.

[33] Golub, G. and van Loan, C., *Matrix Computations.* Baltimore: The Johns Hopkins University Press, second ed., 1989.

[34] Hammond, C. and Doggett, R.V., J., "Determination of Subcritical Damping by Moving-Block/Randomdec Applications," in *NASA Symposium on Flutter Testing Techniques, NASA SP-415*, pp. 59–76, 1975.

[35] Harris, F., Tarzanin, F., and Fisher, R., "Rotor High Speed Performance, Theory vs. Test," *Journal of the American Helicopter Society*, vol. 15, no. 3, pp. 35–44, 1970.

[36] Hübner, B., Walhorn, E., and Dinkler, D., "A Monolithic Approach to FluidStructure Interaction Using SpaceTime Finite Elements," *Computer Methods in Applied Mechanics and Engineering*, vol. 193, no. 23-26, pp. 2087–2104, 2004.

[37] Jespersen, D., Pulliam, T., and Buning, P., "Recent Enhancements to OVERFLOW," in *35th Aerospace Sciences Meeting and Exhibit*, (Reno, NV), Jan. 6-9 1997.

[38] Jin, R., Chen, W., and Simpson, T., "Comparitive Studies of Metamodeling Techniques under Multiple Modeling Criteria," *Structural and Multidisciplinary Optimization*, vol. 23, no. 1, pp. 1–13, 2000.

[39] Johnson, W., "Rotorcraft Aerodynamics Models for a Comprehensive Analysis," tech. rep., Johnson Aeronautics.

[40] Johnson, W., "The response and Airloading of Helicopter Rotor Blades Due to Dynamic Stall," Tech. Rep. ASRL TR 130-1, Massachusetts Institute of Technology, 1970.

[41] Johnson, W., *CAMRAD/JA; A Comprehensive Analytical Model of Rotorcraft Aerodynamics and Dynamics; Volume I, Theory Manual*. Johnson Aeronautics, Palo, Alto, California, 1988.

[42] Johnson, W., "CAMRAD II Components Theory, Volume II," Technical Report Release 3.2, Johnson Aeronautics, Palo Alto, California, June 1999.

[43] Jones, D., Schonlau, M., and Welch, W., "Efficient Global Optimization of Expensive Black-Box Functions," *Journal of Global Optimization*, vol. 13, no. 4, pp. 455–492, 1998.

[44] Kleijnen, J. P., "Kriging Metamodeling in Simulation: A Review," *Europian Journal of Operational Research*, vol. 192, no. 3, pp. 707–716, 2009.

[45] Kufeld, R., Balough, D., Cross, J., Studebaker, K., Jennison, C., and Bousman, W., "Flight Testing of the UH-60A Aircraft," in *American Helicopter Society 50th Annual Forum Proceedings*, (Alexandria, VA), May 11-13 1994.

[46] Lawrence, R. and Bernard, G., *Theory and Application of Digital Signal Processing*. New Jersey: Prentice-Hall, Inc., 1975.

[47] Leishman, J., "Indicial Lift Approximations for Two-Dimensional Subsonic Flow as Obtained from Oscillatory Measurements," *Journal of Aircraft*, vol. 30, no. 3, pp. 340–351, 1993.

[48] Leishman, J., *Principles of Helicopter Aerodynamics*. Cambridge: Cambridge University Press, second ed., 2006.

[49] Leishman, J. and Beddoes, T., "A Generalized Model for Airfoil Unsteady Behavior and Dynamic Stall using the Indicial Method," in *American Helicopter Society* 42^{nd} *Annual Forum Proceedings*, (Washington, DC), June 2–5 1986.

[50] Leishman, J. and Beddoes, T., "A Semi-Empirical Model for Dynamic Stall," *Journal of the American Helicopter Society*, vol. 34, no. 3, pp. 3–17, 1989.

[51] Leishman, J. and Crouse, G., "State-Space Model for Unsteady Airfoil Behavior and Dynamic Stall," in *Proceedings of the 30th AIAA/ASME/ASCE/AHS/ASC Structures, Structural Dynamics and Materials Conference, Mobile, Alabama, April 3-5, 1989*, pp. 1319–1330, 1989.

[52] Leishman, J. and Nguyen, K., "State-Space Representation of Unsteady Airfoil Behavior," *AIAA Journal*, vol. 28, no. 5, doi:10.2514/3.25127, pp. 836–844, 1990.

[53] Liu, H., *Interfacing Comprehensive Rotorcraft Analysis With Advanced Aeromechanics And Vortex Wake Models*. PhD thesis, Georgia Institute of Technology, Atlanta, GA, 2008.

[54] Lomax, H., Heaslet, M., Fuller, F., and Sludder, L., "Two and Three Dimentional Unsteady Lift Problems in High Speed Flight," in *NACA report 1077*, 1952.

[55] Lyapunov, A., *The General Problem of Stability of Motion*. London: Taylor & Francis, 1992.

[56] Lynch, C. E. and Smith, M. J., "Extension and Exploration of a Hybrid Turbulence Model on Unstructured Grids," *AIAA*, vol. 49, no. 11, doi:10.2514/1.56296, pp. 2585–2591, 2011.

[57] Lynch, C. E., *Advanced CFD Methods For Wind Turbine Analysis*. PhD thesis, Georgia Institute of Technology, Atlanta, GA, 2011.

[58] Mardia, K. V. and Watkins, A. J., "On Multimodality of the Likelihood in the Spatial Linear Model," *Biometrika*, vol. 76, no. 2, pp. 289–295, 1989.

[59] Martin, J. and Simpson, T., "A Study of The Use of Kriging Models to Approximate Deterministic Computer Models," in *Proceedings of DETC'03 ASME 2003 Design Engineering Technical Conferences and Computers and Information in Engineering Conference, Chicago, Illinois*, September 2–6 2003.

[60] McAlister, K. W., Lambert, O., and Petot, D., "Application of the ONERA Model of Dynamic Stall," *NASA Technical Paper*, vol. 2399, 1984.

[61] Menter, F., "Two-Equation Eddy-Viscosity Turbulence Models for Engineering Applications," *AIAA*, vol. 32, no. 8, doi: 10.2514/3.12149, pp. 1598–1605, 1994.

[62] Nixon, J., *A Systematic Process for Adaptive Concept Exploration*. PhD thesis, Georgia Institute of Technology, 2006.

[63] Nygaard, T. A., Saberi, H. A., Ormiston, R. A., Strawn, R. C., and Potsdam, M., "CFD and CSD Coupling Algorithms and Fluid Structure Interface for Rotorcraft Aeromechanics in Steady and Transient Flight Conditions," in *American Helicopter Society 62nd Annual Forum Proceedings*, (Phoenix, AZ), May 9-11 2006.

[64] Peters, D. and Barwey, D., "A General Theory of Rotorcraft Trim," *Mathematical Problems in Engineering*, vol. 2, no. 1, pp. 1–34, 1996.

[65] Peters, D., Barwey, D., and Su, A., "An Integrated Airloads-Inflow Model for Use in Rotor Aeroelasticity and Control Analysis," *Mathematical and Computer Modeling*, vol. 19, no. 3-4, pp. 109–123, 1994.

[66] Peters, D., Chouchane, M., and Fulton, M., "Helicopter Trim with Flap-Lag-Torsion and Stall by an Optimized Controller," *Journal of Guidance, Control and Dynamics*, vol. 13, no. 5, pp. 824–834, 1990.

[67] Peters, D. and He, C., "Finite State Induced Flow Models. Part II: Three-dimensional Rotor Disk," *Journal of Aircraft*, vol. 32, no. 2, pp. 323–333, 1995.

[68] Peters, D., Karunamoorthy, S., and Cao, W., "Finite State Induced Flow Models. Part I: Two-dimensional Thin Airfoil," *Journal of Aircraft*, vol. 32, no. 2, pp. 313–322, 1995.

[69] Petot, D., "Differential Equation Modeling of Dynamic Stall," *La Recherche Aérospatiale*, vol. 5, no. 1989-5, pp. 60–72, 1989.

[70] Phanse, S., Sankar, L., and Bauchau, O., "An Efficient Tightly Coupled Fluid-Solid Interaction for Modeling Rotors in Forward Flight," in *The 2nd International Basic Research Conference on Rotorcraft Technology*, (Nanjing, China), November 7–9 2005.

[71] Potsdam, M., Fulton, M. V., Yeo, H., Ormiston, R., and Sim, B., "Advancing State-of-the-Art Unsteady, Multidisciplinary Rotorcraft Simulations," in *High Performance Computing Modernization Program Users Group Conference (HPCMP-UGC), 2010 DoD*, (Schaumburg, IL), pp. 115–122, 2010.

[72] Potsdam, M., Yeo, H., and Johnson, W., "Rotor Airloads Prediction Using Loose Aerodynamic/Structural Coupling," in *Proceedings of the American Helicopter Society 60th Annual Forum*, (Baltimore, Maryland), June 7-10 2004.

[73] Potsdam, M., Yeo, H., and Johnson, W., "Rotor airloads prediction using loose aerodynamic/strucutral coupling," in *American Helicopter Society 60th Annual Forum Proceedings*, (Baltimore, MD), June 2004.

[74] Quaranta, G., Mantegazza, P., and Masarati, P., "Assessing the Local Stability of Periodic Motions for Large Multibody Non-Linear Systems Using Proper Orthogonal Decomposition," *Journal of Sound and Vibration*, vol. 271, no. 3-5, pp. 1015–1038, 2004.

[75] Rajmohan, N., Manivannan, V., Sankar, L. N., Costello, M., and Bauchau, O., "Development of a Methodology for Coupling Rotorcraft Aeromechanics and Vehicle Dynamics to Study Helicopters in Maneuvering Flight," in *Proceedings of the American Helicopter Society 65^{t}h Annual Forum*, May 27-29 2009.

[76] Reveles, N., Smith, M., Zaki, A., and Bauchau, O., "A Kriging-Based Trim Algorithm For Rotor Aeroelasticity," in *Proceedings of the* 37th *European Rotorcraft Forum*, (Gallarata, Italy), September 13–15 2011.

[77] Runze, L. and Sudjianto, A., "Analysis of Computer Experiments Using Penalized Likelihood in Gaussian Kriging Models," in *Joint Statistical Meetings in Minneapolis, Minnesota, August 7-11*, 2005.

[78] Sanchez-Rocha, M., *Wall-Models for Large Eddy Simulation Based on a Generic Additive-Filter Formulation*. PhD thesis, Georgia Institute of Technology, Atlanta, GA, 2008.

[79] Sanchez-Rocha, M., Kirtas, M., and Menon, S., "Zonal Hybrid RANS-LES Method for Static and Oscillating Airfoils and Wings," in 44th *AIAA Aerospace Sciences Meeting, AIAA Paper 2006-1256*, (Reno, NV), January 9–12 2006.

[80] Shelton, A. B., Braman, K., Smith, M. J., and Menon, S., "Improved Turbulence Modeling for Rotorcraft," in *Proceedings of the American Helicopter Society 62nd Annual Forum*, (Phoenix, AZ), May 9–11 2006.

[81] Sitaraman, J. and Roget, B., "Prediction of Helicopter Maneuver Loads using a Coupled CFD/CSD Analysis," 26th *International Congress of the Aeronautical Sciences*, September 14-19, 2008.

[82] Skjoldan, P. and Bauchau, O. A., "Determination of Modal Parameters in Complex Nonlinear Systems," *Journal of Computational and Nonlinear Dynamics*, vol. 6, no. 3, 2011.

[83] Stumpf, W., *An Integrated Finite-State Model for Rotor Deformation, Nonlinear Airloads, Inflow and Trim*. PhD thesis, Georgia Institute of Technology, Atlanta, Georgia, 1992.

[84] Stumpf, W. and Peters, D., "An Integrated Finite-State Model for Rotor Deformation, Nonlinear Airloads, Inflow and Trim," *Mathematical and Computer Modeling*, vol. 18, no. 3-4, pp. 115–129, 1993.

[85] Subramanian, S., Gaonkar, G., Nagabhushanam, J., and Nakadi, R., "Parallel Computing Concepts and Methods for Floquet Analysis of Helicopter Trim and Stability," *Journal of the American Helicopter Society*, vol. 41, pp. 370–382, 1996.

[86] Thepvongs, S. and Cook, J. R. and Cesnik, C. E. S. and Smith, M. J., "Computational Aeroelasticity of Rotating Wings with Deformable Airfoils," in *Proceedings of the American Helicopter Society 65th Annual Forum*, (Grapevine, Texas), May 27–29 2009.

[87] Timothy, W. S., John, J. K., Timothy, M. M., and Farrokh, M., "Kriging Models for Global Approximation in Simulation-Based Multidisciplinary Design Optimization," *AIAA*, vol. 39, no. 12, doi: 10.2514/2.1234, pp. 2233–2241, 2001.

[88] Truong, V., "A 2-D Dynamic Stall Model Based on a Hopf Bifurcation," tech. rep., European Rotorcraft Forum, Italy, 1993.

[89] Wang, J., *Efficient And Robust Approaches To The Stability Analysis And Optimal Control Of Large-Scale Multibody Systems*. PhD thesis, Georgia Institute of Technology, 2007.

[90] Warnes, J. and Ripley, B., "Problems with Likelihood Estimation of Covariance Functions of Spatial Gaussian Processes," *Biometrika*, vol. 74, no. 3, pp. 640–642, 1987.

[91] Yeo, H., Potsdam, M., and Ormiston, R., "Application of CFD/CSD to Rotor Aeroelastic Stability in Forward Flight," in *The American Helicopter Society* 66^{th} *Annual Forum*, (Phoenix, AZ), May 11-13 2010.

[92] Zaki, A., Reveles, N., Smith, M., and Bauchau, O., "Using Tightly-Coupled CFD/CSD Simulation for Rotorcraft Stability Analysis," in *The American Helicopter Society* 66^{th} *Annual Forum*, (Phoenix, Arizona), May 11-13 2010.